MODELING THE EVOLUTION OF VEHICLE EXHAUST PLUME NEAR ROAD AND IN LABORATORY DILUTION SYSTEMS USING THE CTAG MODEL

A Dissertation

Presented to the Faculty of the Graduate School

of Cornell University

In Partial Fulfillment of the Requirements for the Degree of

Doctor of Philosophy

by

Yan Wang

January 2013

MODELING THE EVOLUTION OF VEHICLE EXHAUST PLUME NEAR ROAD AND IN LABORATORY DILUTION SYSTEMS USING THE CTAG MODEL

Yan Wang, Ph. D.

Cornell University 2013

There are a growing number of people living or spending substantial time near major roadways, being exposed to elevated traffic-related pollutants. Due to their adverse health effect, it is imperative to reduce the uncertainties in the traffic emission inventory and characterize the spatial and temporal impacts of pollutants on near-road air quality, which is critical to assessing human exposure.

This dissertation presents the development and applications of an environmental turbulent reacting flow model, the Comprehensive Turbulent Aerosol Dynamics and Gas Chemistry (CTAG) model. CTAG is designed to simulate the transport and transformation of multiple air pollutants in various environments. For near-road applications, CTAG couples the major turbulent mixing processes with gas-phase chemistry and aerosol dynamics. CTAG demonstrates that significant improvement in predicting the spatial gradients of pollutants near roadways can be achieved by detailed treatment of turbulence characteristics. It is commonly assumed that the NO_2/NOx ratio by volume for most roadways is 5%. However, this dissertation is the first to show that this assumption may not be suitable for most roadways, especially those with a high fraction of heavy-duty truck traffic. It also illustrates that the dynamics of exhaust plumes are highly sensitive to vehicle-induced turbulence, sulfuric acid induced nucleation, and condensation of organic compounds. It

simulates, for the first time, the multi-scale aerosol dynamics and micro-environmental air quality by introducing a multi-scale structure to generate the processed on-road particle emissions. It implies that roadway and surrounding infrastructure designs can affect near-road air quality. CTAG can be used to improve the regulatory model in assessing the air quality in near-road environments.

The turbulent reacting flows inside the fabricated dilution systems are also investigated since they are essential to most emission testing procedures and share the same mechanisms with the atmospheric dilution. CTAG investigates the effects of the dilution parameters and illustrates that turbulence plays a crucial role in mixing the exhaust with the dilution air, and the strength of nucleation dominates the level of particle emissions. A potential unifying parameter, the dilution rate of exhaust, is found to play an important role in new particle formation. Using the CTAG model, urban planners have the potential to develop strategies to reduce the uncertainties associated with dilution samplings and define a standardized dilution sampling methodology for characterizing emissions from multiple combustion sources.

BIOGRAPHICAL SKETCH

Yan Wang was born in May 1985, in Renqiu, China. He received his Bachelor degree from Zhejiang University in June 2008, with a major in Energy & Environment System Engineering. He then joined Sibley School of Mechanical and Aerospace Engineering of Cornell University in August 2008. Yan Wang married Rachel Zhou in January 2010, who is also pursuing a Ph.D. degree in Cornell University. He has accepted a postdoc position with Professor K. Max Zhang at Cornell University after graduation.

To my wife Rachel

ACKNOWLEDGMENTS

I would like to sincerely thank my Ph.D. advisor, Professor K. Max Zhang, for his patience, outstanding guidance and constant help in my Ph.D. study. I am also grateful to Professor Donald L. Koch and Professor Stephen B. Pope for their suggestions and help to my Ph.D. study and for serving in my special committee.

I appreciate my colleagues for their help in my research. They are the current students and visiting scholars in Energy and Environment Research Laboratory: Mr. Jonathan Steffens, Mr. Zheming Tong, Dr. Changxing Hu from Zhejiang University, Ms. Monica Nguyen and previous members, Dr. Bo Yang from Jin Lin University, Dr. Xing Wang. I want to thank Professor Zellman Warhaft and Professor Ephrahim Garcia for their help in the wind tunnel experiment, Dr. Rajesh Bhaskaran and Mr. Andrey Klochko for their help in the parallel computing and Dr. Haifeng Wang for his help in the CFD simulation. I would also thank the help and collaborative opportunity provided by Professor Elena McDonald-Buller and Professor David Allen in University of Texas at Austin, Professor Eric M. Lipsky in Pennsylvania State University, Professor Allen L. Robinson in Carnegie Mellon University, Dr. Topi Ronkko and Professor Jorma Keskinen in Tampere University of Technology. I also appreciate the help from Dekati Ltd. and Ford Motor Company, especially from Dr. Matti Maricq.

I would like to thank all instructors at Cornell University who taught me courses, especially Professor Michel Louge, with whom I also served as Teaching Assistant, and Professor Oliver Gao, who helped me with the writing of one journal paper.

I would thank my wife, Rachel Zhou, for her love, encouragement and support. Pursuing a Ph.D. degree is never an easy task, which applies both to me and my wife.

But I believe together we can overcome all the difficulties and have a wonderful future.

I would also thank my parents and parents-in-law, even though I know this is far from enough. As an international student, I miss my parents and hometown, especially during the Chinese New Year, however, it is my wife and parents-in-law that give me a sweet home in United States that comforts me. I wish my parents and I can unite soon.

TABLE OF CONTENTS

LIST OF FIGURES

LIST OF TABLES

CHAPTER 1

INTRODUCTION

It is estimated that over 35 million people live near roadways in the United States, being exposed to the traffic-related pollutants, e.g., ultrafine particles (UFPs), CO and NOx (HEI, 2010; Wang, 2011). Health studies show elevated risk for development of asthma and reduced lung function in children who live near major highways (Kunzli, N, 2003; Brugge, D, 2007). In a cohort of 5000 adults followed up for 8 years, cardiopulmonary mortality was found to be associated with living near a major road (Hoek et al, 2002). Due to the diversity in people's daily activities (e.g., living or working in near-road buildings, driving or traveling on the roadways), it is important to characterize the spatial and temporal impacts of traffic-related emissions on near-road air quality, which is critical to assessing human exposure. Meanwhile, a better understanding in the physical and chemical mechanisms of vehicle exhaust plumes has the potential to mitigate the near-road air pollution through the vehicle emission control, the design of roadways and near-road infrastructures, transportation management and policy-making.

Regardless of their complexity, the nature of roadway-related environmental processes can be defined as turbulent reacting flows. For example, as an exhaust parcel emitted from the tailpipe disperses to the background, it experiences two very distinct turbulent mixing processes (Zhang and Wexler, 2004). First it is diluted by the strong turbulence generated by moving traffic, moving it from tailpipe to roadside (i.e., "tailpipe-to-road"), and then by atmospheric turbulence induced mainly by wind

and atmospheric instability, transporting it from roadside to the ambient ("road-to-ambient"). Aerosol dynamic processes such as nucleation, coagulation, condensation and evaporation are coupled with turbulent mixing to govern the evolution of exhaust particles (Zhang and Wexler, 2004). Gas-phase chemical reactions also couple with turbulent mixing. For instance, the conversion from freshly emitted nitrogen monoxide (NO) to nitrogen dioxide (NO_2) depends on mixing of nitrogen oxides (NOx), ozone (O_3), volatile organic compound (VOC) and free radicals on and near roadways (Wang et al., 2011b) or after being released from power plant stacks (Georgopoulos and Seinfeld, 1986). Therefore, advancing our understanding of turbulent reacting flows for those environmental processes is critical to characterizing the environmental impacts of air pollutants and developing effective mitigation strategies.

Figure 1.1. The highway intersectional micro-environment in suburban Rochester, NY (also shown in Chapter 5)

Initially funded by New York State Energy Research and Development Authority (NYSERDA), the main goal of my Ph.D. research is to investigate the air quality (especially the concentration of UFPs) in a highway intersectional micro-environment in suburban Rochester, NY, during the period of the shutdown of a coal-fired power plant and the adoption of ultra-low-sulfur diesel for on-road diesel vehicles, regulated

by United States Environment Protection Agency (USEPA), as described in detail in Chapter 5. However, the complicated domain of this micro-environment (including residential communities, schools, highway intersections, vegetation canopy and terrains, as shown in Figure 1.1) as well as the uncertainties in the traffic activities, emissions and aerosol dynamics of UFPs makes this turbulent reacting flow problem difficult to solve without understanding its basic mechanisms. Therefore, it is necessary to approach this project by understanding its individual components and advance my modeling capability incrementally:

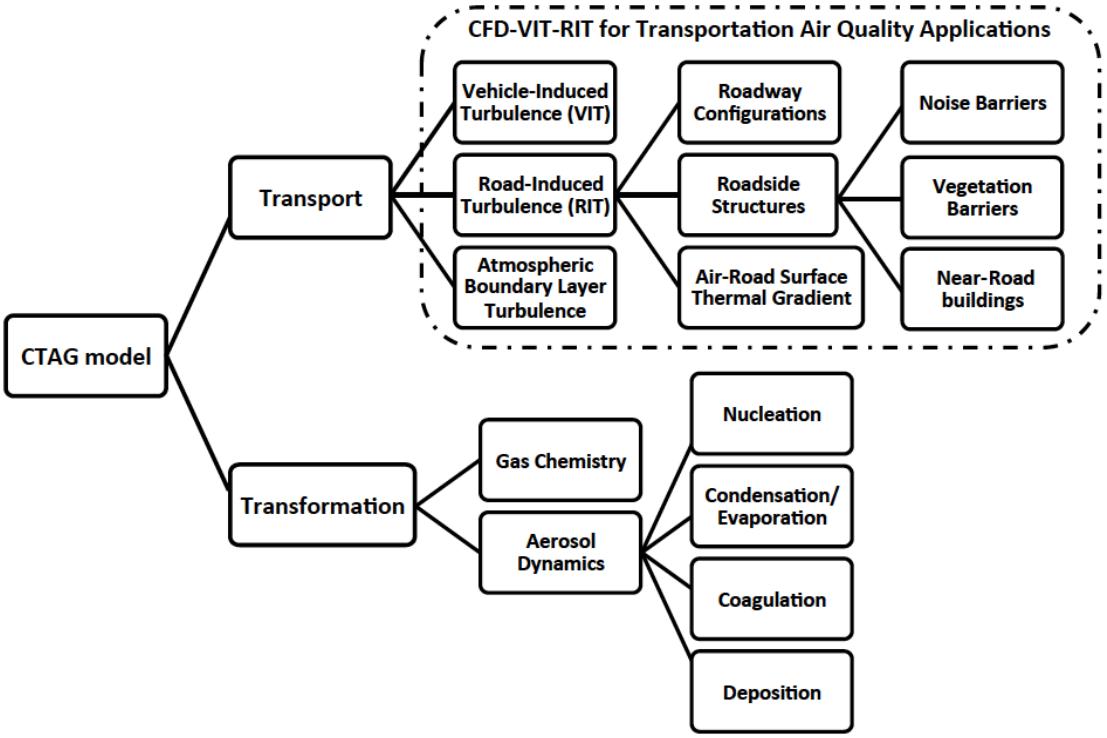

Figure 1.2. CTAG framework and components (also shown in Chapter 4)

I propose the concept of road-induced turbulence (RIT), which includes the turbulence induced by roadway configurations, roadside structures (e.g., noise barrier, vegetation barrier and near-road building) and air-road surface thermal gradient. I also

develop computational codes for the components that are important for the simulation of this intersectional micro-environment as well as other near-road environments and proposed an environmental turbulent reacting flow model, the Comprehensive Turbulent Aerosol Dynamics and Gas Chemistry (CTAG) model, as shown in Figure 1.2. CTAG is designed to simulate the transport and transformation of multiple air pollutants, e.g., from emission sources to ambient background. For the on-road and near-road applications, CTAG explicitly couples the major turbulent mixing processes, i.e., vehicle-induced turbulence (VIT), road-induced turbulence (RIT) and atmospheric boundary layer turbulence (ABLT) with gas-phase chemistry and aerosol dynamics (i.e., nucleation, condensation and evaporation, coagulation and deposition). The sources of models and concepts that form the CTAG model are listed in Table 1.1.

Table 1.1 List of sources of models and concepts that form the CTAG model

	Transport	Transformation
Models and concepts in CTAG framework that developed in this dissertation	Propose the concept of road-induced turbulence (RIT); Incorporate the major turbulence mechanisms: VIT, RIT and ABLT into near-road air quality study.	Integrated aerosol dynamics model
Models and concepts developed by other researchers that are incorporated into CTAG framework	VIT (Chock, 1980); ABLT (Singh et al., 2008);	Mechanisms of aerosol dynamics: Nucleation (Vehkamaki et al., 2003); Coagulation (Seinfeld and Pandis, 2006); Condensation, evaporation (Zhang et al., 2004); Deposition (Liu et al., 2011)
Capability of CFD solver, i.e., ANSYS FLUENT	Turbulence model: RANS model, e.g., k-epsilon; LES model	Mechanisms of multiple gaseous chemical reactions, e.g., Finite-Rate model

In the following chapters, the components that are created and summarized in the CTAG model are studied and evaluated by various field measurements with a gradual increase in the complexity of the simulations: We firstly study the turbulence characteristics (i.e., the vehicle-induced turbulence and road-induced turbulence) of the turbulent reacting flow without considering the chemical reactions and aerosol dynamics, i.e., the dispersion of an inert species, CO in the vicinity of two major highways (I-405 and I-710) with different configurations (e.g., I-405 is located on its embankment) in Los Angeles, CA, as discussed in Chapter 2 (shown in Figure 1.3a). Then we advance our capability to simulate the one-phase turbulent reacting flows by coupling the turbulent mixing with gas chemical reactions, i.e., modeling the evolution

of nitrogen oxides (e.g., NO_2) near roadways under multiple wind directions near Austin, TX in Chapter 3 (Wang et al., 2011b), shown in Figure 1.3b. Based on these attempts, in Chapter 4, we simulate a two-phase turbulent reacting flow by capturing the turbulence characteristics in the wake of a full-sized van with its trailer (Figure 1.4) and aerosol dynamics in the diluting exhaust plume of a diesel car (Figure 1.5) (Wang and Zhang, 2012). Meanwhile, I assisted my group members in the investigations on the near-road turbulence characteristics in complex domains: Steffens et al. (2012) explores the effects of a vegetation barrier on the particle size distributions in a near-road environment (near Highway 501) in Chapel Hill, NC (Figure 1.3c) and Tong et al. (2012) models the spatial variation of black carbon particles in an urban highway-building environment (near I-87) in New York, NY (Figure 1.3d), advancing our understanding in the turbulent reacting flows affected by near-road vegetation barrier, buildings and other structures.

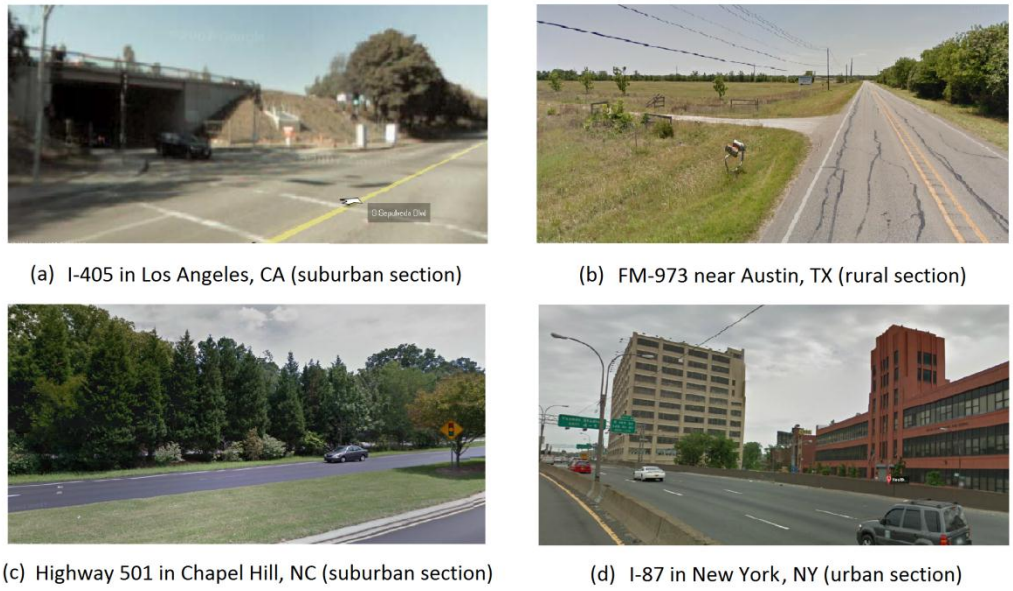

Figure 1.3. Views of field experimental locations near multiple highways (obtained from Google Maps)

Figure 1.4. A full-sized van with its trailer moving on an airport runway at Rockwood, TN. (Rao et al., 2002)

Figure 1.5. A European 2003 station wagon with the sampling inlet and sensor system of measurement devices mounted behind the vehicle (Uhrner et al., 2007)

To link the on-road vehicle emissions with the near-road dispersion for the micro-environment, in Chapter 5 we also implement a novel multi-scale structure (Figure 1.6) into the CTAG model based upon the mechanistic roadway air quality modeling framework proposed by Zhang and Wexler (2004). CTAG resolves the plume dynamics behind individual vehicles and the interactions of multiple plumes in the on-road domain (Scale I), as an emission model. The processed on-road emissions will

serve as inputs to the near-road domain simulations (Scale II), where CTAG resolves the dynamics of roadway plumes in the roadside micro-environment, as a dispersion model. The processed roadway plume profiles on the near-road domain can be potentially used as inputs to regional-scale air quality simulations (Scale III).

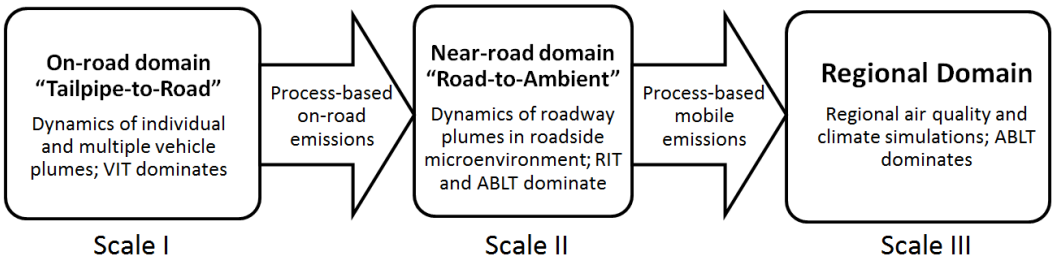

Figure 1.6. The multi-scale structure for the roadway air quality study, implemented in CTAG (also shown in Chapter 5)

These studies provide a solid foundation for the study of modeling multi-scale aerosol dynamics and micro-environmental air quality near the large highway intersection in suburban Rochester discussed in Chapter 5. They also imply that mitigating near-road air pollution through roadway and surrounding infrastructure designs might be useful when considered in the air pollution control and transportation management and policy-making.

Besides the dispersion of pollutants, traffic emission inventory is also important, since on-road vehicle emissions are the main source that dominates the air quality in near-road environments (Burtscher, 2005; Lipsky and Robinson, 2005). Therefore, reducing the uncertainties associated with the emission measurements is important to control air pollution and mitigate human exposure.

The dilution systems are essential to almost all emission testing procedures and major combustion sources (Lipsky and Robinson, 2005; Brockmann et al., 1984; Hildemann et al., 1989). Therefore, the turbulent reacting flows inside the fabricated dilution systems are also investigated in this dissertation. These flows share the same governing mechanisms with the atmospheric turbulent reacting flows found in near-road environments.

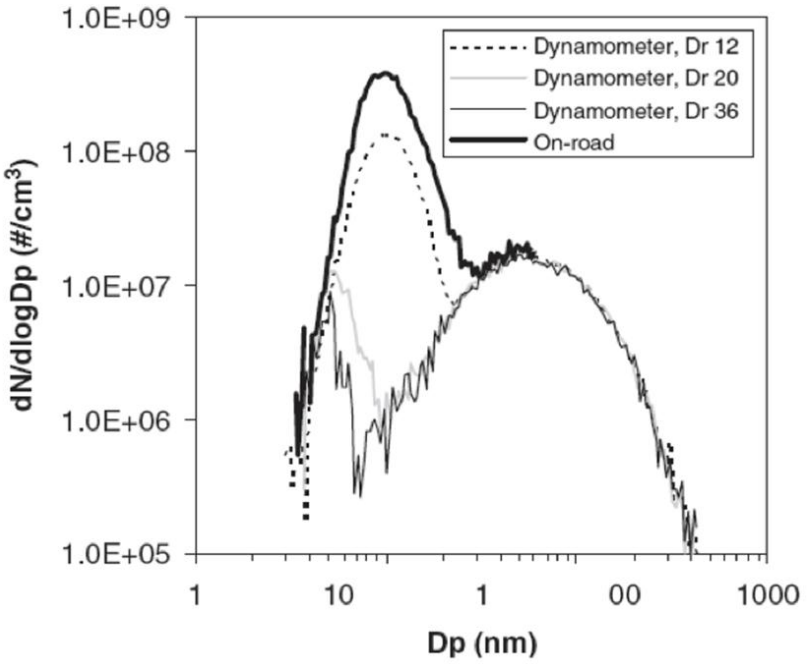

Figure 1.7. Laboratory emission measurements may differ considerably from on-road emissions depending on chosen dilution parameters (Ronkko et al., 2006)

The fabricated dilution systems have been widely used for various purposes: 1) to capture the atmospheric dilution, especially for establishing a link between the atmospheric dilution and the undiluted exhaust, as shown in Figure 1.7 (Lyyranen et al., 2004; Ronkko et al., 2006); and 2) to preserve the exhaust properties as unbiased as possible from the measurement and dilution setup artifacts to produce a so called

"tailpipe-level" emissions as observed inside the exhaust pipe (Strand et al., 2004). For either purpose, the current dilution samplings have many known limitations and those limitations are pronounced for measuring the semi-volatile composition and the ultrafine range (<100 nm) of the particulate emissions. Meanwhile, the design and operation parameters of the dilution systems can strongly affect their functionality and the measurement results, as illustrated in Figure 1.8. Therefore, the CTAG model is utilized to investigate the effects of turbulent mixing on particulate emission measurements within multiple types of dilution systems (Figure 1.9 and 1.10) in Chapter 6, which have the potential to develop strategies to reduce the uncertainties associated with dilution samplings and define a standardized dilution sampling methodology for characterizing emissions from multiple combustion sources.

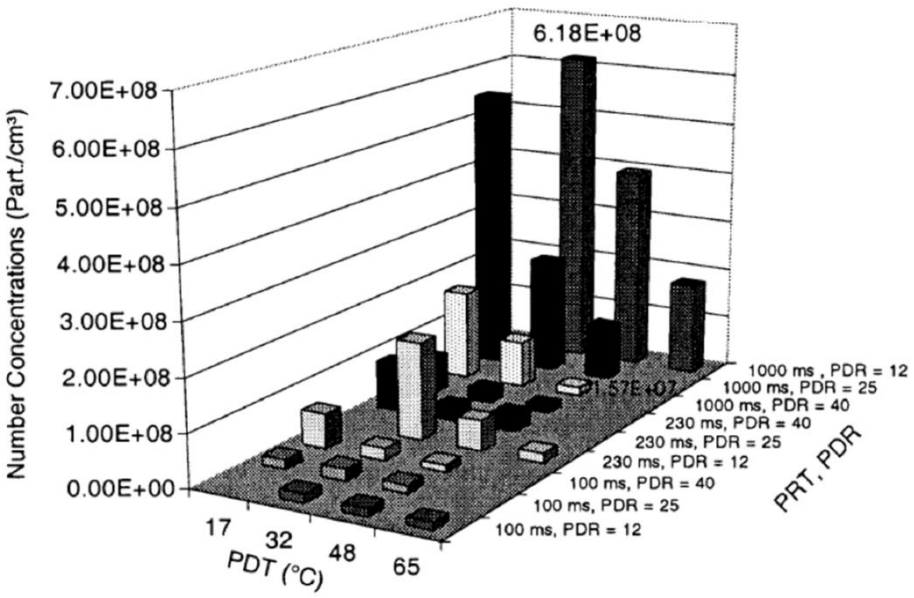

Figure 1.8. Dilution parameters such as residence time, dilution temperature, and dilution ratio have a strong influence on particle number concentrations (Abdul-Khalek et al., 1999)

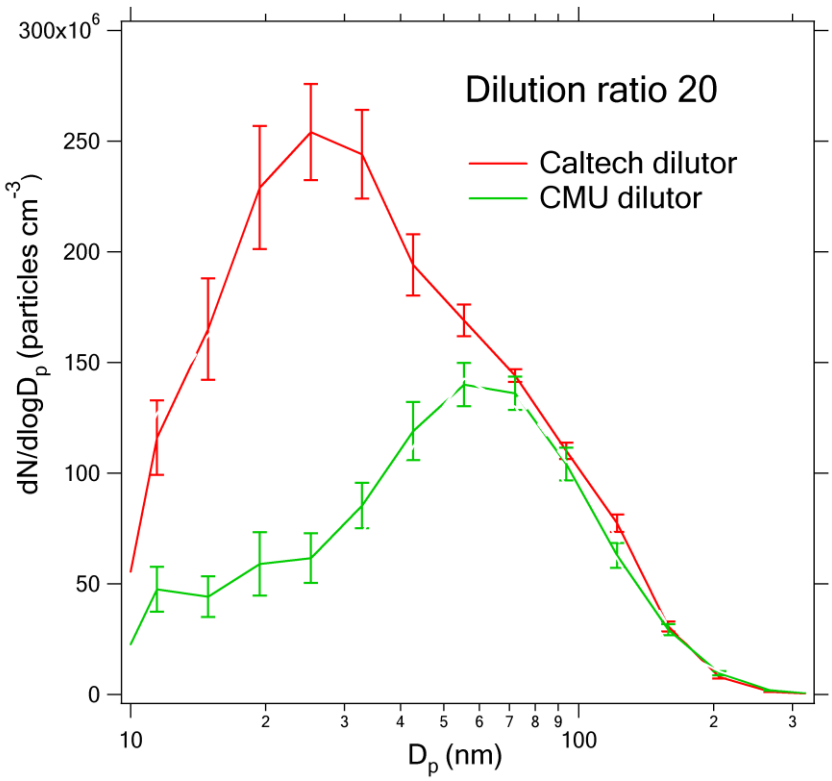

Figure 1.9. Dilution-corrected number size distributions measured during the diesel intercomparison experiments between the Caltech dilutor and CMU dilutor under the dilution ratio = 20 (also shown in Chapter 6)

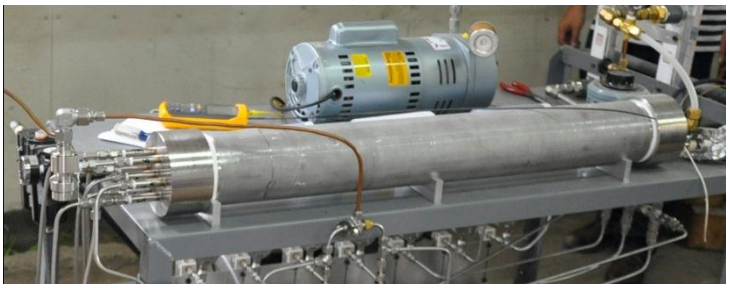

Figure 1.10. The CMU-type dilution system

Contributions of my Ph.D. research, personal experience and the future directions of my work are discussed in Chapter 7. In particular, the CTAG model can also be deployed in a wide range of applications beyond on-road vehicle emissions, such as

the air quality issues regarding the emissions from aircrafts, cargo ships, locomotives and coal-fired power plants. It is important for us to have a better understanding of the emission and dispersion of multiple pollutants from these major combustion sources which can be crucial to policy-making and multi-scale design, mitigating air pollution to benefit the health of people who work or live nearby.

CHAPTER 2

MODELING THE EFFECT OF TURBULENCE IN PREDICTING THE NEAR-ROAD AIR QUALITY USING THE CTAG MODEL*

Abstract

It is well recognized that dilution is an important mechanism governing the near-road air pollutant concentrations. In this chapter, we aim to advance our understanding of turbulent mixing mechanisms on and near roadways using computation fluid dynamics (CFD). Turbulent mixing mechanisms can be classified into three categories according to their origins: vehicle-induced turbulence (VIT), road-induced turbulence (RIT) and atmospheric boundary layer turbulence (ABLT). RIT includes the turbulence generated by road embankment, road surface thermal effects and roadside structures. Both VIT and RIT are affected by the roadway designs. We incorporate the detailed treatment of VIT and RIT into the CFD (namely CFD-VIT-RIT, which is the transport part of the CTAG model) and apply the model in simulating the spatial gradients of carbon monoxide (CO) near two major highways with different traffic mix and roadway configurations. The modeling results are compared to the field measurements and those from CALINE4 and CFD without considering VIT and RIT. We demonstrate that the incorporation of VIT and RIT considerably improves the modeling predictions, especially on vertical gradients and seasonal variations of carbon monoxide. Our study implies that roadway design can significant influence the

*Wang, Y., Zhang, K. M. Modeling near-road air quality using a computational fluid dynamics model, CFD-VIT-RIT. Environmental Science & Technology. 2009, 43: 7778-7783.

near-road air pollution. Thus we recommend that mitigating near-road air pollution through roadway designs be considered in the air quality and transportation management. In addition, thanks to the rigorous representation of turbulent mixing mechanisms, CTAG can become valuable tools in the roadway designs process.

2.1 Introduction

Elevated air pollutants concentrations have been measured in congested urban areas and near roadways (Hagler et al., 2009; Westerdahl et al., 2009), which have been associated with adverse human health effects (Samet, 2007). These effects vary with levels of human exposure to traffic-related air pollutants through different activities (e.g., driving on the road, living/working near or away from the road) (Peters et al., 2004; McConnell et al., 2006). Therefore, it is important to understand the spatial gradient of pollutants near roadways, which requires measurements and simulations addressing complex road configurations and meteorological conditions (Baldauf et al., 2008; Riddle et al., 2004).

Dilution is the dominant mechanism for changing the near-road concentrations. Pollutant dispersion near roadways usually experiences two distinct stages -- 'tailpipe-to-road' and 'road-to-ambient' (Zhang and Wexler, 2004). The dilution ratio of the first stage usually reaches up to about 1000:1 in around 1-3 s; for the second stage, the dilution ratio is usually about 10:1, and the process usually lasts around 3-10 min (Zhang and Wexler, 2004). The aerosol processes such as nucleation, condensation and coagulation are strongly coupled with dilution (Zhang and Wexler, 2004). For nitrogen oxides (NO_x), the concentrations change results from the coupling of dilution

and chemical reactions (Fraigneau et al., 1995). For carbon monoxide (CO), an inert species under typical atmospheric conditions, dilution is the only governing mechanism. Therefore CO is usually used as a dilution indicator since it comes mostly from vehicle exhaust, and can be easily measured (Zhang et al., 2004).

Dilution is caused by on-road and near-road turbulent mixing. Given the importance of dilution on near-road air quality, it is imperative to gain a better understanding of the mechanisms contributing to the turbulent mixing. Several mechanisms affect the generation of turbulence near roadways besides atmospheric boundary layer turbulence (ABLT) (Singh et al., 2008). Firstly, the movement of vehicles on the road results in a significant increase in turbulence, which is known as vehicle-induced turbulence (VIT) (Chock, 1980). Secondly, turbulence can be generated by the embankment on which a roadway is located when wind flows over it (Hauf and Neumannhauf, 1982). Thirdly, thermal effects caused by solar radiation generate turbulence during hot season and cannot be ignored for pollutant dispersion (Kim and Baik, 2001; Sini et al., 1996; Xie et al., 2005). Fourthly, road structures (i.e., noise barrier, tree planting) can also produce turbulence that influences the flow field (Baldauf et al., 2008; Gromke et al., 2008; Lidman, 1985). Since these three effects can be attributed to roadway design, we refer to them as RIT.

Gaussian plume-based dispersion models such as CALINE4 have been widely used to assess the pollutant concentrations of urban road environments (Benson, 1992; Cook et al., 2008; Venkatram et al., 2004). These models typically treat the region directly above the roadway and at prescribed distances on each side of the roadway as a zone of uniform emissions and turbulence called a “mixing zone” (Benson, 1992).

The introduction of the "mixing zone" concept is equivalent to a fixed VIT, i.e., not adjustable to the specific roadway conditions (e.g. the different vehicles speeds and types). Their dispersion parameterizations are based in part on roadway geometry and wind direction but they face the challenge of how to incorporate the effect of road configurations exactly (Rao et al., 2002; Coe et al., 1998; Benson, 1992; Sahlodin et al., 2007). In recent years, computation fluid dynamics (CFD) has been applied in modeling the dynamical and mechanical processes taking place in complicated urban street canyons and road tunnels (Kim and Baik, 2001; Katolicky and Jicha, 2005; Xie et al., 2007). However, it has been rarely applied to simulate near-road air quality and the comprehensive representation of VIT and RIT is scarce (Sahlodin et al., 2007; Liu and Ahmadi, 2005).

In this chapter, we aim to investigate the effects of different turbulent mixing mechanisms on dilution near roadways. The CTAG model with detailed treatment of VIT and RIT (i.e., CFD-VIT-RIT) is used to simulate the horizontal and vertical dispersions of CO in the vicinity of two highways during two seasons, and is compared with field measurements, CALINE4 and CFD (consider no VIT and RIT). The implications of our findings on future road design and the advantages and disadvantages of applying different dispersion models are also discussed here.

2.2 Mechanisms for on-road and near-road turbulences generation

In this section, we provide a brief summary of the mechanisms that generate VIT and RIT in on-road and near-road environments.

2.2.1 Turbulence induced by vehicles

Traffic has a dominant effect in the immediate vicinity of the roadway (Rao et al., 2002). Moving vehicles enhance mixing processes by inducing turbulence, which originates from the interaction between moving vehicles and ambient air. It is known that up to 50% of kinetic energy is converted into additional turbulence when a fluid hits an obstacle (Katolicky and Jicha, 2005). The wakes behind moving vehicles are characterized as momentum wakes and contain organized trailing vortices which play a key role in determining the flux of kinetic energy and rapidly mix the pollutants released in the turbulent wake (Rao et al., 2002; Ozdemir and Ozdemir, 2004; Kozaka et al., 2004). VIT, which is strongly related to vehicle type and speed (Sahlodin et al., 2007; Baumer et al., 2005; Kalthoff et al., 2005), can be expected to significantly influence the diffusion of roadway emissions, especially in the microenvironment near roadways (Chock, 1980; Rao et al., 2002; Baumer et al., 2005). VIT increases with an increase in vehicle speed, indicating increased wake production of turbulence (Rao et al., 2002). Experiments also showed that compared with gasoline cars, heavy-duty diesel trucks induce more turbulence due to its size and structure (Kalthoff et al., 2005).

2.2.2 Turbulence induced by an embankment

An embankment acts as a topographic obstacle which causes a form drag and produces turbulence to compensate for the deformation of the flow field when wind

flows over it (Garbrecht et al., 1999). A recirculation cavity is created downwind of the embankment, containing a well-mixed, and often lower, zone of pollution concentrations (Kim and Patel, 2000). The induced turbulence depends on the wind velocity, wind direction, the height and the shape of the embankment (Hauf and Neumannhauf, 1982; Baumer et al., 2005).

2.2.3 Turbulence induced by thermal effects on road surface

The available solar radiation on a surface, Q_0, can be divided into turbulent fluxes of sensible heat, H_0, latent heat, V_0, and the soil heat flux, B_0 (Kalthoff et al., 2005). With high absorptivity and low heat capacity, the asphalted surface of roadway receives much net energy. Compared to the grassy or concrete surroundings, it provides a very small latent heat flux and leads to an increased sensible heat flux, which generates turbulence. The thermally induced flow is combined with mechanically induced flows, and affects the transport of pollutants. It should be noted that due to the large solar zenith angle in the winter, the road surface receives much less direct solar radiation, so the temperature difference between road surface and air can be neglected.

2.2.4 Turbulence induced by roadside structures

Roadside structures affect pollutant concentrations around the structure by blocking initial dispersion, and increasing turbulence and initial mixing of the emitted

pollutants (Baldauf et al., 2008; Gromke et al., 2008; Lidman, 1985). A noise barrier disturbs the wind field as a still obstacle while a tree planting consisting of branches and leaves can be considered as a porous body (Baldauf et al., 2008; Gromke et al., 2008). It has been shown that the plume behind noise barrier and vegetation is relatively uniform and vertically well-mixed, and pollutant concentrations are reduced under certain meteorological conditions. With winds directionally from the road, concentrations of CO and particle concentrations generally decrease between 15 and 50% behind the noise barrier (Baldauf et al., 2008).

2.3 Field measurements

The experimental data are collected from previous measurements near Interstate 405 (I-405) and Interstate 710 (I-710) in Los Angeles in the summer and winter (Zhang et al., 2004; Zhang et al., 2005; Zhu et al., 2002a; Zhu et al., 2004; Zhu et al., 2005). I-405 is 30 m wide, with an embankment of 4.5 m-height, while I-710 is 26 m wide at ground level. The horizontal sampling points are taken within 300 m downwind and upwind from the center of the highways at height 1.6 m. Meanwhile, the vertical CO concentrations at different heights are measured at 50 m downwind of I-405 in the summer. There are relatively large differences in temperature, but small differences in wind speed and vehicle volume for each highway between different seasons. For I-405, gasoline cars dominate the vehicle mix, while for I-710, more than 25% of the vehicles are heavy-duty diesel trucks. All related conditions are considered in our simulation. More meteorological and road data are listed in Table 2.1.

Table 2.1 Meteorological parameters and road conditions collected during field experiment

Parameters	I-405		I-710	
	Summer	Winter	Summer	Winter
Temperature (℃)	30.3	23.2	30.3	23.2
Relative humidity (%)	66.4	43.1	66.4	43.1
Solar zenith angles (°)	25.1	64.4	25.1	64.4
Wind velocity (m s^{-1})	1.5	1.4	1.3	1.2
Wind direction to highways (°)	90	90	90	90
Wind deviation (°)	23	23	45	45
Stability class	unstable	neutral	unstable	Neutral
Traffic volume (vehicles min^{-1})	231	236	203	200
Heavy-duty truck percentage	5-6%	5-6%	25-30%	25-30%
Upwind CO concentration (ppm)	0.1	0.2	0.1	0.2

For I-405 study, wind speed and directions were measured 6 m above ground level 30 m downwind of the highway. For I-710 study, wind speed and direction were measured at 6 m above the ground level 20 m downwind of the highway. The detailed measurements were described in Zhu et al. (2002a; 2002b).

2.4 The CTAG model

The standard $k-\varepsilon$ turbulence model available in the CFD code, ANSYS FLUENT, is used for modeling flow and dispersion in the vicinity of roadways. It is probably the most widely documented and validated CFD turbulence model currently available (Lien et al., 2004). It represents the effects of turbulence by including two more variables: the turbulent kinetic energy (TKE), k, and its dissipation rate, ε. These two quantities are treated as variables in transport equations, which have to be solved together with Reynolds-averaged Navier-Stokes (RANS) equations, involving

continuity, momentum, energy and pollutant concentration conservation for a steady, incompressible fluid flow. The governing equations are as follows:

- Momentum equation:

$$u_j \frac{\partial(\rho u_i)}{\partial x_j} = \rho\left(\frac{\rho-\rho_n}{\rho_n}\right) g_i - \frac{\partial p}{\partial x_i} + \frac{\partial}{\partial x_j}\left(\mu\left(\frac{\partial u_j}{\partial x_i}+\frac{\partial u_i}{\partial x_j}\right) - \rho u_i^{'} u_j^{'}\right) \tag{2.1}$$

where

$$-\rho_j u_i^{'} u_j^{'} = \mu_t\left(\frac{\partial u_i}{\partial x_j}+\frac{\partial u_j}{\partial x_i}\right) - \frac{2}{3}\rho k \delta_{ij} \tag{2.2}$$

$$\mu_t = \rho C_\mu \frac{k^2}{\varepsilon} \tag{2.3}$$

The first term on the right-hand side represents the air motions induced by buoyancy force. When solar radiation heats the asphalt road surface, air density changes due to the increase of the air temperature near the ground. The rate change in the air density due to an increase in temperature is estimated by:

$$\frac{\rho-\rho_n}{\rho_n} = -\beta(T-T_n) \tag{2.4}$$

where β is the coefficient of thermal expansion, T is the temperature, ρ_n and T_n are the density and temperature of the ambient air, respectively.

- Pollutant concentration equation:

$$\frac{\partial(\rho u_i C_i)}{\partial x_i} = \frac{\partial}{\partial x_i}\left(\rho D_{i,m} + \frac{\mu_t}{Sc_t}\right)\frac{\partial C_i}{\partial x_i} + S_i \tag{2.5}$$

where C_i is the concentration of the i th species, S_i is the mass rate of creation or depletion of the i th species, and $D_{i,m}$ is the diffusivity coefficient of i th species in the mixture. $Sc_t = 0.7$ is the turbulent Schmidt number.

- Turbulent kinetic energy (TKE) k and dissipation ε equations are:

$$\frac{\partial(\rho k u_i)}{\partial x_i} = \frac{\partial}{\partial x_j}\left[\left(\mu + \frac{\mu_t}{\sigma_k}\right)\frac{\partial k}{\partial x_j}\right] + P_k + G_b - \rho\varepsilon \tag{2.6}$$

and

$$\frac{\partial(\rho\varepsilon u_i)}{\partial x_i} = \frac{\partial}{\partial x_j}\left[\left(\mu + \frac{\mu_t}{\sigma_\varepsilon}\right)\frac{\partial \varepsilon}{\partial x_j}\right] + G_{1\varepsilon}\frac{\varepsilon}{k}(P_k + C_{3\varepsilon}G_b) - C_{2\varepsilon}\rho\frac{\varepsilon^2}{k} \tag{2.7}$$

$$G_b = -\beta g_i \frac{\mu_t}{Pr_t}\frac{\partial T}{\partial x_i} \tag{2.8}$$

$$\mu_t = \rho C_\mu \frac{k^2}{\varepsilon} \tag{2.9}$$

$$P_k = \mu_t \frac{\partial u_j}{\partial x_i}\left(\frac{\partial u_i}{\partial x_j} + \frac{\partial u_j}{\partial x_i}\right) \tag{2.10}$$

where μ_t is the turbulent viscosity, μ is the laminar viscosity, g_i is the gravitational acceleration in the i th direction coordinate, $(0,-g,0)$, G_b is the turbulence production due to buoyancy and P_k is the generation of turbulent kinetic energy due to the mean velocity gradients.

The model constants for standard $k-\varepsilon$ turbulence model are:

$$C_\mu = 0.09,\ \sigma_k = 1.0,\ \sigma_\varepsilon = 1.3,\ C_{1\varepsilon} = 1.44,\ C_{2\varepsilon} = 1.92,\ C_{3\varepsilon} = 1.44 \tag{2.11}$$

The governing equations are discretized using the finite volume method and the SIMPLE algorithm is used to solve the equations.

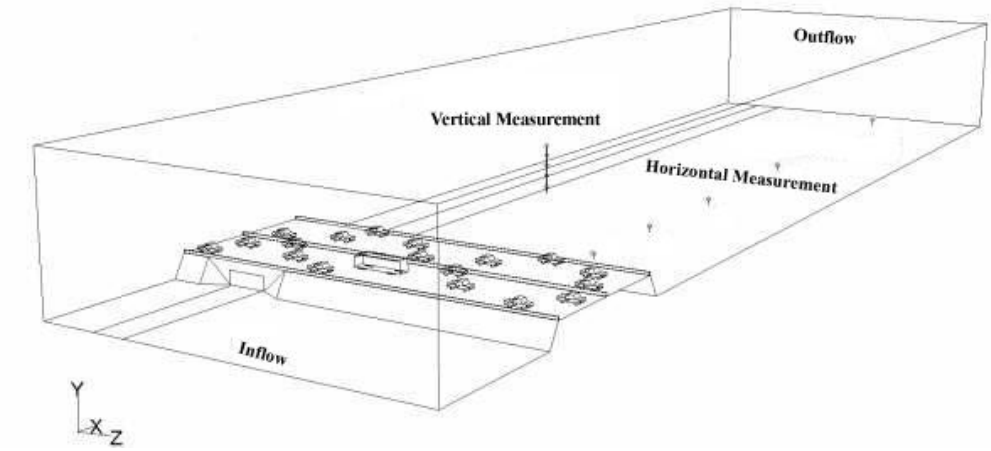

Figure 2.1. Geometric features of the computational domain for I-405

Figure 2.1 shows the computational domain of I-405 and the sketch of measurement locations. The number of computational cells used for the simulation is 2,305,712, with a size of the solution domain of 380 m by 80 m in the horizontal and 30 m in the vertical direction. The computational domain for I-710 is similar, except that the highway is not located on an embankment. The spatial domain has a size of 380 m by 40 m in the horizontal and 30 m in the vertical direction and is divided into 1,063,541 unstructured cells.

Test zones above road surface (shown in Figure 2.2) are created to obtain average turbulent kinetic energy (TKE). Different heights of the domain are set according to the heavy-duty truck percentage. Since most of the vehicles are cars and vans for I-405, the height of the zone is 2.5 m, while for I-710, the height is 3.5 m since it is a major truck route.

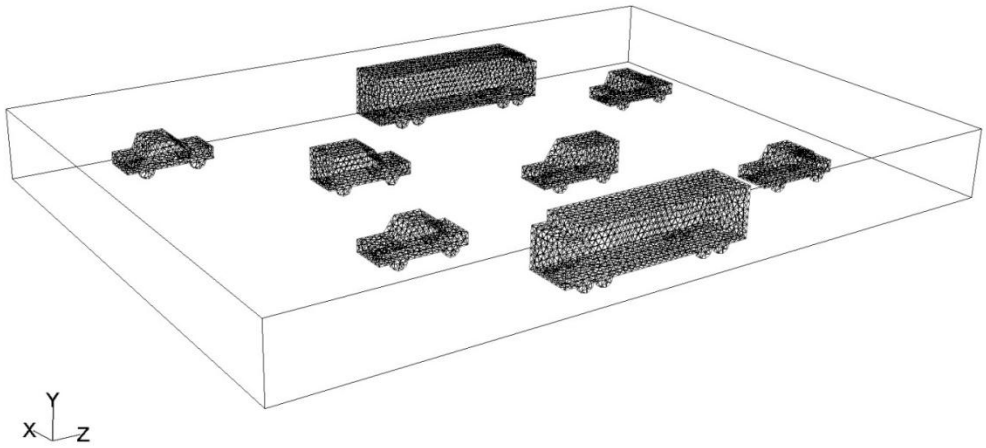

Figure 2.2. Sketch of three-dimension elements for I-710

We model the vehicles as real-shaped rather than block-shaped to keep the conditions similar to the streamlined shape of real vehicles (Sahlodin et al., 2007), shown in Figure 2.2, since the turbulence for the block-shaped vehicle is estimated to be 25% higher than for the true vehicle models (Thompson and Eskridge, 1987). Different types of vehicles are built approximately following their actual sizes. Since the average vehicle speed, 24 m s^{-1}, is measured during the experiments (Zhang et al., 2005), the same moving speed for all vehicles is adopted in the simulation (Gidhagen et al., 2004). For the vehicle surface, an equivalent roughness height of 0.0015 m is chosen to match the simulated drag force of vehicles with the value based on drag coefficient (White, 2002). The exhaust pipe is modeled as a small area on the back of the light-duty vehicle or on the top of the heavy-duty diesel vehicles. Since traffic volumes change little between seasons, just one set of vehicles is built for each highway. The embankment for I-405 is built corresponding to its real size (in Figure 1). All the solid boundaries, including ground surfaces and vehicle surfaces, are

specified as non-slip boundary conditions in the flow module and are prescribed at a fixed temperature in the heat transfer module. Symmetric boundary conditions (zero gradient normal to boundary) are applied to the top and side faces of the domain.

Based on a meteorological study in Los Angeles (Terjung and Orourke, 1982), the temperature difference between air and roadway surface is estimated to be 20 ℃ for the summer season under strong solar radiation. Considering the atmospheric wind in two seasons, fully developed in-flow vertical profiles for ABLT are incorporated through User-Defined Function to describe the fully developed vertical profile of inlet wind flow (Blocken et al., 2007). The wall functions of wind velocity, u, turbulent kinetic energy, k and its dissipation rate, ε are specified as:

$$u = u_r \left(\frac{y}{y_r} \right)^p \tag{2.12}$$

where p depends on atmospheric stability and surface roughness, u_r is the reference velocity, and y_r is the reference height.

$$k = \frac{u_*^2}{\sqrt{C_\mu}} \tag{2.13}$$

$$\varepsilon = \frac{u_*^3}{\kappa y} \tag{2.14}$$

where u_* is the friction velocity, and κ is the von Karman constant.

When the atmospheric stability is neutral (stability class D),

$$u_* = \kappa u_r \left[\ln\left(\frac{y_r}{z_0} \right) \right]^{-1} \tag{2.15}$$

or when the atmospheric stability is unstable (stability class A or B),

$$u_* = \kappa u_r \left\{ \ln\left(\frac{y_r}{z_0}\right) + \ln\left[\frac{(\eta_0^2+1)(\eta_0+1)^2}{(\eta_r^2+1)(\eta_r+1)^2}\right] + 2(\tan^{-1}\eta_r - \tan^{-1}\eta_0) \right\}^{-1} \quad (2.16)$$

$$\eta_r = \left[1 - 15\frac{y_r}{L}\right]^{1/4} \quad (2.17)$$

$$\eta_0 = \left[1 - 15\frac{z_0}{L}\right]^{1/4} \quad (2.18)$$

where z_0 is the roughness length, and L is the Monin-Obukhov length. For flat terrain simulations, the boundary layer structure is defined in terms of the Monin-Obukhov length, boundary layer height and surface roughness (Seinfeld and Pandis, 2006).

In summary, we incorporate the turbulence induced by moving traffic, embankment, thermal effects and atmospheric wind into our model. Since there are no noise barriers and few trees in the surrounding of I-405 and I-710, turbulence generated by the road barriers and trees is not simulated here, and will be investigated in future studies.

2.5 Results

2.5.1 TKE results

Table 2.2 Summary of TKE in the test zone

		I-405				I-710			
		Summer	Percentage	Winter	Percentage	Summer	Percentage	Winter	Percentage
VIT[a]:		0.36	41.4%	0.35	53.9%	0.63	76.8%	0.63	95.5%
RIT[a]	Embankment:	0.30	34.5%	0.27	41.5%	N/A	N/A	N/A	N/A
	Road surface thermal effects:	0.17	19.5%	N/A	N/A	0.15	18.3%	N/A	N/A
ABLT[a]:		0.04	4.6%	0.03	4.6%	0.04	4.9%	0.03	4.5%
Total TKE[a]:		0.87	100.0%	0.65	100.0%	0.82	100.0%	0.66	100.0%

[a]Unit is $m^2 s^{-2}$

Induced TKE within the test zone is summarized in Table 2.2. From Table 2.2, it is clear that total TKE changes with seasons and highways and the largest TKE is obtained from I-405 with the embankment in the summer. The produced VIT, especially for I-710, is dominated over ABLT, as suggested by previous wind tunnel studies (Khare et al., 2005). Due to the large percentage of heavy-duty trucks, VIT of I-710 is much larger than that of I-405. Excellent agreements are found for VIT between our model (0.36 $m^2 s^{-2}$ for I-405 and 0.63 $m^2 s^{-2}$ for I-710) and the empirical formula (0.37 $m^2 s^{-2}$ for I-405 and 0.64 $m^2 s^{-2}$ for I-710) reported by Baumer et al. (2005). TKE produced by embankment, ~ 0.30 $m^2 s^{-2}$, or 34.5% of the total TKE in the test zone, is also in good agreement with the value, 0.34 $m^2 s^{-2}$, calculated from the empirical formula in Baumer et al. (2005). The large contribution of embankment-induced TKE implies that elevated highways enhance turbulent mixing downwind, potentially reducing human exposure to traffic-generated air pollutants. Furthermore,

TKE caused by the thermal effects due to road surface properties accounts for about 20% of total TKE in the test zone and therefore cannot be ignored.

A comparison simulation of on-road TKE is also conducted with another method (described in detail in Chapter 4): the on-road vehicles are set to be stationary, while the inlet air is blowing towards the vehicles. The surfaces of the vehicles are set as "wall", for which a no-slip condition has to be satisfied. The inlet wind velocity is taken as the sum of the vehicle velocity and ambient wind velocity. In addition, the roadway surface is set to have the same velocity as the on-road vehicles to avoid generating the ground surface boundary layer artificially. The RNG $k-\varepsilon$ turbulence model is used in the comparison simulation, since it has been used to capture the turbulence characteristics in the wake of a full-sized van and evaluated by field measurement data in Chapter 4. The simulated TKE in the test zone for I-405 is 0.34 $m^2 s^{-2}$, while for I-710 is 0.58 $m^2 s^{-2}$, which are both close to the method of simulating moving vehicles with the standard $k-\varepsilon$ turbulence model.

Table 2.3 Comparison of the simulations of on-road VIT

		VIT ($m^2 s^{-2}$)	
		I-405	I-710
Method I	Moving vehicles (Standard k-epsilon model)	0.36	0.63
Method II	Stationary vehicles with incoming wind (RNG k-epsilon model)	0.34	0.58
	Difference (based on Method II)	5.9%	8.6%

It should be noted that the main advantage of our model over the empirical formula is its capability to resolve the effects of VIT and RIT over the near-road region beyond the test zone. Our simulations show that TKE reaches the maximum

value on road, and decays with the increasing distance from the highway, until at 300 m it is negligibly small. Due to a large turbulence dissipation rate, VIT, averaged from the ground to the height of the test zone, drops to below 50% at about 20 m downwind of highway. When wind velocity increases, VIT dissipates faster but is also transported to a greater horizontal distance. When wind velocity is small, VIT can spread to higher elevation. RIT decreases slower than VIT, due to the big size of the embankment which results in a larger influence range. For I-405, the ratio of VIT to RIT decreases with the increasing distance.

2.5.2 Spatial gradients of carbon monoxide concentrations

In this section, we compare the simulated CO concentrations in both horizontal and vertical directions against the field measurement data. In addition to the CTAG model, we also present the results from CALINE4 and a standard CFD model. In the standard CFD model, referred to as "CFD" in the text, the highways are treated as elevated line sources without explicit treatment of VIT and RIT. We use 405S, 405W, 710S and 710W to refer to the studies of two different highways (i.e., I-405 and I-710) at two seasons with "S" and "W" representing summer and winter, respectively.

While the spatial gradients of near-road concentrations of inert species such as CO are determined by turbulent mixing, the absolute concentrations are determined by both vehicle emission factors and turbulent mixing. Since the emission factors derived by models such as MOBILE6 and EMFAC have known discrepancies in representing real-world emission factors (Cook et al., 2007; Ban-Weiss et al., 2008), our comparisons focus on the relative concentrations of CO, thus avoiding the additional

uncertainties introduced by the emission factor models. The CO concentrations at downwind distances are normalized by their values at the closest distances to the roadways, i.e., 30 m for I-405 and 17 m for I-710, respectively. For instance, the relative CO concentrations at 30 m from I-405 are unity for both measurements and modeling results. However, the concentrations at 60 m, 90m, 150m and 300 m vary depending on measurements and selected models.

2.5.3 Horizontal gradients and seasonal variations

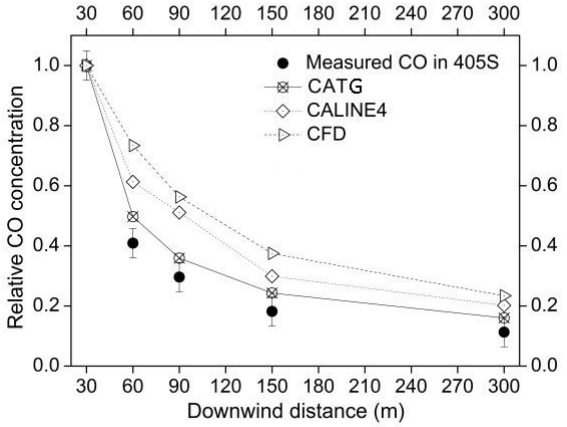

(a)

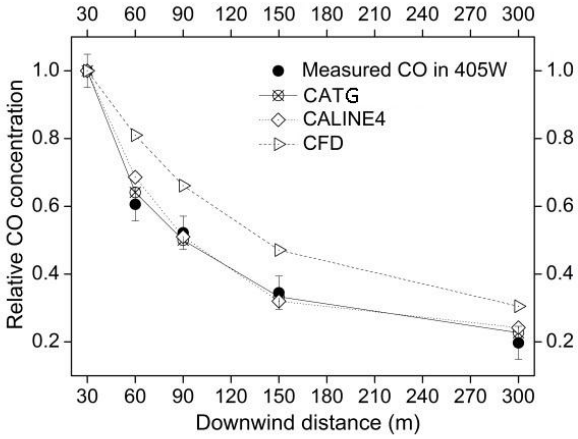

(b)

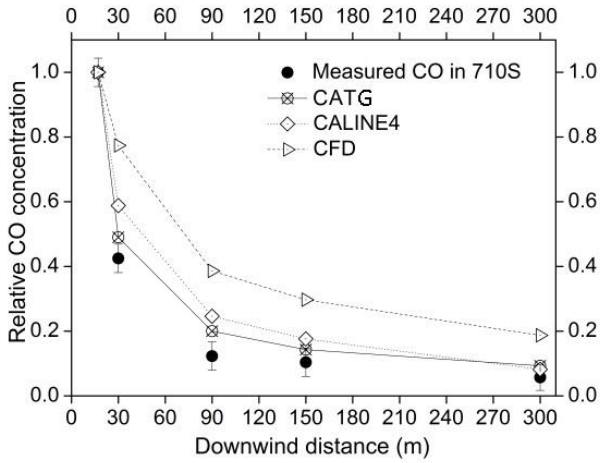

(c)

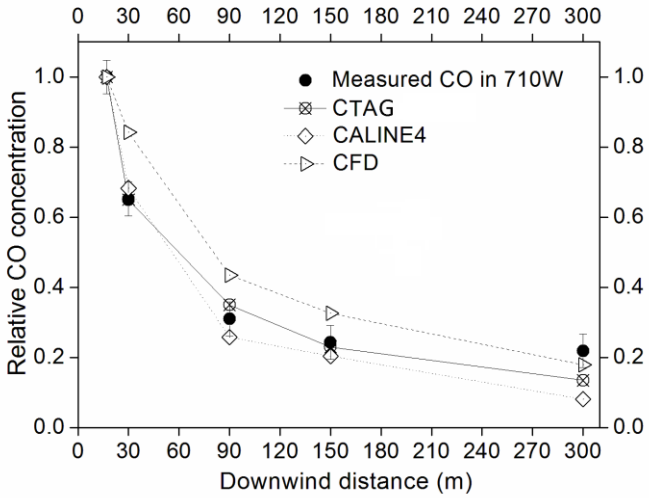

(d)

Figure 2.3. Comparison of relative CO concentrations between models and field experiment for I-405 in (a) summer and (b) winter and for I-710 in (a) summer and (d) winter

Figure 2.3(a) compares the simulation results obtained from CTAG, CALINE4 and CFD models to the measurement data for I-405 in the summer. Relative CO concentration decays exponentially when moving away from the traffic source. The dilution between 30 m and 60 m varies with different models: CALINE4 and CFD underpredict more than 33% compared to measurement data, while CTAG reduces the

error to less than 15%. In Figure 2.3(b), since turbulence induced by the road surface thermal effects can be ignored in the winter, the differences in CALINE4 and CTAG predictions are relatively small. However, CFD still shows big error due to no-consideration of VIT and RIT. The simulation results for I-710 in the summer and winter are shown in Figure 2.3(c) and Figure 2.3(d). The improvement of predictions by CTAG over CFD and CALINE4 on I-710 can be attributed to the detailed treatment of VIT and RIT.

Table 2.4 RMS of relative CO concentration and dilution ratio between 30 m and 150 m

		Measurement	CTAG	CALINE4	CFD
405S Horizontal	30 m/ 150 m	5.5	4.11	3.34	2.67
	RMS	N/A	0.065	0.186	0.270
405W Horizontal	30 m/ 150 m	2.89	3.00	3.13	2.12
	RMS	N/A	0.031	0.052	0.162
710S Horizontal	30 m/150 m	4.12	3.43	3.32	2.61
	RMS	N/A	0.064	0.124	0.277
710W Horizontal	30 m/150 m	2.78	2.83	3.37	2.58
	RMS	N/A	0.024	0.042	0.131
405S Vertical	RMS	N/A	0.059	0.246	0.213

The horizontal dispersion of CO is determined mainly by wind velocity and turbulence (Zhu and Hinds, 2005). To compare near-road dispersions for both I-405 and I-710 in different seasons, we introduce a parameter called the dilution ratio, which is the ratio of background-subtracted CO concentrations at 30 m and 150 m, listed in Table 2.3. The root mean square (RMS) of measured and simulated relative CO concentrations at 60 m, 90, and 150 m for I-405 and 30 m, 90 m, and 150 m for I-710, respectively, is also shown in Table 2.3. More details can be found in Zhang et al. (2004). From Table 2.3, it is clear that due to the thermal effects, dilution ratios

between 30 m and 150 m in the summer are much larger than those of winter for both highways. Seasonal effects are significant with winters generally less dynamic than summers, therefore thermal effects cannot be neglected during the summer, especially under low wind conditions and wind perpendicular to the street (Zhang et al., 2004; Kim and Baik, 2001; Xie et al., 2007; Xie et al., 2006). Mainly due to the existence of the embankment, dilution ratios of I-405 are higher than that of I-710 for both seasons with similar total TKE values. The dilution ratios obtained from CTAG show the same trend as the measurement data while CFD and CALINE4 show little change between different seasons. RMS of CTAG is consistently smaller than those of CALINE4 and CFD, which shows a more precise prediction of dilution ratio for CO horizontal dispersion and seasonal variations. CTAG's capability in capturing the seasonal variations is particular useful in long-term human exposure assessment of near-road exposure.

2.5.4 Vertical gradients

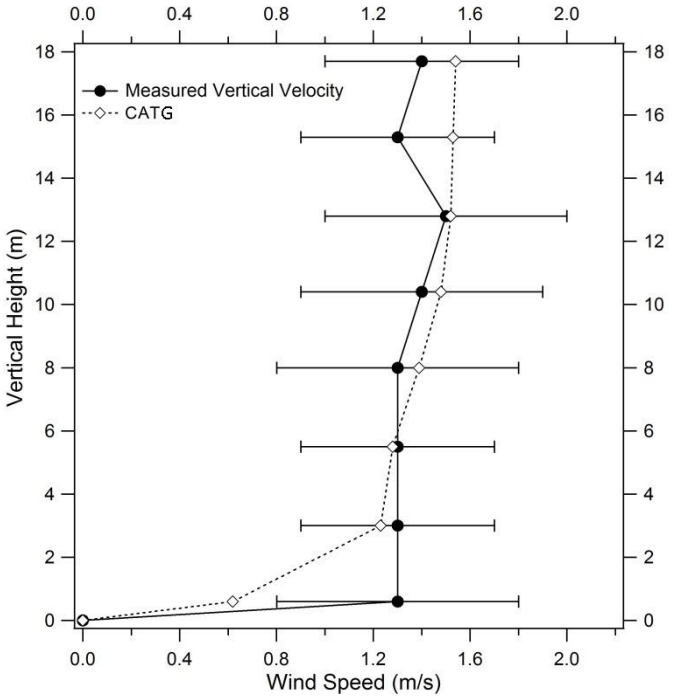

Figure 2.4. Comparison of wind velocity changing with vertical heights at 50m downwind between CTAG and field experiment for I-405 in summer. Error bars indicate one standard deviation of the measurement

We first compare the simulated wind velocity vertical profile with the field measurement. As illustrated in Figure 2.4, the measured wind velocities are approximately constant with vertical height and have relatively small and similar standard deviations (Zhu and Hinds, 2005). CTAG shows good consistence, except at height 0.6 m, where the simulated velocity is not within the standard deviation of the measured data. A possible reason is that since the sampling point is close to the surface, it is probably disturbed by the unconsidered structure on the ground.

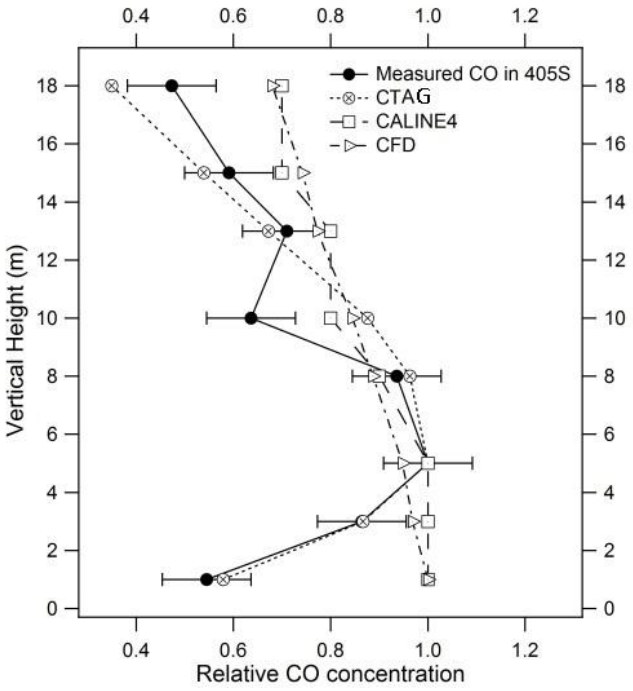

(a)

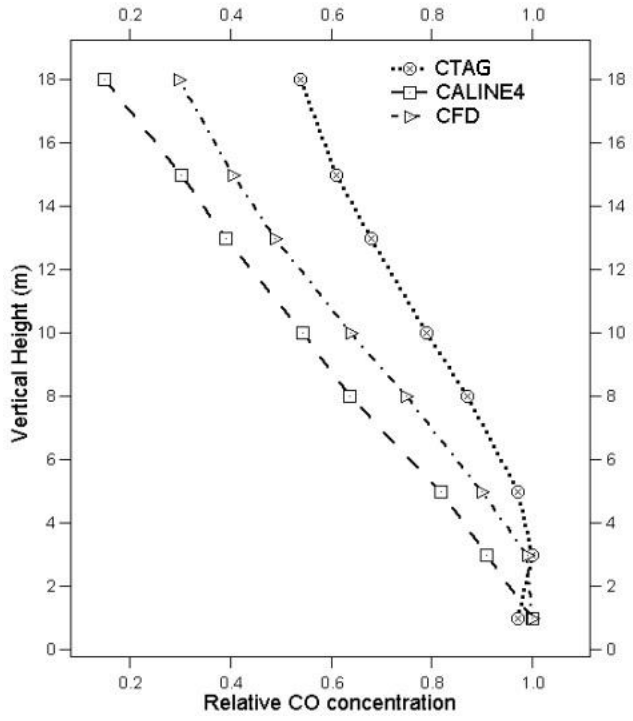

(b)

Figure 2.5. Comparison of vertical relative CO concentration (a) for I-405 in the summer and (b) for I-710 in the summer

Next, we compare the measured and simulated vertical profile of relative CO concentrations at eight sampling locations above the ground at 50 m downwind of I-405 horizontally in the summer, depicted in Figure 2.5(a). The vertical CO concentration is observed to reach a maximum at a height around 5 m above the ground, and decreases by 30% at 18 m above the ground. There is a dimple observed at 10 m, which is likely due to secondary mixing above the central line of emission (Zhu and Hinds, 2005). CTAG demonstrates great superiority in predicting CO vertical profile compared to CALINE4 and CFD. The RMS of CTAG shown in Table 2.3 is nearly half of those of CALINE4 and CFD. VIT and RIT play more significant roles in the vertical dispersion, where turbulence dominates the mixing process, than in the horizontal dispersion, where both turbulence and axial wind transport govern the mixing process. CTAG yields good predictions at almost all sampling points. Its maximum concentration is obtained at 6.4 m, about 1.9 m above the highway. The small rise of the plume from the highway is mainly due to the buoyancy of the exhaust induced by a higher temperature on surface of asphalted road. However, because of the strong mechanical mixing due to moving vehicles on road, the plume rise is small (Rao et al., 2002). Simulated CO concentration at the height of 0.6 m is in good agreement with the measurement data, though simulated wind velocity shows an error. This is mainly because vertical dispersion is mostly controlled by turbulence rather than wind velocity. The capability of CTAG to accurately predict the vertical profiles of air pollutants is important in studying human exposure to near-road air pollution for people living at different elevations.

Figure 2.5(b) compares the simulated CO vertical profiles at 50 m from I-710 in the summer by CTAG, CALINE4 and CFD models. CTAG predicts maximum concentration around 2 m above the highway (at the ground level) due to the thermal effects. In contrast, the maximum concentrations predicted by CALINE4 and CFD are both at the ground level due to lack of representation of the thermal effects.

2.5.5 On-road emission factors of carbon monoxide

As the capability of CTAG has been validated by the horizontal and vertical gradients of CO, we apply the inverse modeling method to derive the on-road CO emission factors using CTAG, following the methodology reported earlier (Kim and Patel, 2000). The derived CO emissions factors are, in g $mile^{-1}$ $vehicle^{-1}$, 6.1 for 405S, 7.2 for 405W, 7.0 for 710S, and 6.0 for 710W, which are similar to the values reported in the earlier study (Zhang et al., 2005).

2.6 Conclusion

We have demonstrated that the significant improvement in predicting the spatial gradients of air pollutants near roadways can be achieved by incorporating detailed treatment of VIT and RIT into dispersion modeling. RIT is determined by the roadway design characteristics such as roadway configurations (e.g., elevated or depressed), road surface properties (e.g., asphalt or concrete) and roadside structures (e.g., noise and vegetation barriers). VIT is governed by the traffic mix on the roadways, which is,

to a large extent, affected by roadway designs such as road width, slope and speed limits. Given the large effects of VIT and RIT on pollutant dispersion, we argue that roadway designs affect near-road air quality and that future roadway designs could serve as an effective strategy to mitigating near-road air pollution. Nevertheless, further understanding of the effects of the roadway designs on pollution dispersion is needed before making scientifically sound policies. We hope that our study can initiate future investigations into this subject.

CTAG is still more computationally expensive than Gaussian plume models such as CALINE4, but it is able to provide much more physical insights thanks to its rigorous treatment of turbulence mixing mechanisms on- and near-road, evinced by the excellent prediction of vertical gradients of air pollutants near roadways. Thus CTAG, or a combination of CTAG and CALINE4, can become a valuable tool in roadway design process and near-roadway air quality research. The caveat is that a CFD model without detailed treatment of VIT and RIT adds no more benefits than CALINE4 besides high computational cost.

CHAPTER 3

MODELING THE CHEMICAL EVOLUTION OF NITROGEN OXIDES NEAR ROADWAYS USING THE CTAG MODEL*

Abstract

The chemical evolution of nitrogen oxides (NO_X), nitrogen dioxide (NO_2) and nitrogen monoxide (NO) in the vicinity of roadways are numerically investigated using the CTAG model and a Gaussian-based model, CALINE4. CTAG couples a standard $k-\varepsilon$ turbulence model for turbulent mixing and the Finite-Rate model for chemical reactions. CALINE4 employs a discrete parcel method, assuming that chemical reactions are independent of the dilution process. The modeling results are compared to the field measurement data collected near two roadways in Austin, Texas, State Highway 71 (SH-71) and Farm to Market Road 973 (FM-973), under parallel and perpendicular wind conditions during the summer of 2007. In addition to ozone (O_3), other oxidants and reactive species including hydroperoxy radical (HO_2), organic peroxy radical (RO_2), formaldehyde (HCHO) and acetaldehyde (CH_3CHO) are considered in the transformation from NO to NO_2. CTAG is shown to be capable of predicting both NOx and NO_2 profiles downwind. CALINE4 is able to capture the NOx profiles, but underpredicts NO_2 concentrations under high wind velocity. Our study suggests that the initial NO_2/NO_X ratios have to be carefully selected based on

*Wang, Y., McDonald-Buller, E., Denbleyker, A., Allen, D., Zhang, K. M. Modeling chemical transformation of nitrogen oxides near roadways. Atmospheric Environment. 2011, 45(1): 43-52.

traffic conditions in order to assess NO_2 concentrations near roadways. The commonly assumed NO_2/NO_X ratio by volume of 5% may not be suitable for most roadways, especially those with a high fraction of heavy-duty truck traffic. In addition, high O_3 concentrations and high traffic volumes would lead to the peak NO_2 concentration occurring near roadways with elevated concentrations persistent over a long distance downwind.

3.1 Introduction

It is estimated that 30–45% of people in large North American cities live within the areas most highly affected by traffic emissions (Health Effects Institute, 2010). In the U.S., transportation accounts for approximately 60% of nitrogen oxides (NO_X) emissions, and near road environments have been found to significantly contribute to one-hour peak nitrogen dioxide (NO_2) exposures (USEPA, 2010). High concentrations or continued exposure to low levels of NO_2 have been associated with the development and exacerbation of respiratory and cardiovascular diseases (Horvath, 1980; OSHA, 2000). The U.S. Environmental Protection Agency (USEPA) recently revised the health-based National Ambient Air Quality Standards (NAAQS) for NO_2. The new 1-hour NO_2 standard is 100 parts per billion (ppb), which is determined as the 3-year average of the 98th percentile of the annual distribution of daily maximum 1-hour average concentrations (USEPA, 2010). USEPA is retaining the annual average NO_2 standard of 53 ppb. In order to determine compliance with the new standard, USEPA has established new monitoring requirements to include monitors at

locations where maximum NO_2 concentrations are expected to occur, such as within 50 meters of major roadways (USEPA, 2010).

There have been a number of studies investigating the chemical transformation of nitrogen oxides in power plant plumes (Builtjes and Talmon, 1987; Karamchandani et al., 1998), and the transformation of NOx near roadways has been the subject of increased attention in recent years (Carslaw, 2005; Alvarez et al., 2008; Clements et al., 2009). This chapter examines the chemical evolution of nitrogen oxides near roadways as represented by the gradients of NO_X and NO_2 concentrations along the plume dispersion trajectory. The two models, CTAG and CALINE4, simulate the chemical evolution of nitrogen oxides near two roadways under both perpendicular and parallel wind cases, and the modeling results are compared with the field measurement data collected during in Central Texas during the summer of 2007 (Clements et al., 2009; Zhu et al., 2009). Important parameters such as initial NO_2/NO_X ratio, ozone (O_3) concentrations, hydroperoxy radical (HO_2) and organic peroxy radical (RO_2) and photolysis rates are studied to explore the gradients of NO_2 and their human exposure implications under different conditions.

3.2 Field measurements

The experimental data utilized in this chapter were collected near two roadways during the Texas Roadway Study in the summer of 2007 (DenBleyker et al., 2008; Clements et al., 2009; Zhu et al. 2009). The first roadway was State Highway 71 (SH-71), an arterial highway dominated by passenger vehicles. The second roadway was

Farm to Market Road 973 (FM-973), a surface roadway dominated by truck traffic. No other significant anthropogenic emission sources were observed near the studied roadways. The gradients of nitrogen oxides were characterized by a mobile monitoring platform with increased distances from roadways as described by Clements et al. (2009). Stationary monitoring sites were established for time-integrated measurements of fine particulate matter mass and other gas-phase carbonyl species, such as formaldehyde (HCHO) and acetaldehyde (CH_3CHO). Four sets of measurements were conducted under different meteorological and road conditions: SH-71 with near parallel winds (designated as SH-71 Parallel), FM-973 with near parallel winds (FM-973 Parallel), FM-973 with two perpendicular wind cases (FM-973 Perpend1 and FM-973 Perpend2). Meteorological conditions, road characteristics, and pollutant concentrations are summarized in Table 3.1.

For FM-973, wind data was collected at the sampling site, while wind data for SH-71 and ozone concentrations for both roadways were retrieved from the nearest Texas Commission on Environmental Quality (TCEQ) continuous ambient monitoring station (CAMS #5003) at Austin Bergstrom airport, one mile from the studied roadways (http://www.tceq.state.tx.us/nav/data). Surface roughness was estimated based on the land surrounding SH-71 and FM-973 at the sampling site, which was open grassland, with a few trees surrounding sparse residences. Global radiation data were taken from the Solar Energy Laboratory at The University of Texas at Austin (http://www.me.utexas.edu/~solarlab/), from which photolysis rates were calculated as described in Section 3.3.1.2. Upwind NOx, NO_2, O_3, HCHO and CH_3CHO concentrations were obtained from field measurement. In Kenty et al. (2007), the

effects of HO_2 and RO_2 as oxidizing agents for NO were discussed but were not included in their simulation. In this chapter, the effect of HO_2 and RO_2 were investigated in the near roadway modeling simulations. Since direct HO_2 and RO_2 measurements in Austin area were not available, we approximated their concentrations based on the measurement in Houston in the summer of 2006 (Mao et al., 2009).

Even though the NO_2 concentrations were relatively low (<10 ppb) due to the low traffic volumes in the studied roadways (<2000 vehicles per hour) during the Texas Roadway Study, it provides a unique dataset in examining the capability of near-road modeling tools in characterizing the chemical evolution of NOx by measuring the NO and NOx concentrations along the wind trajectories.

3.3 Numerical models

3.3.1 Turbulent reacting flow model, CTAG

The concentrations of NO_2 near roadways are governed by the coupling of dilution, which acts to reduce NO_2 concentrations as exhaust is being dispersed from roadways, and chemical reactions of nitrogen oxides and ozone, which typically results in a net generation of NO_2. Therefore, we expand the capability of the CTAG model to incorporate the coupling of dilution and chemical reactions.

3.3.1.1 Turbulent dispersion near roadways

Pollutant dispersion near roadways usually experiences two distinct stages – ‘tailpipe-to-road’ and ‘road-to-ambient’ (Zhang and Wexler, 2004). For both stages,

dilution is the dominant mechanism and is caused by on-road and near-road turbulent mixing. As described in Chapter 2 (Wang and Zhang, 2009), turbulent mixing can be classified into three categories according to their origins: First, vehicle-induced turbulence (VIT), due to the movement of vehicles and buoyancy of hot exhaust; second, road-induced turbulence (RIT), caused by the existence of embankment, roadside barriers (such as vegetations and sound walls), and thermal effects due to solar radiation on road surface; and finally, atmospheric boundary layer turbulence (ABLT).

CTAG simulates different turbulent mixing mechanisms using a selected turbulent model. Our study in Chapter 2 shows that a standard $k-\varepsilon$ turbulence model is capable of capturing VIT and RIT for near-road conditions.

3.3.1.2 Chemical reactions

The reactive pollutants studied here are NO and NO_2 in the presence of background O_3, HO_2 and RO_2 and sunlight. The main chemical reactions considered are (Sadanaga et al., 2003; Baik et al., 2007):

$$NO + O_3 \rightarrow NO_2 + O_2 \tag{3.1}$$

$$NO_2 + h\nu \rightarrow NO + O \tag{3.2}$$

$$O + O_2 + M \rightarrow O_3 + M \tag{3.3}$$

The reaction rate constant $k_1 = 44.05\times10^{-3}\exp(-1370/T)\ ppb^{-1}s^{-1}$ is temperature-dependent, where T is in Kelvin (K). The photolysis rate, J_{NO2}, depended on the solar

irradiance. Here we adopt an expression in the form of a second-order polynomial function derived from recent field observations: $J_{NO_2} = (1+\alpha) \times \left(B_1 \times G + B_2 \times G^2 \right) s^{-1}$ (Trebs et al., 2009), where α is defined as the site-dependent UV-A surface albedo and the polynomial coefficients; and B_1 and B_2 can be used to estimate ground-level J_{NO_2} directly from G, independent of solar zenith angle under all atmospheric conditions. Calculated photolysis rates for each set are shown in Table 3.1. Reaction 3.3 is assumed to proceed instantaneously.

Table 3.1 Meteorological parameters and road conditions

	SH-71	FM-973		
	Parallel	Perpend1	Perpend2	Parallel
Measurement period	16:35-18:40, Jun 11	14:40-16:10, Jul 12	13:20-17:15, Jul 13	10:45-13:10, Jul 13
Temperature (℃)	31.8	32.6	25.5	29.4
Wind velocity (m s^{-1})	3.82	4.22	2.17	2.71
Range of wind angle (°)	7.3	9.8	19.8	14.2
Surface roughness (m)	0.1	0.1	0.1	0.1
Global radiation (W m^{-2})	243	671	550	938
Photolysis rate (s^{-1})	0.00394	0.00845	0.00732	0.01020
Stability class	Neutral	Slightly Unstable	Slightly Unstable	Unstable
Number of track lines	4	2	2	2
Road width (m)	16.0	8.5	8.5	8.5
Road elevation (m)	0	0	0	0
Pollutant sampling height (m)	3.0	3.0	3.0	3.0
Traffic volume (vehicle h^{-1})	1914	1194	1038	774
Heavy-duty truck percentage	5%	37%	34%	28%
Vehicle speed (m s^{-1})	24.2	15.3	15.3	15.3
Nitrogen oxides (NO_X) [a,c]	0.75	2.57	4.05	5.62
Nitrogen dioxide (NO_2) [a,c]	0.53	2.16	2.78	3.59
Ozone (O_3) [a,c]	27.0	25.5	25.8	22.5
Hydroperoxy radical (HO_2) [b,c]	9	20	13	26
Organic peroxy radical (RO_2) [b,c]	135	300	195	390
Formaldehyde (HCHO) [b,c]	92	156	148	173
Acetaldehyde (CH_3CHO) [b,c]	364	171	162	190

[a] Unit is ppb, [b] Unit is ppt. [c] Background concentration.

HO_2 and RO_2 were also responsible for the conversion between NO and NO_2 (Carpenter et al., 1998; Mao et al., 2009):

$$HO_2 + NO \rightarrow OH + NO_2 \tag{3.4}$$

$$RO_2 + NO \rightarrow RO + NO_2,\ k_{4,5} = 51.39\times10^{-3}\exp(250/T)\ \ ppb^{-1}s^{-1} \tag{3.5}$$

Photodissociation of HCHO and higher aldehydes, such as CH_3CHO, which can be photolyzed to HO_2 and RO_2, are important sources of HO_2 in the atmosphere (Sadanaga et al., 2003):

$$HCHO + h\upsilon(+O_2) \rightarrow HO_2 + HCO\ ,\ k_6 = 2.17\times10^{-5}\ s^{-1} \tag{3.6}$$

$$CH_3CHO + h\upsilon\left(+O_2\right) \rightarrow CH_3O_2 + HCO\ ,\ k_7 = 6.35\times10^{-6}\ s^{-1} \tag{3.7}$$

$$HCO + O_2 \rightarrow HO_2 + CO,\ k_8 = 76.35\times10^{-3}\ \ ppb^{-1}s^{-1} \tag{3.8}$$

However, the photolysis of HCHO is typically more important than that of other higher aldehydes because the absorption and photodissociation leading to radical production of HCHO extends to longer wavelengths than that of higher aldehydes.

In our turbulent reacting flow model, two sets of reactions are simulated. First, only Reaction 3.1 – Reaction 3.3 are considered. The resultant model configuration is named as CTAG with Three Reactions (CTAG w/ 3 RXN). Second, all eight reactions, Reaction 3.1 – Reaction 3.8, are considered. The configuration is named as CTAG with Eight Reactions (CTAG w/ 8 RXN). The comparison among the two configurations is used to reveal the importance of reactions Reaction 3.1 – Reaction 3.3 for the production of NO_2 and roles of HO_2 and RO_2 in the chemical evolution process near roadways.

CTAG couples the Finite-Rate Model and the $k-\varepsilon$ turbulence model to simulate the transformation and transportation of NO_2. In the Finite-Rate Model (Peters, 2000), detailed kinetics of Reaction 3.1 – Reaction 3.8 were simulated, where reaction rate constants were determined by Arrhenius expressions and in this section the effect of turbulent fluctuations is ignored.

3.3.1.3 Modeling domain

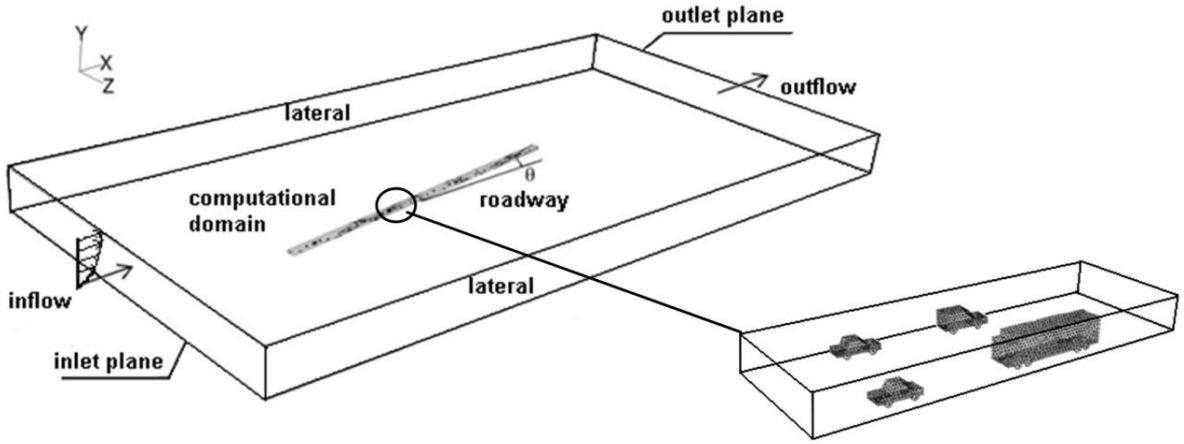

Figure 3.1. Sketch of the CTAG computational domain

Figure 3.1 shows the schematic diagram of the computational domain and boundary conditions for CTAG, which can be modified according to different road conditions, i.e. width and elevation of roads, traffic volume. The roadway axis can be rotated to make the angle θ to be the angle between the roadway axis and the direction of the prevailing wind, i.e., x axis. The y axis is referred to the height of the domain, while the z axis is the width of it. The length of roadway can be adjusted to make the simulation results insensitive of the chosen value, especially for parallel

wind cases. For perpendicular cases, the spatial domain has a size of 600 by 200 m in the horizontal and 150 m in the vertical direction and is divided into 2.5 million unstructured cells, while for parallel cases, the domain has a size of 3000-250-1800 m (x-y-z) and about 6.1 million unstructured cells. Mesh independence study (1.5 million and 3.5 million for vertical direction, 4.6 million and 7.6 million for parallel cases) has been conducted to make sure that the grid resolution to be fine enough for the accuracy of the simulation result (difference within 5% for the simulation results of the dispersion of NOx). Sensitivity study has been conducted to guarantee that the simulation results are independent of the height of the domain. At the inlet boundary, a fully developed vertical profile of inlet wind flow is imposed in the + y-direction, as shown in Chapter 2. Symmetric boundary conditions are set to lateral and the top planes of the domain, representing a zero flux of all quantities. All the surfaces of ground, road and vehicles are set as "wall", for which a no-slip condition is satisfied. At the exit plane an outflow condition is imposed, meaning that a zero normal first derivative of all quantities is fulfilled.

A uniformly mixed zone above the road surface, formed through the mergence of the turbulence zones produced by the vehicles in a stream of moving traffic, is created to obtain TKE and used as the effective emission source. The height of the mixing zone depends on the heavy-duty truck percentage. We set the height for light-duty-vehicles-dominated roadways to be 2.5 m (Held et al., 2003), and the height for heavy-duty-vehicles-dominated roadways to be 5.0 m. The height of the mixing zone for a specific highway is taken as the weighted average of those two heights depending on the heavy-duty diesel traffic. Since most of the on-road vehicles were cars and vans

for SH-71, the height of its mixing zone is set to be 2.5 m. For FM-973, due to its larger volume of truck traffic, the height is set to be 3.5 m.

The methodology for estimating VIT is explained in Chapter 2. We model the vehicles as real-shaped to keep the conditions similar to the streamlined shape of real vehicles. The sketch of detailed vehicle mesh can be found in Figure 3.1, though the vehicle number and percentage for each type of vehicle vary with different roadways. The surfaces of the vehicles are set as moving walls and their velocities are specified according to the field measurements show in Table 3.1 for each roadway. Therefore the air connected to these surfaces has the same velocity and decreases when moving away from them due to non-slip condition and therefore TKE can be produced due to the velocity gradient. We also select appropriate values of the surface roughness length for the sampling area (Seinfield and Pandis, 2006), shown in Table 3.1. To simulate the buoyancy, the temperature difference between air and roadway surface is estimated to be 15 ℃ for the two roadways according to the weather status during the measurement period.

3.3.2 Gaussian plume model

CALINE4, a Gaussian plume-based line source model, is widely used in the prediction of carbon monoxide dispersion for roadways (Benson 1992). The NO_2 option for CALINE4 is available using its executable from a command line (http://www.dot.ca.gov/hq/env/air/pages/calinesw.htm). CALINE4 considers reactions Reaction 3.1 – Reaction 3.3, and the same reaction rate constants are set for both CALINE4 and CTAG. CALINE4 uses a Discrete Parcel Method, which assumes that

emissions and ambient reactive species are fully mixed in the roadway mixing zone initially, and that the dispersion of this initial mix is characterized as a scattering of discrete parcels, with reactions proceeding as isolated processes within each parcel (Benson 1992). Therefore the NO_2 concentration at a downwind receptor is solely governed by the initial concentrations and time of travel from element to the receptor. In other words, the reactions within each parcel are independent of the dispersion process (Benson 1992).

3.3.3 Model initialization: Curbside NOx concentrations and NO_2/NOx ratios

The initial NO_X emission for roadways is commonly assumed to consist of 95% NO and 5% NO_2 by volume (Berkowicz, 2000; Kenty et al., 2007). However, the increasing NO_2/NOx ratios monitored near roadways in the past few years indicate that the proportion of NO_2 emitted by traffic has changed. A study in London showed that the roadside NO_2/NO_X ratio increased markedly from a mean of about 5-6% in 1997 to about 17% in 2003 (Carslaw, 2005). This rise in the ratio of NO_2 to NO_X parallels the implementation of oxidation catalytic converters or diesel particular filters (DPF) in diesel vehicles (Carslaw and Beevers, 2005; Alvarez et al., 2008). Diesel exhaust is now the largest anthropogenic source of NO_X, and the NO_2/NO_X ratio is higher in diesel engines than in gasoline engines. Aftertreatment devices such as the oxidation catalytic converters oxidize carbon monoxide and hydrocarbons originating from incomplete combustion in the engine, but also enhance the conversion from NO to NO_2 in certain temperature conditions. Herner et al. (2009)

reported a wide range of NO_2/NOx ratios depending on the combinations of aftertreatment devices (indicating different catalytic loading) and driving cycles (indicating different operating temperatures for the devices). Highest emissions of NO_X were recorded for diesel vehicles equipped with diesel particulate filters with mass ratios of NO_2 within NO_X of up to 70% (Alvarez et al., 2008).

Table 3.2 Fitting of NOx and NO concentrations with y=a+b*exp(-c*x)

	A	b	C	R^2	Curbside NOx[a]	Initial NO_2/NOx
FM-973 Perpend1 NOx	6.565	20.155	0.01920	0.966	24.3	31.0%
FM-973 Perpend1 NO	1.413	16.632	0.02108	0.998	16.8	
FM-973 Perpend2 NOx	7.936	34.613	0.03988	0.997	38.4	28.8%
FM-973 Perpend2 NO	4.039	29.040	0.04529	0.997	27.3	
FM-973 Parallel NOx	0	27.063	0.00328	0.969	25.1	25.6%
FM-973 Parallel NO	0	19.391	0.00463	0.989	18.7	
SH-71 Parallel NOx	0.910	15.867	0.00842	0.981	15.7	19.4%
SH-71 Parallel NO	1.103	14.777	0.00878	0.996	12.7	

[a] Unit is ppb.

Therefore, in this chapter the initial NO_2/NO_X ratios are obtained from the field experiment data. We fit the measured NO_X and NO concentrations at multiple downwind distances with exponential decay curves, of the form $y = a + b\exp(-cx)$. The "x" is referred to the downwind distance, while "y" is the concentration of pollutants (ppb). The values for a, b, and c for each case are listed in Table 3.2. The error bars take into account the discrepancies between the different sets of measurements and the detection limit of the NOx measuring instrument (0.4 ppb) (Zhang et al., 2005; Clements et al., 2009). Instead of showing the pooled concentration profiles of NOx and NO for all the studied roadways together (Clements et al. 2009), we analyze each case listed in Table 3.1 separately. The exponential decay curves are then used to estimate the NOx concentrations and the NO_2/NOx

ratios at the edge of the roadway, referred to as "curbside". Since the on-road concentrations are typically well-mixed due to vehicle-induced turbulence, we use the curbside concentrations as the initial conditions for both CTAG and CALINE4 simulations. The R^2 values for each case are shown in Table 3.2. The initial NO_2/NO_X ratio for FM-973 Perpend1, FM-973 Perpend2, FM-973 Parallel and SH-71 Parallel are 31.0%, 25.6%, 28.8% and 19.4% by volume, respectively. The difference between each case is likely due to the different heavy-duty truck percentages (Carslaw, 2005). Among the three cases for FM-973, the Perpend1 case has the highest heavy-duty truck percentage, which explains its highest initial NO_2/NO_X ratio. Estimated FM-973 curbside NO_X concentrations are generally higher than SH-71, since SH-71 has a lower volume of heavy-duty truck but higher total traffic volume. This is consistent with heavy-duty trucks which have much higher NO_X emission (Alvarez et al., 2008).

3.4 Results and discussion

3.4.1 Turbulent Kinetic Energy (TKE) in the vicinity of roadways

Table 3.3 Summary of TKE in the mixing zones for the different roadways

	SH-71		FM-973					
	Parallel	%	Perpend1	%	Perpend2	%	Parallel	%
VIT [a]	0.08	20.5	0.06	15.9	0.05	35.7	0.04	23.5
RIT [a]	0.02	5.1	0.01	2.6	0.01	7.1	0.01	5.8
ABLT [a]	0.29	74.4	0.31	81.5	0.08	57.2	0.12	70.7
Total TKE [a]	0.39	100.0	0.38	100.0	0.14	100.0	0.17	100.0

[a] Unit is $m^2 s^{-2}$.

Induced TKE within the mixing zones is summarized in Table 3.3. It is clear that TKE changes under different traffic and meteorological conditions. All VITs are less than 0.1 $m^2 s^{-2}$ and account for 35.7% of total TKE at most. The relative small contributions of VIT to the total TKE are due to the low traffic volumes for SH-71 and FM-973. The traffic volumes for SH-71 and FM-973 are 1914 vehicle h^{-1} and 1038 vehicle h^{-1}, respectively, compared to 14160 vehicle h^{-1} for I-710 in Los Angeles in Chapter 2, where the VIT is shown to account for 86.2% of the total TKE. RIT is also small because 1) the road widths are narrow so that little solar radiation is received on the road surfaces, and 2) there are no embankments, tall trees or sound walls existing near SH-71 or FM-973. Therefore, the atmospheric boundary layer turbulence (ABLT) is the dominant mechanism for turbulent dispersion near the two roadways.

3.4.2 Horizontal gradients of NOx

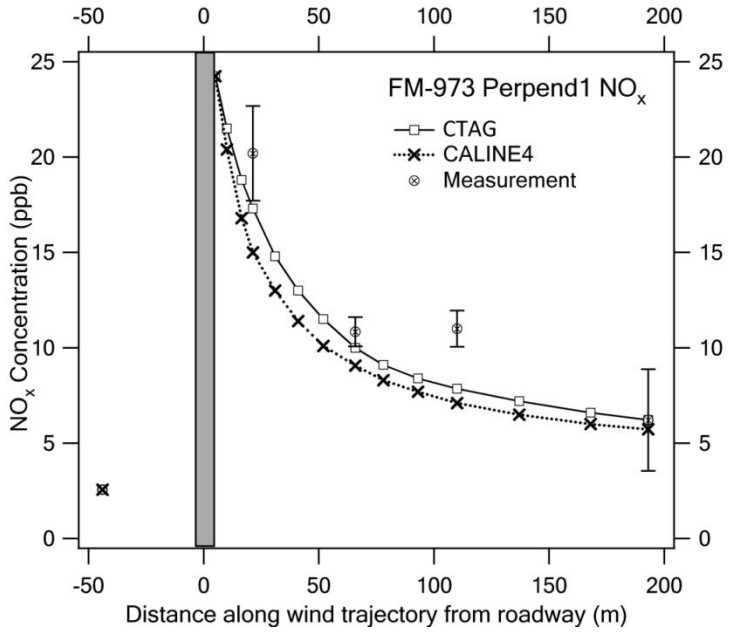

(a)

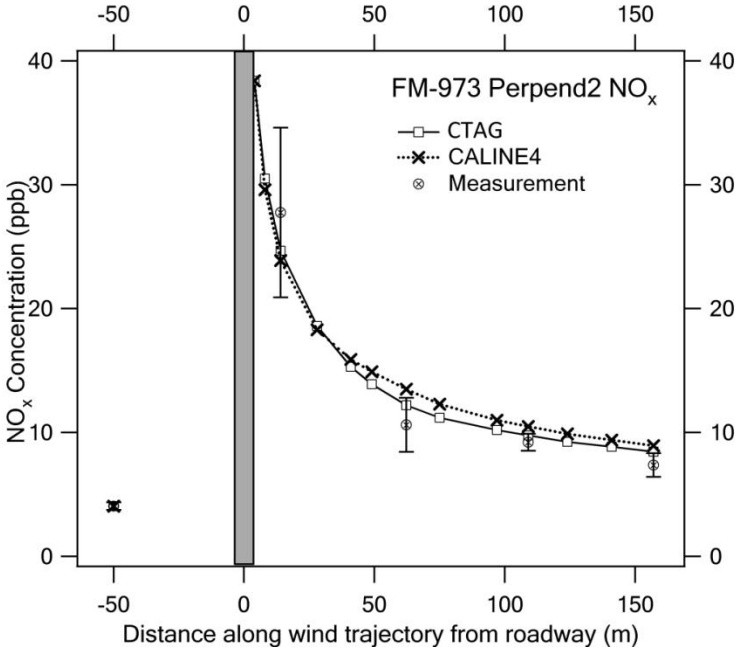

(b)

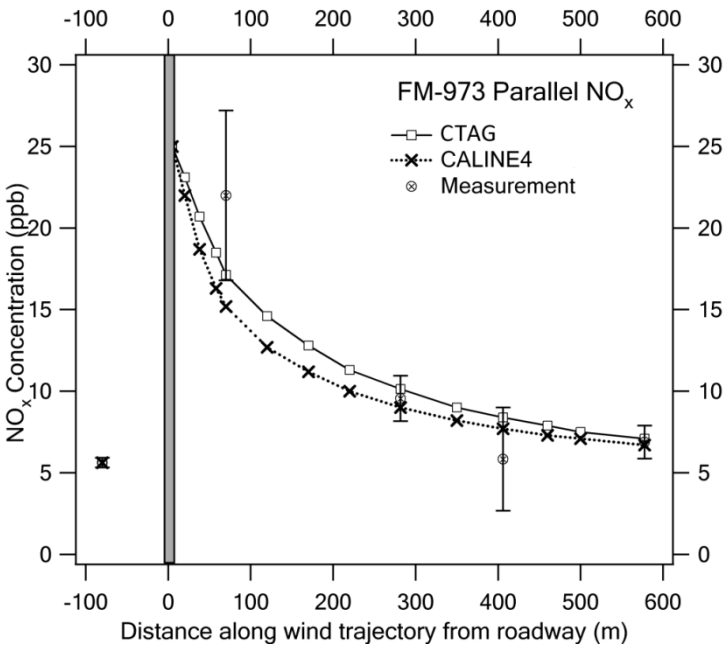

(c)

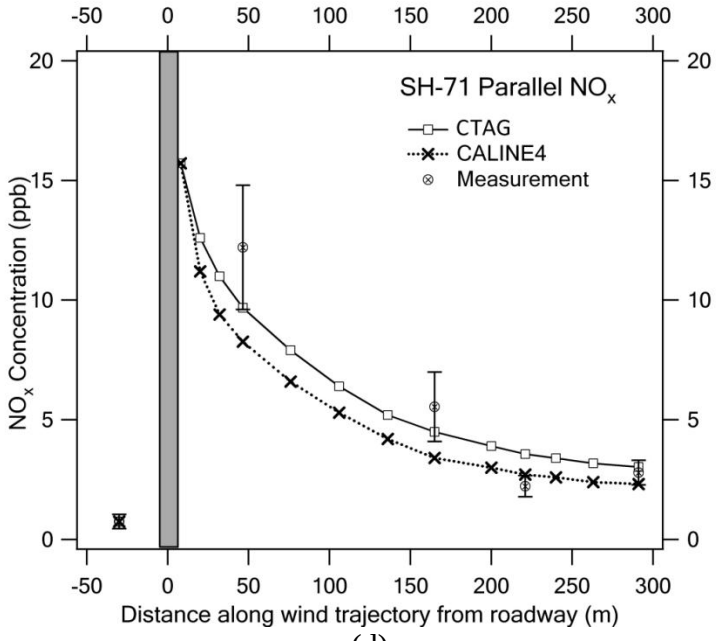

(d)

Figure 3.2. Comparison of NO_X concentration profiles between models and field experiment for (a) FM-973 Perpend1, (b) FM-973 Perpend2, (c) FM-973 Parallel and (d) SH-71 Parallel. X-axis is the true distance as an air parcel travels from the roadway to the mobile sampling locations. Positive x value meant downwind and negative x value means upwind

Figure 3.2 illustrates that NO_X concentrations decay exponentially with increasing distance from the roadway, and that at further downwind NOx concentrations return to their background levels due to the dilution process. Compared to FM-973 Perpend1, FM-973 Perpend2 has larger NOx concentrations which are mainly due to lower wind velocity.

It can be seen from Figure 3.2 that both CTAG and CALINE4 agree reasonably well with the measurement, which provide a reliable basis for NO_2 comparisons in the next step. Since VIT and RIT don't dominate TKE for both roadways, CTAG only shows a moderate advantage over CALINE4, based on the root mean square (RMS) between modeled and measured concentrations shown in Table 3.4. But as shown in Chapter 2, CFD considerably improved the modeling predictions for cases involving high traffic volumes and complex roadway configuration, where the roles of VIT and RIT are significant.

Table 3.4 RMS of NOx and NO_2 concentrations for different cases

	CTAG w/ 3 RXN		CTAG w/ 8 RXN		CALINE4	
	NOx	NO_2	NOx	NO_2	NOx	NO_2
FM-973 Perpend1	0.587	0.667	--	0.648	0.873	0.953
FM-973 Perpend2	0.438	0.261	--	0. 333	0. 678	0. 239
FM-973 Parallel	0.749	0.502	--	0. 519	0. 826	0. 516
SH-71 Parallel	0.621	0.319	--	0.312	0.754	0.502
FM-973 Perpend1, 5% NO_2	--	1.155	--	1.125	--	1.365
SH-71 Parallel, 5% NO_2	--	0.462	--	0.439	--	0.649

3.4.3 Horizontal gradients of NO_2

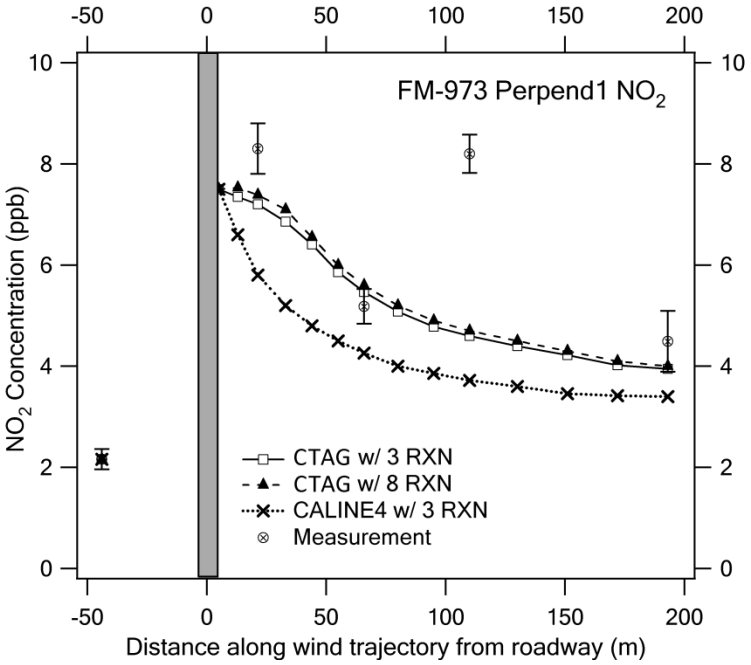

(a)

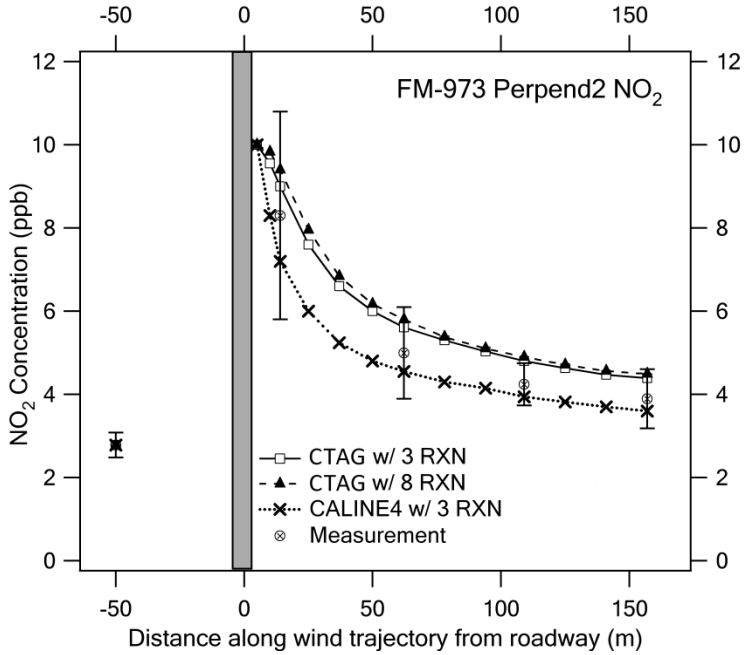

(b)

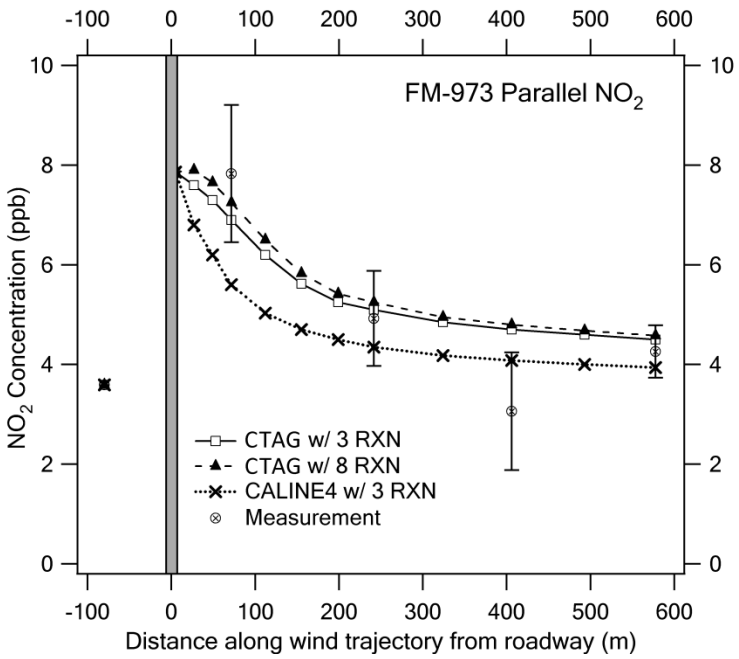

(c)

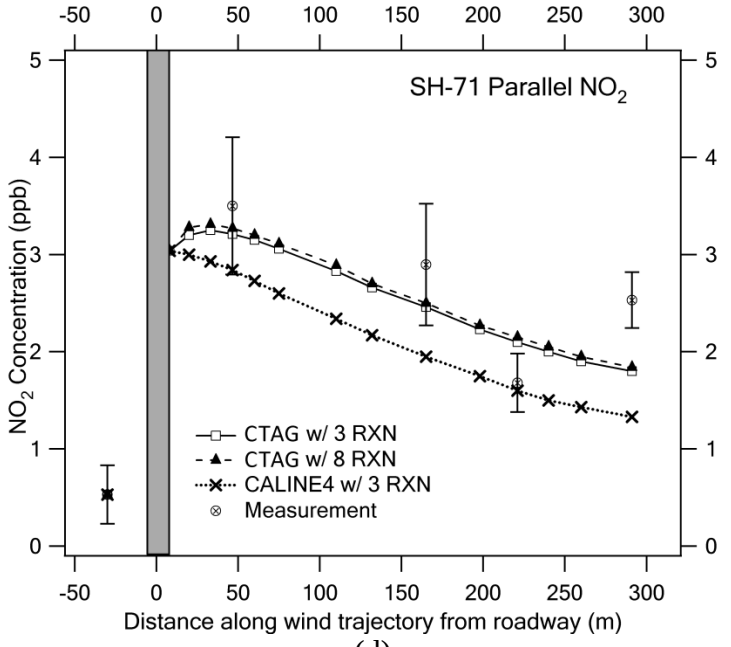

(d)

Figure 3.3. Comparison of NO_2 concentration profiles between models and field experiment for (a) FM-973 Perpend1, (b) FM-973 Perpend2, (c) FM-973 Parallel and (d) SH-71 Parallel

Figure 3.3 depicts the horizontal gradients of NO_2 for the two roadways. As described earlier, the dilution process decreases the concentration of NO_2, while the chemical reactions tend to favor NO_2 production. As a result, the decay rate of NO_2 is far less than that of NO_X concentrations in the near-road environments. At the same time, the NO_2/NOx ratio increases with increasing distance from the roadway until it reaches the background level. As one example, the dataset FM-973 Perpend1 has an extrapolated concentration of NO_X at the curbside comprised of 31% NO_2, while at 191 m downwind, NO_2 makes up 66% of NO_X and the background NOx contains 81% NO_2.

It also can be seen from Figure 3.3 that CALINE4 tends to underpredict NO_2 concentration near the roadway. In particular, under high wind velocity, e.g. FM-973 Perpend1 and SH-71 Parallel, NO_2 concentrations are underestimated during the entire dispersion process. With rigorous treatment of turbulent mixing and chemical reactions, CTAG shows better performances than CALINE4 in predicting NO_2 gradients for all the investigated cases, as shown by the RMS values listed in Table 3.4. When HO_2 and RO_2 are considered, based on their different concentrations, the simulated NO_2 concentrations of CTAG w/ 8 RXN are 2% to 7% higher than those of CTAG w/ 3 RXN. For SH71 Parallel, with the lowest HO_2 and RO_2 concentration among the four cases, NO_2 concentration of CTAG w/ 8 RXN is only 2% higher than CTAG w/ 3 RXN, which suggests negligible effect of HO_2 and RO_2 on the transformation of NO to NO_2 due to their limited concentrations. Under this circumstance, the influence of HO_2 and RO_2 on the concentration of NO_2 can be ignored, while for other situations, such as near a polluted area, where HO_2 and RO_2

have higher concentrations, their effect should not be omitted, since they can become the additional NO_2 source to surpass the controlled NO_2 concentration.

A major difference between FM-973 and SH-71 is that the NO_2 concentration for FM-973 decays immediately from the roadway, while for SH-71, CTAG predicts that the NO_2 concentrations first increases and then starts to decay, resulting in a peak NO_2 concentration at 33 m along the wind trajectory. The reason for this is that FM-973 has a higher heavy-duty truck fraction, therefore the initial on-road NO_2/NO_X ratio is relatively large, while the SH-71 parallel case has the lowest initial NO_2/NO_X ratio among four cases, which is related to the low heavy-duty truck percentage on SH-71. Therefore the relatively abundant curbside NO concentration near SH-71 leads to a much higher NO-to-NO_2 conversion rate, overcoming the dilution rate and resulting in a higher NO_2 concentration further downwind from the curbside.

To further illustrate the dynamics between chemical reactions and dilution, based on the CTAG w/ 3 RXN results, we adopt the concept of photostationary state defect (%) defined here as (Carpenter et al., 1998; Baker et al., 2004):

$$d_{ps} = \left(\frac{k_1[O_3][NO]}{J_{NO_2}[NO_2]} - 1 \right) \times 100 \qquad (3.9)$$

d_{ps} is a measure of the departure degree from the photochemical steady-state condition for NO_2. Higher, positive d_p indicates a higher NO_2 production rate relative to NO_2 dissociation rate.

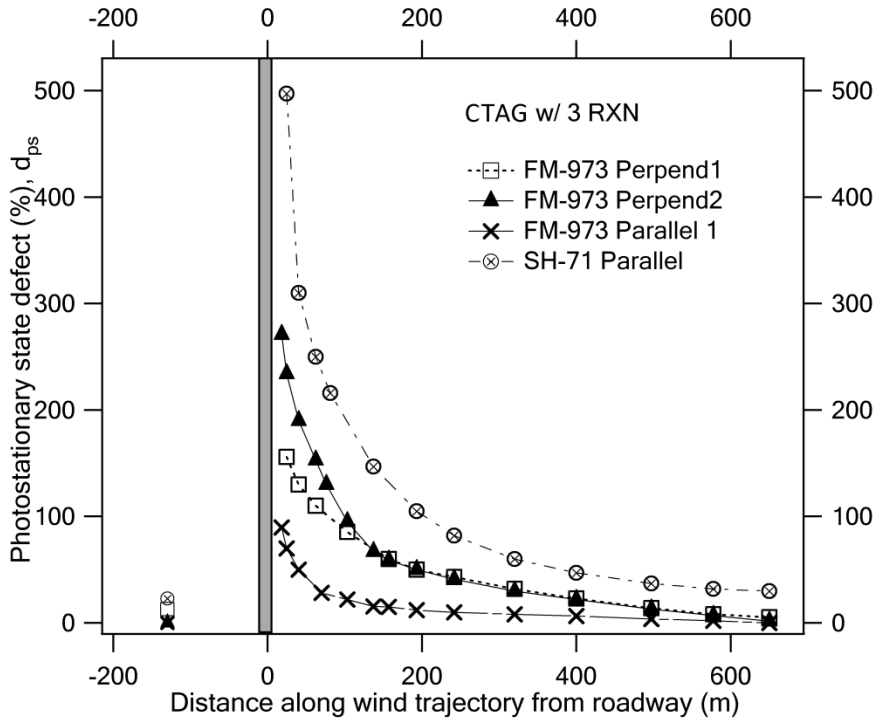

Figure 3.4. Profile of photostationary state defect for FM-973 and SH-71 under parallel and perpendicular wind conditions

d_{ps} is close to zero in the upwind flow shown in Figure 3.4, which suggests a nearly photochemical steady state for the background condition, but rises sharply after the flow moves cross the roadways. For the closest sampling points downwind of the roadway, the photostationary states defect are much larger than zero for all four cases, indicating that Reaction 3.1 is faster than Reaction 3.2 and that NO is converted to NO_2. Then the phototstationary state defect started to decay, and at 650 m downwind, all four cases are close to chemial equilibrium again, when d_{ps} is close to zero.

For SH-71, since the initial NO_2/NO_X ratio and photolysis rate are the lowest, and its ozone concentration is the highest among the four cases, its photostationary state defect, d_{ps} is the largest near the roadway, which explains why NO_2 first rises and then

starts to decay downwind of SH-71. Due to the similar NO_X composition and the photolysis rates for FM-973, d_{ps}'s are simialar among all three FM-973 cases and are smaller than that of SH-71.

3.4.4 Sensitivity Analysis

3.4.4.1 NO_2/NO_X ratio

As described in Section 3.3.3, we obtain the initial NO_2/NOx ratios from the measurement data. The ratios we derived are drastically different from the commonly assumed ratio, i.e., 5%. To test the validity of this assumption, both curbside NO_2/NOx ratio of FM-973 Perpend1 and SH-71 are set to be 5 %, while all other parameters for the simulation remain the same.

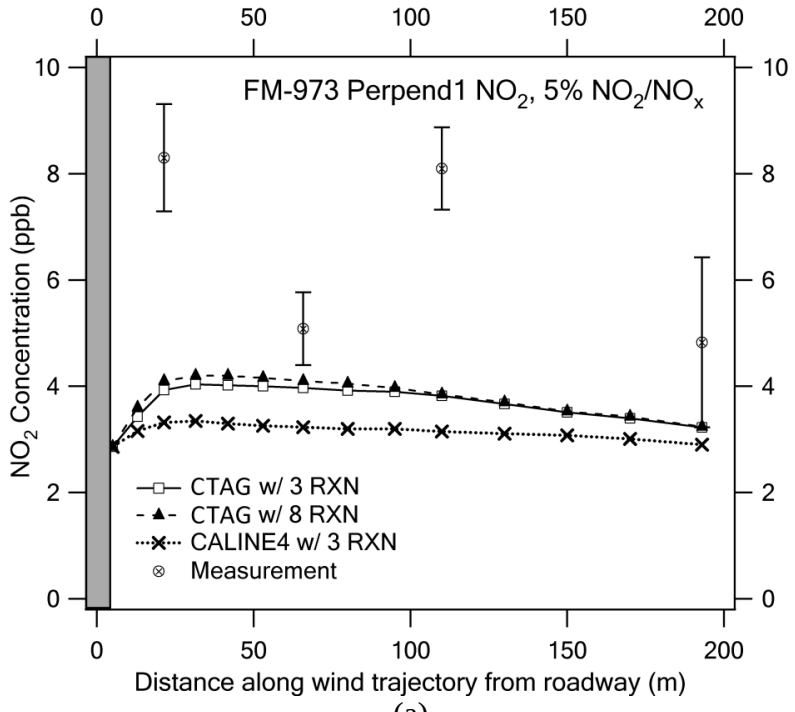

(a)

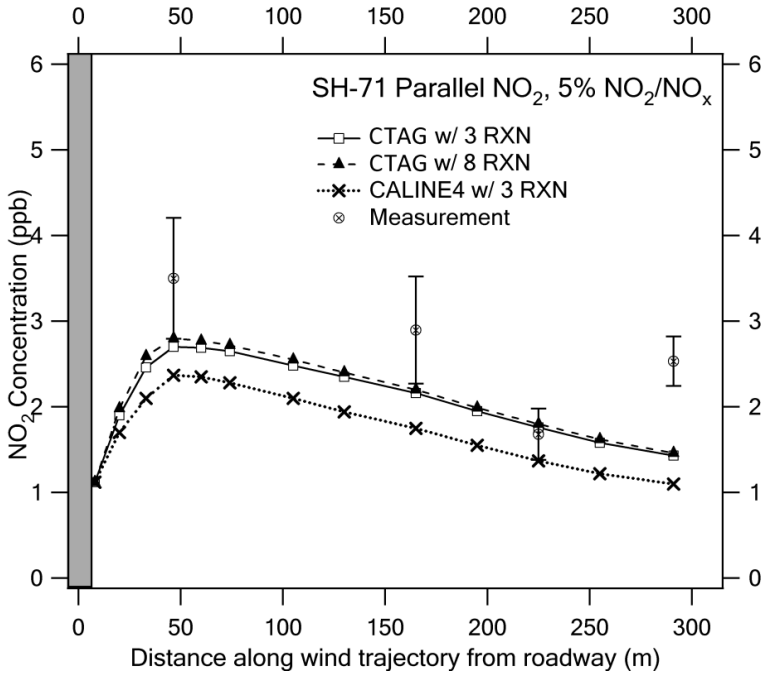

(b)

Figure 3.5. Comparison of NO_2 concentration profiles between models and field experiment for (a) FM-973 Perpend1 and (b) SH-71 Parallel when the NO_2/NO_X is set to be 5%

Figure 3.5 shows that using the 5% NO_2/NO_X ratio, all the models underpredict the downwind NO_2 concentrations for both FM-973 and SH-71. In particular, at the closest sampling point of FM-973, the result from CALINE4 is only around one third of the measured value and CTAG shows poor agreement as well. The RMS of the NO_2 profile for FM-973 Perpend1 with 5% NO_2/NO_X is almost twice as large as that of FM-973 Perpend1 with 31% NO_2/NO_X. Compared with FM-973, the model predictions for SH-71 are closer to observations, which are due to the low diesel fraction on SH-71. The heavy-duty truck percentage for FM-973 is around 34%, while SH-71 has only 5% heavy-duty truck traffic. Since the NO_2 fraction emitted from diesel trucks is substantially higher than that of gasoline cars, a lower heavy-duty

truck percentage means the assumed 5% NO_2/NO_X ratio is closer to actual conditions. Therefore, the NO_2/NO_X ratio is a dominant parameter that affects the accuracy of the NO_2 prediction. The commonly assumed 5% NO_2/NO_X ratio may not be suitable for most roadways, especially those with a high fraction of heavy-duty truck traffic.

3.4.4.2 Ozone concentration, photolysis rate and temperature

Table 3.5 Values of O_3 concentrations, temperature and photolysis rates for sensitivity analysis

Case ID	Date	O_3[a]	Temperature[b]	Photolysis rate[c]	Type	Notes
Case 1	09/21/07	93	32.2	0.00951	Urban	Highest eight-hour O_3 concentration in 2007
Case 2	10/04/07	75	29.7	0.00843	Urban	Eight-hour O_3 air quality standard in NAAQS
Case 3	07/24/07	47	30.1	0.00839	Rural	Highest O_3 concentration during field experiment
Case 4	06/13/07	26	32.6	0.00845	Rural	FM-973 Perpend1, used as a reference case
Case 5	06/13/07	13	20.8	0.0	Urban	Night-time
Case 6	06/13/07	6	19.6	0.0	Rural	Night-time
Case 7	06/13/07	0	32.6	0.0	Rural	Dilution process without chemical reaction

[a]Unit is ppb, [b]Unit is K, [c]Unit is s^{-1}.

Different combinations of ozone concentrations, photolysis rates, and temperatures, corresponding to different types of environments, are examined for the influence of these parameters on the chemical evolution of NO_2. Seven representative ozone concentrations and their corresponding temperatures in Austin area are selected from the TCEQ, shown in Table 3.5, our comparisons are based on FM-973 Perpend1 case, and other parameters remain the same for the comparisons:

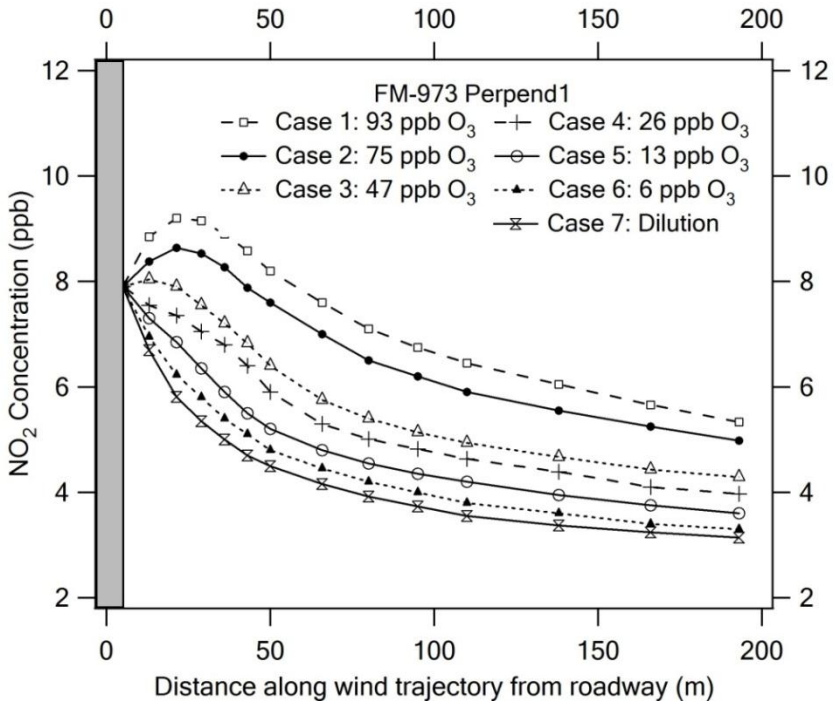

Figure 3.6. Comparison of NO_2 concentration profiles under different ozone concentrations and corresponding photolysis rate for FM-973 Perpend1

As shown in the Figure 3.6, under daytime, high O_3 concentrations (e.g. 75 ppb and 93 ppb), peak NO_2 concentrations tends to occur within 50 m downwind of the roadway due to the high initial NO-to-NO_2 conversion rates, which indicats the existence of high NO_2 exposure zones near roadways. In addition, under high O_3 conditions, elevated NO_2 concentrations persist much further downwind, implying a larger affected population in broader areas than under low O_3 conditions. Under nighttime conditions, since O_3 concentrations are low, especially for rural locations, the NO_2 profiles are mostly governed by dilution. It should be noted that the traffic volume is relatively low for all the cases we simulated. We expect much elevated near-road NO_2 concentrations with high traffic-volume and high ozone concentrations, typical for major metropolitan areas.

3.4.4.3 Height of the emission zone

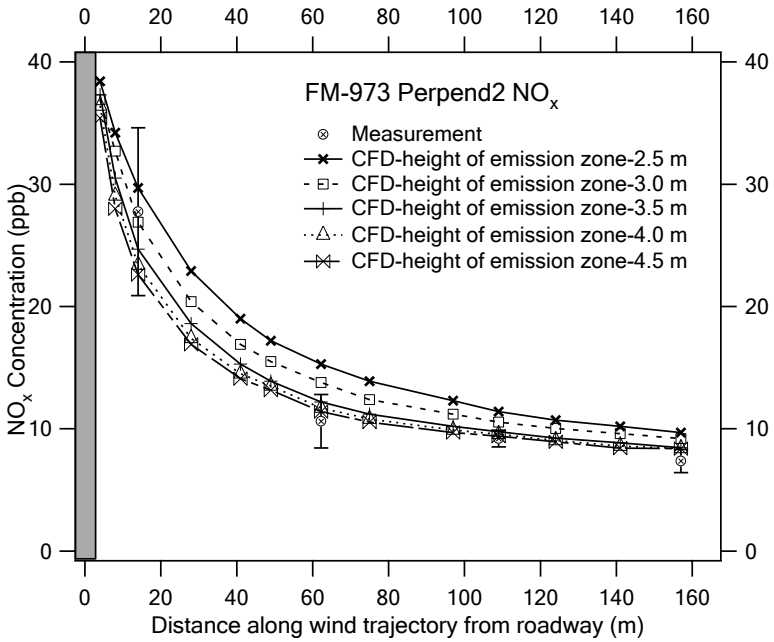

Figure 3.7. Comparison of NO_x concentration profiles under different heights of the emission zone for FM-973 Perpend2

We have conducted the sensitivity study on the height of the emission zone described in Section 3.3.1.3 for all the cases we studied. Figure 3.7 depicts the result for FM-973. The NOx concentrations with the height of the mixing zone of 2.5 and 3.0 m are significantly higher than the measured values, especially for the distance beyond than 50 m, while the results appear to be less sensitive to the height of the mixing zone as the height is larger than 3.5 m. In other words, choosing low height of the mixing zone is not appropriate for roadways with large diesel traffic fraction.

3.5 Conclusion

In this study, we expand the capabilities of the CTAG model to incorporate the coupling of turbulent mixing and chemical reactions. The resultant CTAG has been shown to be able to accurately capture the NO_X and NO_2 profiles in the vicinity of roadways under different meteorological parameters and road conditions. In comparison, CALINE4 is capable of predicting the NO_X profile, but underpredicted the NO_2 concentrations under high wind speed.

Our sensitivity analysis leads to two major implications in modeling the chemical evolution of nitrogen oxides near roadways. First, the initial NO_2/NO_X ratio should be carefully analyzed since it is one of the dominant parameters that influence the NO_2 profile. The commonly assumed 5% NO_2/NO_X ratio by volume (or 7.5% by mass) is very likely not suitable for most roadways, especially those with high heavy-duty truck traffic. The Second, high O_3 concentrations and high traffic volumes are of particular concern for near-road NO_2 exposure. Under such conditions, peak NO_2 concentration will likely occur near roadways (rather than on roadways), and elevated NO_2 concentration will persistent over a long distance downwind.

One limitation of the finite rate model, currently used in CTAG, is that it does not consider the influence of micro-scale turbulence in the vicinity of roadways, which may result in the small-scale nonhomogeneity on chemical reactions (Galmarini et al., 1995; Fraigneau et al., 1996). Without considering this micro-mixing, the CFD model may over-predict the NO_2 production rate under some circumstances (Gonzalez, 1997). Simulations considering the micro-mixing effect for on-road and near road chemical reactions should be further investigated.

CHAPTER 4

COUPLED TURBULENCE AND AEROSOL DYNAMICS MODELING OF VEHICLE EXHAUST PLUMES USING THE CTAG MODEL[*]

Abstract

This chapter presents the evaluation of the CTAG model in simulating the dynamics of individual plumes in the "tailpipe-to-road" stage, i.e., VIT behind a moving van and aerosol dynamics in the wake of a diesel car by comparing the modeling results against the respective field measurements. Combined with sensitivity studies, we analyze the relative roles of VIT, sulfuric acid induced nucleation, condensation of organic compounds and presence of soot-mode particles in capturing the dynamics of exhaust plumes as well as their implications in vehicle emission controls.

4.1 Introduction

Turbulent reacting flows have been extensively studied in many fields such as combustion (Pope, 2008; Wang and Pope, 2011) and chemical reactor engineering (Fox, 2003). In comparison, its applications in environmental problems still need considerable improvement. For example, a number of studies have investigated the initial evolution of exhaust particles emitted from tailpipes using turbulent reacting flow models (Uhrner et al., 2007; Albriet et al., 2010; Liu et al., 2011), which have

[*]Wang, Y., Zhang, K. M. Coupled turbulence and aerosol dynamics modeling of vehicle exhaust plumes using the CTAG model. Atmospheric Environment. 2012, 59: 284-293.

advanced our understanding of the plume processing of vehicular emissions. However, many important processes were missing in the previous studies such as turbulence flow simulations (Zhang et al., 2004), vehicle-induced turbulence (Albriet et al. 2010), and the condensation of organic compounds (Liu et al. 2011). In addition, applications of turbulent flow models on near-road air quality are rare (Baik et al., 2007; Wang et al., 2011b). Furthermore, even fewer studies so far, to the best of our knowledge, have examined how turbulent reacting flows affect air quality in micro-environments, where the presence of urban features such as roadways, building, and vegetation leads to substantial spatial variations of air pollutants.

The main objective of this chapter is to expand the capability of our CTAG model, which stands for Comprehensive Turbulent Aerosol Dynamics and Gas Chemistry for air quality, transportation, and climate applications. We incorporate all major turbulent mixing processes and aerosol dynamics/gas chemistry processes into the computational fluid dynamics (CFD) framework. This chapter is organized as follows. First, we introduce the structure of the CTAG model for roadway air quality study. Then we will evaluate various CTAG components and conduct related sensitivity analyses on the turbulence field and aerosol dynamics in the wakes of moving vehicles.

4.2 CTAG framework and components

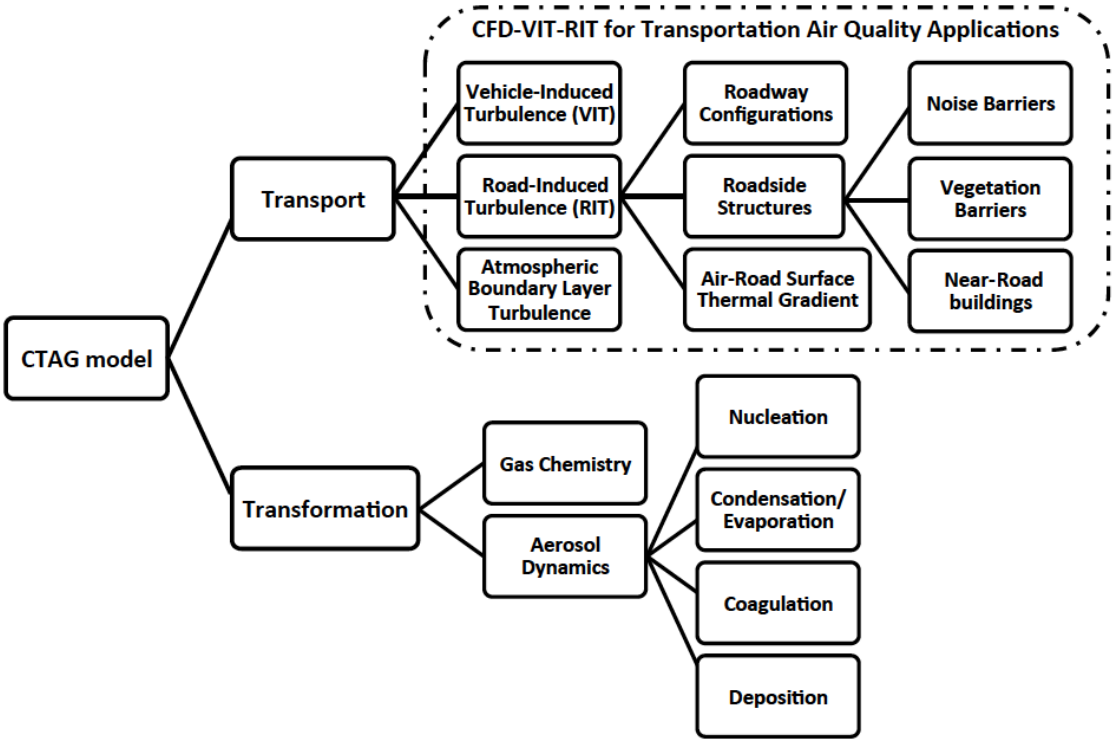

Figure 4.1. CTAG framework and components

Figure 4.1 illustrates the framework and components of the CTAG model. We will introduce the model based on the two major categories, transport and transformation, followed by a description on how they are coupled. In this chapter, our discussions will focus on roadway air quality applications. It should be noted that CTAG is designed as a general environmental turbulent reacting flow model. Its applications can be expanded beyond the roadway applications, e.g., the turbulent flow fields and aerosol dynamics of exhaust from a diesel engine inside the dilution tunnels.

4.2.1 Transport

The transport portion of CTAG solves the turbulence flow field within the computational domain using a CFD solver, ANSYS FLUENT. CTAG's transport model designed for roadway applications is called CFD-VIT-RIT, which is described and evaluated in our previous studies (Chapter 2; Chapter 3; Steffens et al., 2012; Tong et al., 2012). CFD-VIT-RIT explicitly simulates vehicle-induced turbulence (VIT), road-induced turbulence (RIT) and atmospheric boundary layer turbulence (ABLT). VIT originates from the interaction between moving vehicles and ambient air. It plays a dominant role in the on-road dispersion of pollutants and is strongly related to traffic volume, vehicle type and speed. The mechanisms being considered for RIT include roadway configurations (i.e., highway embankment, highway viaduct, or cut-sections), air-road surface thermal gradient and roadside structures such as sound barriers, vegetation barriers and roadside buildings. ABLT plays an important role in the dispersion of pollutants near-road and is affected by atmospheric stability, upwind and downwind terrain, ground roughness and urban structures. Detailed treatment of on-road and near-road turbulent mixing processes is critical. In Chapter 2, it is showed that a generic CFD model without such detailed treatment is not adequate in simulating the dispersion near complex near-road environments.

4.2.2 Transformation

The transformation portion of CTAG simulates the physical and chemical changes in the properties of pollutants due to gas-phase chemistry and aerosol dynamics (Pandis et al., 1995). The individual components are described as follows.

4.2.2.1 Gas chemistry

Chemical evolution of gas-phase pollutants in the atmosphere starts occurring right after exhaust exits the tailpipes and continues to near-road and ambient environments. CTAG simulates the gas-phase chemical reactions and their coupling with turbulent mixing on and near roadways. The model is flexible in terms of the chemical mechanisms and the number of reacting species to incorporate. Wang et al., (2011b) applied the Finite-Rate Model in CTAG to simulate the NOx chemistry near two Texan highways using two sets of species: one with three reacting species (i.e., NO, NO_2 and O_3) and the other with eight reactive species (NO, NO_2, O_3, HONO, OH, RO, HO_2 and RO_2). A complete set of chemical mechanisms such as CB05 (Gery et al., 1989; Yarwood et al., 2005) and SAPRC 99 (Carter, 2000) can be incorporated into the CTAG framework. CTAG is shown to be capable of predicting both NOx and NO_2 profiles downwind.

4.2.2.2 Aerosol dynamics

The integrated aerosol dynamics module in CTAG describes the evolution of particle number concentration (PNC), particle size distribution (PSD) and chemical composition of a multi-component aerosol. The Reynolds-averaged Population Balance Equation (PBE), i.e., for the local rate of change of the number concentration n of particles with the mass between m to m+dm, can be formulated as:

$$\left\langle \frac{\partial n(m,x,t)}{\partial t} \right\rangle + \langle \nabla(u \cdot n) \rangle + \left\langle \frac{\partial}{\partial m} G \cdot n \right\rangle = \langle D\nabla^2 n \rangle + \langle J(m')\delta(m-m') + \frac{1}{2}\left\langle \int_0^{\infty} \beta(m-m',m')n(m-m',x,t)n(m',x,t)dm' \right\rangle - \left\langle \int_0^{\infty} \beta(m,m')n(m,x,t)n(m',x,t)dm' \right\rangle - \alpha\langle v_d \cdot n \rangle \quad (4.1)$$

In multi-component aerosol, $m = \sum_1^{Ns} m_i$, where Ns is the number of chemical components for particles with mass between m and m+dm. PNC is defined as the total number concentration, i.e., summing up particles of all sizes. The second term on the left-hand side (LHS) of Equation (4.1) represents advection by the carrier gas. The third term on the LHS represents growth of particles as a result of condensation/evaporation of condensable species. G is the mass growth rate due to gas-particle partitioning**.** The first term on the right-hand side (RHS) describes the turbulent and molecular diffusion of the particles. The second term on the RHS is the nucleation rate, J. The third and fourth terms on the RHS of Equation (4.1) describe the coagulation process with β representing the binary coagulation coefficient**.** The last term on the RHS represents the loss due to the dry deposition within the vegetation canopy. α is the leaf area density and v_d is the deposition velocity of the particles.

PSD is represented by a fixed-bin, moving-center sectional structure, in which size-bin edges are fixed but size-bin centers vary between the low and high edges of the bin (Jacobson 1997). The number of bins can be selected based on the specific applications and associated computation cost. Particulate species include organic compounds (OC), elemental carbon (EC), sulfuric acid and water. OC can be further divided into volatile, semi-volatile and low-volatile groups based on the volatility distribution. The current model takes the internally-mixed assumption, which means that particles of a given size have the same composition. The source-oriented version is under development. The aerosol dynamics module is written in C-language by the

authors of this chapter and incorporated into ANSYS FLUENT through User-Defined Function.

Nucleation

Nucleation is the process of spontaneous formation of new particles from gas-phase precursors. The rapid cooling of hot exhaust by entrainment of ambient air, either in a laboratory dilution tunnel during engine testing or in the atmosphere near the exit of a tailpipe, results in high super-saturation ratios that trigger sulfuric acid-water homogeneous nucleation, generating nuclei around 1 nm. The nucleation rate, J (particles cm^{-3} s^{-1}), strongly depends on the turbulent mixing process and precursor concentrations. The parameterized binary nucleation model of sulfuric acid and water, which is valid for the temperature range relevant to on-road and near-road environments, is incorporated into CTAG (Vehkamaki et al., 2002; Vehkamaki et al., 2003). In the future, other types of nucleation mechanisms can be included for appropriate applications. The timescale for integrating nucleation rates is taken as:

$$\tau_{nuc} = \frac{PNC}{J}$$

(4.2)

Condensation and Evaporation

Partitioning of semi-volatile and low-volatile organic compounds between the gaseous and particulate phases will result in condensation or evaporation of condensable materials to and from particles. The dynamic gas/particle portioning

formulation is taken as that presented in Zhang et al. (2004), which considers both the Kelvin effect and Raoult's Law. The specific treatment of condensation/evaporation in diluting plumes is described in Section 4.3.2.1. Due to the differences in the time scales of various dynamic processes, an asynchronous time-stepping integrator is employed to reduce the stiffness in numerical integration of gas-particle partitioning (Zhang and Wexler, 2006).

Coagulation

Coagulation is the process that two particles collide to form a larger particle. For aerosol particles smaller than 500 nm, Brownian coagulation is the dominant inter-particle phenomenon (Seinfeld and Pandis, 2006).

Dry deposition on vegetation canopy, ground surface, and building surface

Dry deposition of gaseous and particulate species removes pollutants from the atmosphere. CTAG treats the dry deposition on vegetation as a sink term in the PBE as shown in Equation 4.1. Deposition of particles on the surfaces of ground (bare soil or covered by grass and road surface) and building (wall and roof) are treated as the boundary condition in the PBE. Detailed description of deposition formulation in CTAG is presented in the Section 4.3.1.1 and in Steffens et al., (2012).

4.2.3 Coupling of transport and transformation

Turbulent reacting flows are characterized by complex interactions between turbulence, scalar transport, chemical reactions and aerosol dynamics. There are two

main approaches in simulating the interactions or the coupling between transport and transformation. One is to carry out simulations on mean properties, i.e., without considering the effects of turbulent fluctuations on chemical reactions and aerosol dynamics. The other is to consider the fluctuations from the mean spatial and temporally and their effects on chemical reactions and aerosol dynamics. Currently, we have taken the first approach in CTAG. Taking aerosol dynamics as an example, the coupling essentially involves calling the aerosol processes in every cell and at every time step, and mean PNCs are used for numerical calculations. The implementation of the second approach in CTAG is under development.

We adopt the timestep splitting (also referred to as operator splitting) method (Oran and Boris, 2005) to couple turbulence and aerosol dynamics simulations. We refer to τ_{turb} as the timescale for turbulence flow simulation, which is conducted by the commercial turbulence solver. The aerosol dynamics simulation is postulated as an initial value problem with the integration interval as τ_{turb}. Within the aerosol dynamics, nucleation is a much faster process than condensation/evaporation, while coagulation and deposition are considerably slower than both of them (Zhang and Wexler, 2004). When nucleation happens, the timescale for aerosol dynamics simulation is chosen uniformly as τ_{nuc} to make sure that the interactions between nucleation, condensation/evaporation, coagulation and deposition can be resolved. When nucleation is not viable, the rest of the processes are integrated indecently with their inherent timescales (Oran and Boris, 2005; Zhang and Wexler, 2002).

Besides the numerical coupling method, there are also two ways to couple the motion of the particles with the flow field: the Eulerian/Eulerian frame and

Eulerian/Lagrangian frame. For the sub-micron particles, which have a Stokes number much less than one, it is reasonable to assume that they will follow the flow streamline. Meanwhile, due to their relatively low concentrations, those particles do not affect the turbulent flow field. Therefore, the Eulerian framework for both particles and flow field is suitable for this type of problem. For micron or larger particles, the forces between the flow field and particles need to be resolved, and those particles do not follow the streamline because of their inertia. To track their positions, the stochastic tracking method such as the Random Walk model is needed, where particles are simulated as a discrete phase in the Lagrangian framework, while the flow field is simulated as the continuous phase in the Eulerian framework. Simulations presented in this chapter are conducted in the Eulerian/Eulerian framework, while Steffens et al. (2012) adopt a Eulerian/Lagrangian framework.

4.2.4 Unsteady-state simulations and coupling of time steps

Unsteady-state simulations are employed in CTAG. There are two types of boundary conditions for the unsteady simulations: with time-constant boundary conditions and with time-varying boundary conditions. With time-constant boundary conditions, unsteady-state simulations undergo two stages. First, as emission sources are injected into background environment, the spatial distributions of pollutants are being formed over time (i.e., the transient-state). Second, with constant injection of emission sources, the statistically steady-state is reached after a certain period of time and the simulation result can be sampled and averaged for the statistically steady-state. With time-varying boundary conditions, unsteady-state simulations may not reach the

statistically steady-state and remain in the transient-state. CTAG is able to conduct both types of unsteady-state simulations, depending on the nature of the problems.

4.3 Model evaluations

CTAG simulates a large number of interacting physical and chemical processes related to roadway air quality. For such a comprehensive model, it is crucial to evaluate the scientific robustness of each component. Previously, we validate its transport part (CFD-VIT-RIT) in modeling dispersion of inert species (carbon monoxide) near different highway configurations in Chapter 2, NOx chemistry near roadways in Chapter 3, spatial variations of black carbon particles in urban highway-building environments (Tong et al., 2012), and particle transport and deposition across vegetation barriers (Steffens et al., 2012). In this section, we will present the evaluation of CTAG in simulating the transport and transformation of individual plumes.

4.3.1 Turbulent flow field in the wake of an individual vehicle

We first evaluate CTAG in resolving the turbulent flow field behind a single vehicle by testing against turbulence measurements in vehicle wakes conducted by Rao et al., (2002). In the field measurement, 3-D sonic anemometers were installed on an adjustable pipe scaffolding on an open platform trailer, which was towed by a full-sized van moving on a 1524 m long airport runway at Rockwood, TN (Rao et al., 2002; Hosker et al., 2003). To minimize the impact of the platform of the wake airflow, the trailer flooring was removed, leaving only the main supporting structure.

The scaffolding was designed to enable various sampling positions during the experiment, i.e., the top three anemometers were placed at 3.7 m, higher than the top of the van to provide measurements that would be above the wake cavity zone of the van (Hosker et al., 2003). The van operated at two speeds, 13.4 m s^{-1} (30 mph) and 13.4 m s^{-1} (50 mph). The dimensions of the van are 5.0 m (L) by 1.9 m (W) by 2.1 m (H). During the experiments, the ambient winds were light and effectively parallel to the runway.

4.3.1.1 Simulation set-up

We created several on-road computational domains with respect to the different sets of measurements. Figure 4.2 shows one example of the domain with the full-sized van and its trailer (the anemometers were placed 0.6 m away from the rear of the van). This domain has dimensions of 80x50x30 m (x-y-z) and is meshed with approximately 3 million unstructured tetrahedral cells. Mesh independence study (the domain meshed with 4.5 million cells) has been conducted to make sure that the grid resolution to be fine enough for the accuracy of the simulation result. That is, the greatest difference observed between the two calculations is a 5% increase in the TKE behind the vehicle on the finer mesh. The finest mesh resolution is created for the near-vehicle region, increasing exponentially in x-, y- and z-directions towards the outer boundaries of the domain. The smallest cell size is 0.005 m, while the largest cell size is 0.5 m. In our simulation, the van is set to be stationary, while the inlet air is blowing towards the van. The surfaces of the van and the trailer are set as “wall”, for which a no-slip condition has to be satisfied. The inlet wind velocity is taken as the sum of the vehicle

velocity and ambient wind velocity. In addition, the roadway surface is set to have the same velocity as the van to avoid generating the ground surface boundary layer artificially. Symmetric boundary conditions are set to lateral and the top planes of the domain, representing a zero flux of all quantities. For the outflow condition shown in Figure 4.2, a zero normal first derivative of all quantities is fulfilled. We select unsteady renormalization group (RNG) $k-\varepsilon$ turbulence model for the turbulence simulation:

- The momentum equation is:

$$\frac{\partial(\rho u_i)}{\partial t}+u_j\frac{\partial(\rho u_i)}{\partial x_j}=\rho\left(\frac{\rho-\rho_n}{\rho_n}\right)g_i-\frac{\partial p}{\partial x_i}+\frac{\partial}{\partial x_j}\left(\mu\left(\frac{\partial u_j}{\partial x_i}+\frac{\partial u_i}{\partial x_j}\right)-\rho\overline{u_i'u_j'}\right)+S_u \qquad (4.3)$$

where

$$-\rho\overline{u_i'u_j'}=\mu_t\left(\frac{\partial u_i}{\partial x_j}+\frac{\partial u_j}{\partial x_i}\right)-\frac{2}{3}\rho k\delta_{ij} \qquad (4.4)$$

$$\mu_t=\rho C_\mu\frac{k^2}{\varepsilon} \qquad (4.5)$$

$$\frac{\rho-\rho_n}{\rho_n}=-\beta_T(T-T_n) \qquad (4.6)$$

g_i is the gravitational acceleration in the ith direction coordinate $(0,-g,0)$, β_T is the thermal expansion coefficient, and $C_\mu=0.0845$ is constant. ρ_n and T_n are the density and temperature of the ambient air, respectively. S_u is the momentum source term induced by the vegetation barrier. The momentum drag due to vegetation is proportional to the plant coefficient of drag, C_D (dependent on the tree type) and the

leaf area density, LAD (ratio of leaf surface area to total volume occupied by vegetative element). Thom (1975) gives the modeled sink term, S_u, to be:

$$S_u = -\rho C_D LAD u^2 \tag{4.7}$$

- The transport equations for TKE, k and turbulent dissipation rate, ε are:

$$\frac{\partial \rho k}{\partial t} + \frac{\partial (\rho k u_i)}{\partial x_i} = \frac{\partial}{\partial x_j}\left(\alpha_k \mu_{eff} \frac{\partial k}{\partial x_j} \right) + G_b + P_w + P_s + S_k - \rho\varepsilon \tag{4.8}$$

$$\frac{\partial (\rho\varepsilon)}{\partial t} + \frac{\partial (\rho\varepsilon u_i)}{\partial x_i} = \frac{\partial}{\partial x_j}\left(\alpha_\varepsilon \mu_{eff} \frac{\partial \varepsilon}{\partial x_j} \right) + G_{\varepsilon 1} \frac{\varepsilon}{k}(P_w + P_s + C_{\varepsilon 3} G_b) + S_\varepsilon - C_{\varepsilon 2} \rho \frac{\varepsilon^2}{k} - R \tag{4.9}$$

where

$$G_b = -\beta g_j \frac{\mu_t}{\mathrm{Pr}_t} \frac{\partial T}{\partial x_i} \tag{4.10}$$

$$P_s = \mu_t \frac{\partial u_j}{\partial x_i}\left(\frac{\partial u_i}{\partial x_j} + \frac{\partial u_j}{\partial x_i} \right) \tag{4.11}$$

$$R = \frac{C_\mu \rho \eta^3 (1 - \eta/\eta_0)\varepsilon^2}{(1 + \beta\eta^3)k} \tag{4.12}$$

μ_{eff} is the effective viscosity. α_k and α_ε are the inverse effective Prandtl number for k and ε, respectively. $\eta = Sk/\varepsilon$ is the scalar measure of the deformation tensor. G_b is the turbulence production due to buoyancy of heated air close to the surface of roadway and building roof. P_w and P_s are the generation of TKE due to the shear effect and wake effect, respectively, caused by the movement of vehicles and the existence of building structures. Pr_t is the turbulent Prandtl number. S_k and S_ε are the

source term of TKE and turbulent dissipation rate induced by vegetation barrier, respectively.

The model constants for RNG $k-\varepsilon$ turbulence model are:

$$C_{1\varepsilon}=1.42\,,C_{2\varepsilon}=1.68\,,\alpha_k=\alpha_\varepsilon=1.393\,,\eta_0=4.38\ ,\beta=0.012 \qquad (4.13)$$

- The pollutant concentration equation is:

$$\frac{\partial(\rho C_i)}{\partial t}+\frac{\partial(\rho u_i C_i)}{\partial x_i}=\frac{\partial}{\partial x_i}\left(\rho D_m+\frac{\mu_t}{Sc_t}\right)\frac{\partial C_i}{\partial x_i}+S_i \qquad (4.18)$$

C_i is the concentration of pollutants, D_m is the molecular diffusivity coefficient, and Sc_t is the turbulent Schmidt number. S_i is the source term of pollutants, and for inert species, S_i is set related to roadway emission, while chemical reactions need to be considered for reactive species. S_i is more complicated for aerosol particles, since the mechanisms of nucleation, condensation and evaporation, coagulation and deposition are incorporated in.

Deposition on ground (bare soil or covered by grass) and building surface (wall and roof) is considered as the boundary condition in the PBE. The deposition flux of pollutants is (Seinfeld and Pandis, 2006):

$$F_i=-v_d C_i \qquad (4.19)$$

4.3.1.2 Results and discussion

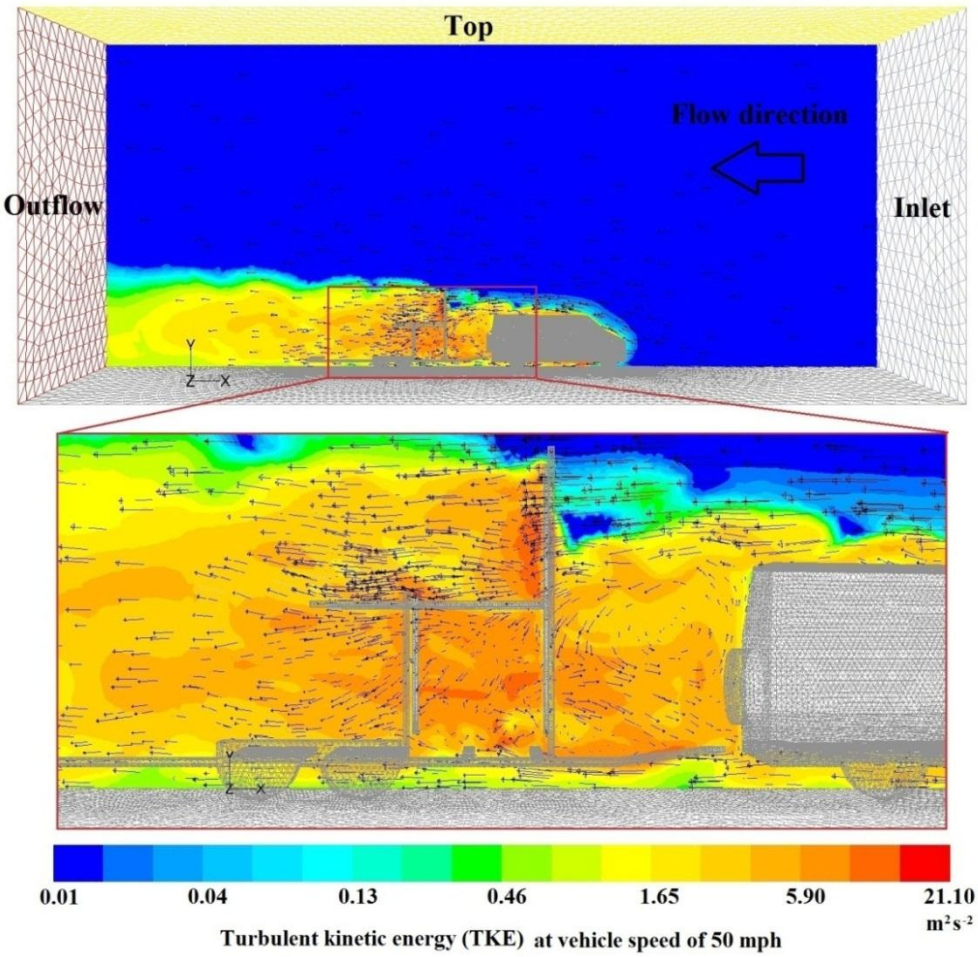

Figure 4.2. Computation domain of a full-sized van with its trailer and TKE profile with the velocity vector of the flow field at vehicle speed of 50 mph

Figure 4.2 illustrates the contour of turbulent kinetic energy (TKE) when the full-sized van is running at the speed of 50 mph. It can be seen that TKE is generated in the wake of the vehicle and enhanced by the existence of the trailer frame. The values of generated TKE are significantly higher than the ambient turbulence level, suggesting the strong influence of VIT on the flow field. Shown in Table 4.1, the maximum vertical TKE occurs at the height of 1.8 m (y-axis), and then decreases quickly from 1.8 m to 2.7 m. At the height of 3.7 m, TKE returns to the ambient value, which is in accordance with the experiment. Since the height of the van is only 2.1 m, at the height of 2.7 m, instead of being produced by the wake effect, turbulence is

either generated by the shear effect or transported from elsewhere before being dissipated. At the height of 3.7 m, the production of turbulence is small due to negligible shear effect, and transported turbulence is dissipated quickly due to viscous force before reaching up to that height. TKE also varies horizontally. While moving away at 0.6 m from the rear side of the van (i.e., along x-axis), TKE first increases and reaches the maximum value at 2.7 m (x-axis), where the turbulence field is fully developed. Then TKE decreases while moving away from the van.

Table 4.1 Comparisons of TKE values between measurement and CTAG at different speeds and locations

Location (x-y-z)	Vehicle speed (mph)	TKE by measurement (m^2 s^{-2})	TKE by CTAG (m^2 s^{-2})	Difference between measurement and CTAG (Based on measurement)
0.6-1.8-0	50	4.23 ±1.27	3.66 ±1.44	-13.5%
0.6-2.7-0	-	1.09 ±0.33	1.27 ±0.61	16.5%
0.6-3.7-0	-	~ 0	~ 0	
2.7-1.8-0	-	5.14 ±1.83	4.78 ±1.12	-7.0%
2.7-2.7-0	-	1.61 ±0.49	1.47 ±0.69	-8.7%
2.7-3.7-0	-	~ 0	~ 0	
3.7-1.8-0	-	3.43 ±0.96	3.05 ±0.96	-11.1%
3.7-2.7-0	-	0.42 ±0.13	0.37 ±0.09	-11.9%
3.7-3.7-0	-	~ 0	~ 0	
0.6-1.8-0	30	3.32 ±0.95	2.64 ±0.93	-20.5%
0.6-2.7-0	-	0.75 ±0.20	0.81 ±0.40	8.0%
0.6-3.7-0	-	~ 0	~ 0	
2.7-1.8-0	-	3.79 ±1.06	3.25 ±0.74	-14.2%
2.7-2.7-0	-	0.91 ±0.32	0.76 ±0.21	-16.5%
2.7-3.7-0	-	~ 0	~ 0	
3.7-1.8-0	-	2.25 ±0.68	1.79 ±0.24	-20.4%
3.7-2.7-0	-	0.28 ±0.07	0.23 ±0.07	-17.9%
3.7-3.7-0	-	~ 0	~ 0	

A comparison between the predicted and measured TKE for each sampling point is presented in Table 4.1, and the model evaluation statistics for CTAG is summarized in Table 4.2. With small MNE (<0.150) and MFE (<0.100), and high R (>0.900), CTAG has been demonstrated to have a good capability of capturing the turbulent flow field in the wake of a moving vehicle and therefore can provide a solid foundation for the simulations of transformation of vehicle plumes.

Table 4.2 Results of model performance evaluation for CTAG by field measurements

	MNB	MNE	MFB	MFE	FB	MG	NMSE	VG	R	FAC2
TKE values in the wake of a full-sized van with trailer (Corresponding to Table 4.1)	-0.098	0.138	-0.070	0.096	0.122	1.115	0.030	1.025	0.910	1.000
PNC for Case 1 and Case 2 at 0.45 and 0.90 m	-0.094	0.094	-0.066	0.066	0.061	1.106	0.005	1.015	0.921	1.000
PSD for Case 1: 148 km h^{-1}, 4000 rpm at 0.45 m (Corresponding to Figure 4.5a)	-0.051	0.111	-0.039	0.077	0.032	1.064	0.063	1.024	0.918	1.000
PSD for Case 1: 148 km h^{-1}, 4000 rpm at 0.90 m (Corresponding to Figure 4.5a)	-0.215	0.239	-0.161	0.177	0.130	1.300	0.086	1.112	0.916	1.000
PSD for Case 2: 105 km h^{-1}, 2300 rpm at 0.45 m (Corresponding to Figure 4.5b)	0.114	0.179	0.037	0.081	0.037	0.953	0.003	1.090	0.937	0.938
PSD for Case 2: 105 km h^{-1}, 2300 rpm at 0.90 m (Corresponding to Figure 4.5b)	-0.251	0.221	-0.165	0.169	0.203	1.326	0.064	1.191	0.928	0.875

MNB: Mean normalized bias; MNE: mean normalized error; MFB: mean fractional bias; MFE: mean fractional error; FB: fractional bias; MG: geometric mean bias; NMSE: normalized mean square error; VG: geometric variance; R: correlation coefficient; FAC2: fraction of predictions within a factor of two of observations. MNB, MNE, MFB and MFE are described in Boylan and Russell (2006), and FB, MG, NMSE, VG, R and FAC2 in Chang and Hanna (2004).

4.3.2 Aerosol dynamics in a diluting diesel vehicle exhaust plume

4.3.2.1 Baseline simulations

CTAG is further tested by simulating aerosol dynamics in diluting diesel plumes. The simulation results are compared against the freeway measurements described in

Uhrner et al. (2007 and 2011) and Wehner et al. (2009). Measurements were conducted on a public 4-lane freeway (A38). The traffic density was low (0.4 cars km^{-1} and 0.2 heavy duty vehicles km^{-1}) because the freeway was partially closed during the measurement period. The testing vehicle was a European 2003 station wagon with a 74 KW diesel engine. The dimensions of the vehicle were 4.3 m (L) by 1.7 m (W) and 1.5 m (H). The sampling inlet and sensor system of measurement devices were mounted behind the vehicle. The sampling inlet was mounted at either 0.45 or 0.9 m to the tailpipe. PSDs from 7 to 400 nm in diameter were measured using a Scanning Mobility Particle Sizer (SMPS). Each scan for the SMPS took 90 s, and the result for each driving condition was reported as the average of scans within 15 min.

Simulation set-up

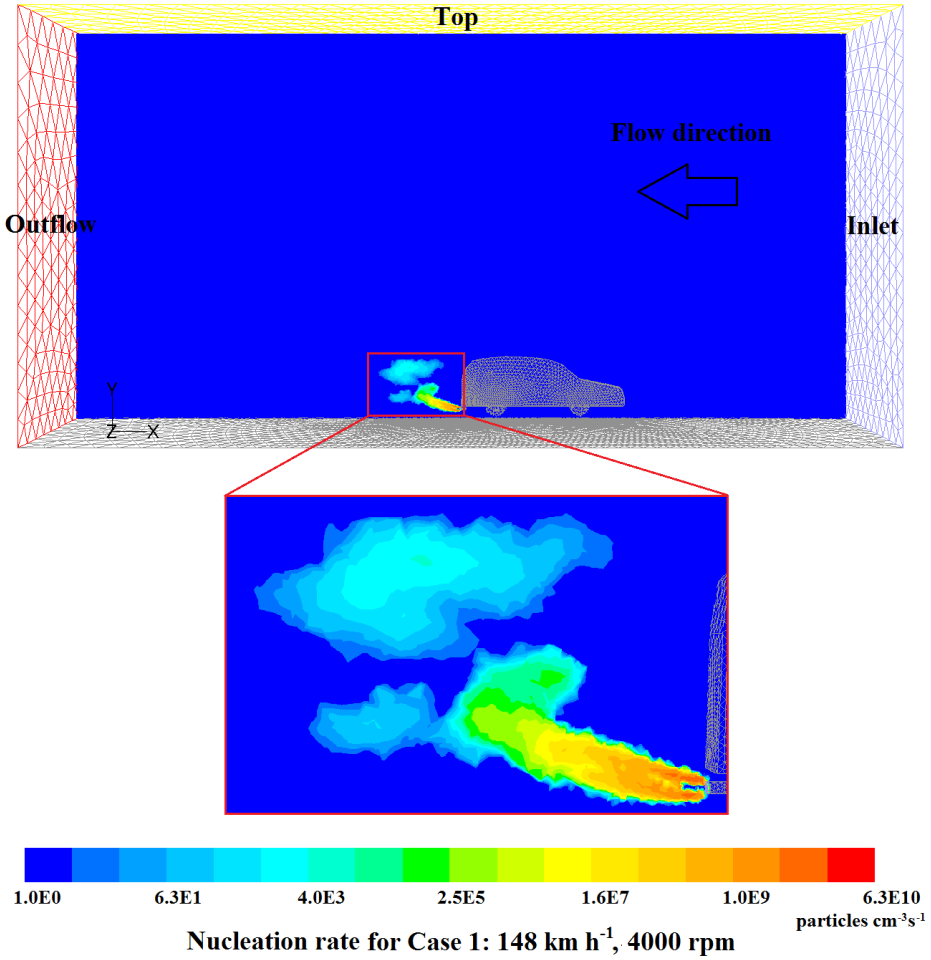

Figure 4.3. Computational domain for a diluting diesel plume and the contour of instantaneous nucleation rate for Case 1 (Base Case): 148 km h^{-1}, 4000 rpm

The schematic diagram of the computational domain is shown in Figure 4.3. The domain has dimensions of 80x50x30 m (x-y-z) and ~3.2 million cells. Mesh independence study (the domain meshed with 1.6 million and 4.8 million cells) has been conducted to make sure that the grid resolution to be fine enough for the accuracy of the simulation result. The setup of the computational domain is the same as the full-sized van with trailer in Section 3.1, except that velocity inlet is set for both ambient air and tailpipe. The ambient air inlet includes ambient temperature, relative

humidity (RH) and wind velocity as well as background PSD. The tailpipe inlet includes exhaust temperature, exhaust exit velocity, exhaust water content, PSD of pre-existing soot-mode particles, sulfuric acid concentration and organic carbon (OC) concentration. Two driving conditions described in Uhrner et al. (2007, 2011) and Wehner et al. (2009) are simulated, noted as Case 1 (vehicle speed at 148 km h^{-1} and engine speed at 4000 rpm) and Case 2 (vehicle speed 105 km h^{-1} and engine speed 2300 rpm). Case 1 and Case 2 serve as two baseline cases, and eight more cases are developed to investigate the sensitivities of concentrations of sulfuric acid, OC, and soot-mode particles. Unsteady RNG $k-\varepsilon$ turbulence model is used in the simulation. While the measurements covered the size range from 7 to 400 nm, the modeled size range is from 0.9 to 400 nm in 22 discrete bins.

Sulfuric acid concentration at the exit of the tailpipe plays an important role in determining the PNC. It depends on the fuel sulfur content (FSC), sulfur in the lubricant oil and the SO_2-to-SO_3 conversion rate (cr). FSC is around 7~10 ppm for the diesel fuel used in the field measurements (Uhrner et al., 2007). In addition, sulfur in lubrication oil also contributes to sulfuric acid concentration in the exhaust. It is estimated that the lubricant can make up to 6 ppm equivalent FSC (Uhrner et al., 2007; Kittelson et al., 2008). Therefore the total sulfur content is around 13~16 ppm. The installed oxidation catalyst converter may substantially increase cr depending on the exhaust temperature, noble metal and washcoat used in the oxidation catalyst (Arnold et al., 2006). Given the uncertainties in fuel and lubrication oil sulfur contents and their corresponding cr's, we acquired the exhaust sulfuric acid flow rate by matching the predicted and measured PNCs. The fitted exhaust sulfuric acid flow rate for Case 1

is 10.6×10^{-7} mol s^{-1}, which is close to the value of 9×10^{-7} mol s^{-1} used in the simulation of Uhrner et al. (2007). The fitted exhaust sulfuric acid flow rate for Case 2 is 3.5×10^{-7} mol s^{-1}, which is close to the value of 3×10^{-7} mol s^{-1} used in the simulation of Uhrner et al. (2007). The sensitivity analysis on sulfuric acid concentration will be discussed in Section 3.2.2.

While sulfuric acid is the main nucleating species, OC in the exhaust is responsible for the growth of nuclei and pre-existing particles. OC originate mainly from unburned fuel and lubricant oil (Jacobson et al., 2005). Laboratory studies showed that nucleation mode particles consist mainly of heavy hydrocarbons and their volatility resembles that of C_{24}-C_{32} long n-alkanes, implying a significant contribution from lubricant oil (Kittelson et al., 2006). There are also substantial quantities of polycyclic compounds and, in particular, polycyclic aromatic hydrocarbons (PAHs) that result from the combustion process (Schauer et al., 1999). We separate OC into volatile, semi-volatile and low-volatile groups. Among these groups, volatile OC is considered to have little impact on particle growth due to their large volatilities. Therefore semi-volatile and low-volatile groups are considered in CTAG. The organic compositions of vehicle emissions are dependent on the fuel type, the state of vehicle maintenance, engine load, vehicle speed and ambient conditions (Maricq et al., 1999; Andersson and Wedekind, 2001). Considering the range of OC volatility, $C_{20}H_{42}$ (saturation vapor pressure as 5.32×10^{-2} Pa at 298.15 ℃) is used to represent the first semi-volatile group for C_{18}-C_{22}. $C_{25}H_{52}$ (saturation vapor pressure as 7.85×10^{-5} Pa at 298.15 ℃) is used to represent the second semi-volatile group for C_{23}-C_{27}, while $C_{30}H_{62}$ (saturation vapor pressure as 4.17×10^{-7} Pa at 298.15 ℃) is for low-volatile group of C_{28}-C_{32} (Chemical

abstracts). Furthermore, a polycyclic organic compounds, $C_{16}H_{10}$ (saturation vapor pressure as 5.07×10^{-8} Pa at 298.15 ℃) is used to represents the polycyclic organic compounds (Albriet et al., 2010). The temperature dependence of saturation concentrations is described by the Clausius-Clapeyron equation. All three groups of organic compounds are assumed to reside in the gas-phase at the exit of the tailpipe due to the high temperature. When all C_{18}-C_{32} and $C_{16}H_{10}$ carbonyls are combined, they can account for 20-40 % of the gas-phase organic compound mass emissions for diesel engine (Schauer et al. 1999). Among the semi-volatile and low-volatile groups, fractions of $C_{20}H_{42}$, $C_{25}H_{52}$, $C_{30}H_{62}$ and $C_{16}H_{10}$ are estimated to be 59%, 19%, 5% and 17%, respectively, based on measurements and estimations (Schauer et al., 1999; Schauer et al., 2002; Donahue et al., 2006). OC emissions significantly increase at higher engine speed (Wehner et al., 2009). For Case 1 (vehicle speed 148 km h^{-1} and engine speed 4000 rpm), the total emission rate for C_{18}-C_{32} and $C_{16}H_{10}$ carbonyls is estimated as 240.0 mg/km. Therefore the emission rates for $C_{20}H_{42}$, $C_{25}H_{52}$, $C_{30}H_{62}$ and $C_{16}H_{10}$ are set to be 141.6, 45.6, 12.0 and 40.8 mg/km, respectively. For Case 2 (vehicle speed 105 km h^{-1} and engine speed 2300 rpm), the total emission rate for C_{18}-C_{32} and $C_{16}H_{10}$ carbonyls is approximated as 24.0 mg/km, about 1/10 of that of Case 1. The sensitivity analysis on OC emission rate will be discussed in Section 3.2.2.

Emission rates and size distributions of soot-mode particles for Case 1 and Case 2 are obtained from Uhrner et al. (2007).

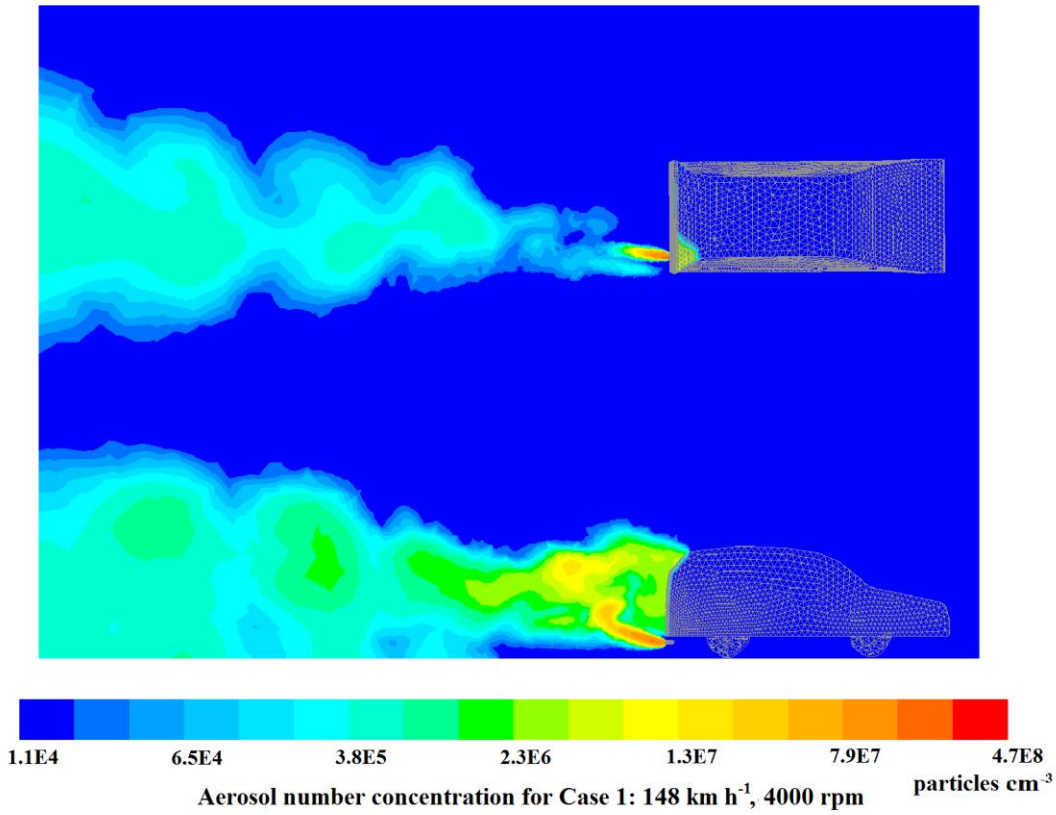

Figure 4.4. Contour of instantaneous PNC in the exhaust plume for Case 1 (Base Case): 148 km h^{-1}, 4000 rpm

Figures 4.3 and 4.4 depict the snapshots of nucleation rates and PNCs in contours from Case 1 simulations. Strongly affected by VIT, the shape of the exhaust plume is changing rapidly in the wake of the vehicle. Figure 4.3 suggests that the nucleation process takes place in the near-wake region. The maximum nucleation rates occur in the areas where the gradients of sulfuric acid, temperature, RH and dilution are the steepest, while no nucleation happens within the cone-shape zone immediately after the tailpipe due to the high exhaust temperature. The nucleation process ends quickly as the gaseous-phase sulfuric acid concentration is depleted due to dilution and

condensation onto pre-existing particles. Figure 4.4 illustrates that the highest PNC is present close to the tailpipe and then mixes with ambient air and dilutes rapidly due to VIT. There is also a recirculation zone near the rear of the vehicle that has less exchange with ambient air and therefore keeps relatively high particle concentration.

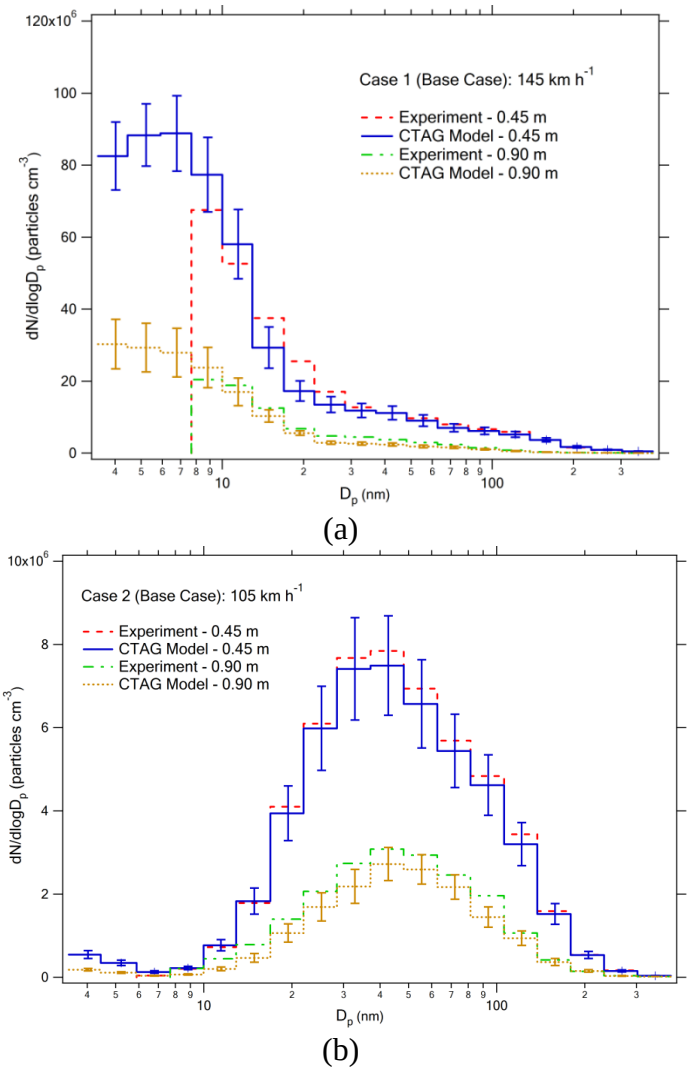

Figure 4.5. Predicted vs measured PSDs for two base cases, (a) Case 1 (Base Case): 148 km h^{-1}, 4000 rpm and (b) Case 2 (Base Case): 105 km h^{-1}, 2300 rpm

Depicted in Figure 4.5, the predicted PSDs are compared to the measurements at 0.45 and 0.90 m from the exit of the tailpipe for the two baseline cases: Case 1 (148 km h^{-1}, 4000 rpm) and Case 2 (105 km h^{-1}, 2300 rpm). Due to the nature of unsteady-

state simulations, the mean values for each bin are acquired within the statistically steady-state stage. The sampling period usually covers dozens of periods within the statistically steady-state stage. The error bars (one standard deviation of uncertainty) indicate the range of fluctuations. As shown in Figure 4.5(a) for Case 1, strong nucleation event occurs in the exhaust plume and nucleation mode particles have grown into a larger size due to the condensation of OC. As a result, there is no clear boundary between the nucleation mode and soot-mode. For Case 2, the lower sulfuric acid concentration results in a much smaller nucleation mode, shown in Figure 4.5(b). Consequently, the nucleation mode and the soot-mode are easily distinguishable.

Table 4.3 Comparison between predicted and measured PNCs for Case1 and Case2

	PNC by measurement (7-400 nm) (particles cm^{-3})	PNC predicted by CTAG (7-400 nm) (particles cm^{-3})	Difference between measurement and CTAG (Based on measurement)
Case 1 - 0.45 m	1.74×10^7	1.68×10^7	-3.40%
Case 1 - 0.9 m	5.29×10^6	4.65×10^6	-12.10%
Case 2 - 0.45 m	3.23×10^6	3.11×10^6	-3.70%
Case 2 - 0.9 m	1.31×10^6	1.07×10^6	-18.30%

A comparison of PNC and PSDs between predictions and measurements is presented in Table 4.2 and Table 4.3. With small MNE (<0.100) and MFE (<0.100), and high R (>0.900) for PNC, and average MNE (<0.200) and MFE (<0.150), and high R (>0.900) for PSDs, CTAG model shows adequate agreement with experimental data for capturing the aerosol dynamics in a diluting diesel vehicle exhaust plume.

4.3.2.2 Sensitivity analysis

To better understand the influence of different input parameters on aerosol dynamics, eight sensitivity studies (Cases 3-12) are conducted, which includes varying the concentrations of sulfuric acid, OC and soot-mode. As shown in Table 4.4, two

types of sensitivity studies have been conducted. Cases 3 - 9 mainly focus on the influence of the exhaust parameters on aerosol dynamics, while Cases 10 - 12 evaluate the relative importance of different aerosol processes. Specifically, Cases 3 and 4 vary the sulfuric acid concentrations, Cases 5 and 6 alter the OC concentrations and Cases 7 and 8 vary the soot-mode concentrations. Case 9 varies the sulfuric, OC and soot-mode concentrations.

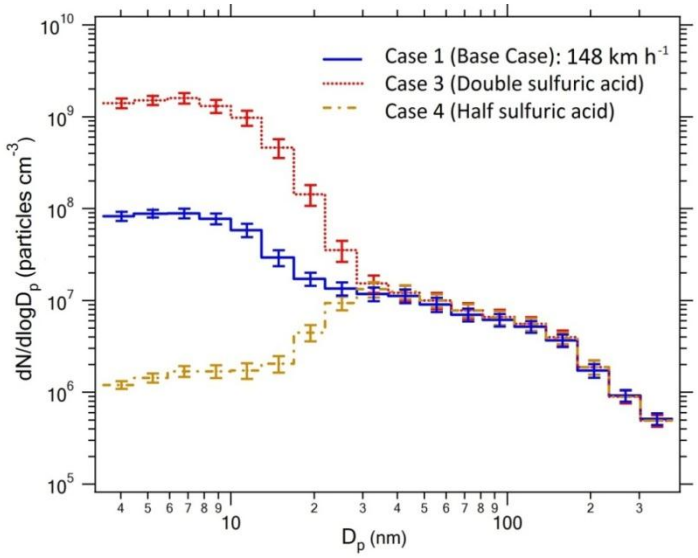

(a)

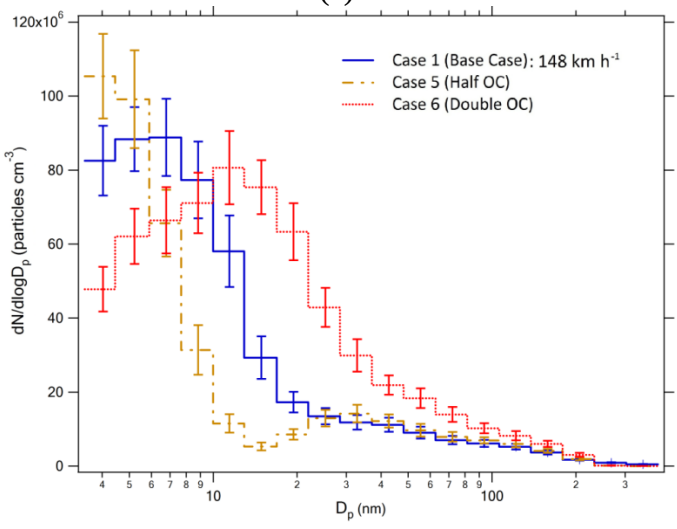

(b)

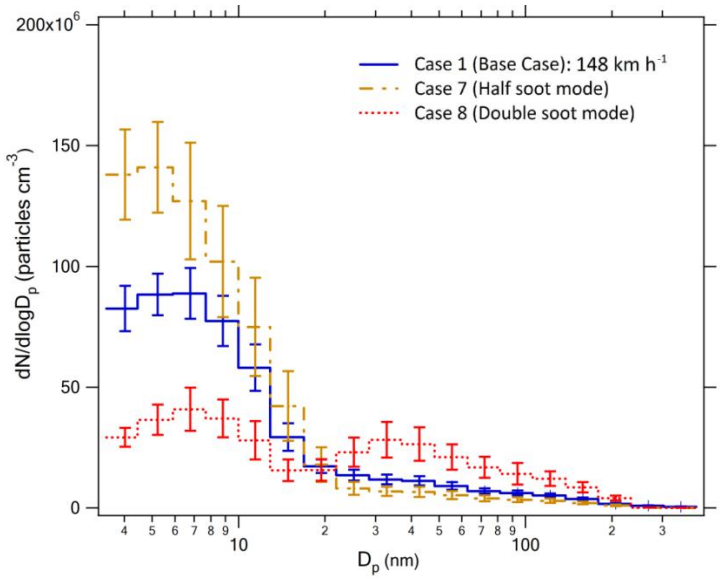
200x10^6
150
100
50
0
dN/dlogD_p (particles cm^-3)
Case 1 (Base Case): 148 km h^-1
Case 7 (Half soot mode)
Case 8 (Double soot mode)
4 5 6 7 8 9 10 2 3 4 5 6 7 8 9 100 2 3
D_p (nm)

(c)

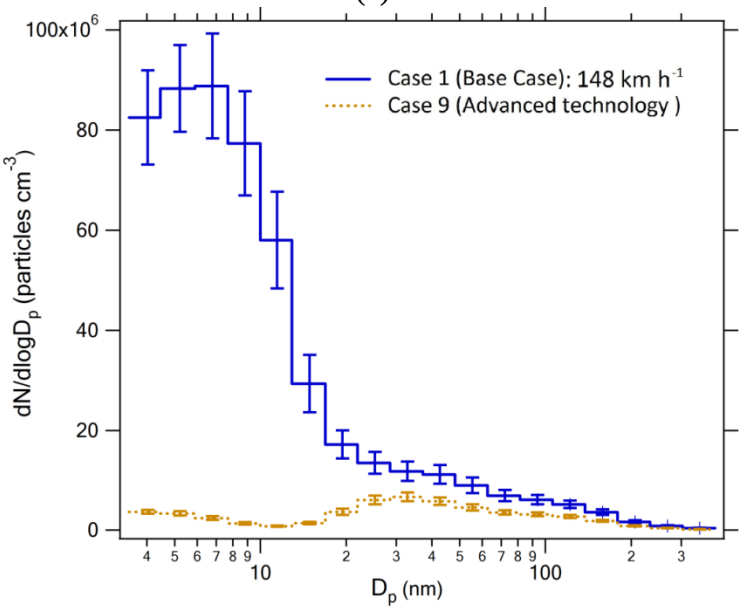
100x10^6
80
60
40
20
0
dN/dlogD_p (particles cm^-3)
Case 1 (Base Case): 148 km h^-1
Case 9 (Advanced technology)
4 5 6 7 8 9 10 2 3 4 5 6 7 8 9 100 2 3
D_p (nm)

(d)

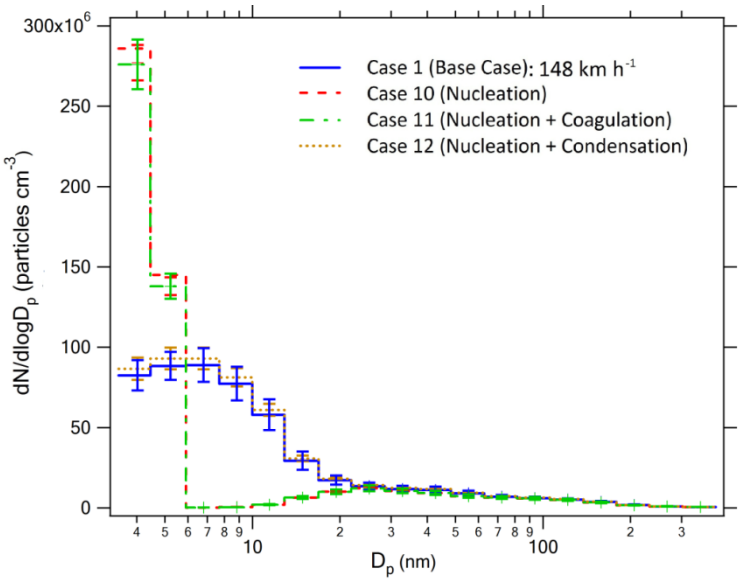

(e)

Figure 4.6. Predicted PSDs for Cases 3 – 12 compared to Case 1 (Base Case): 148 km h^{-1}, 4000 rpm. (a) The dependence of PSDs on sulfuric acid concentration. Note that logarithmic scale is used on the y-axis. (b) The dependence of PSDs on the OC concentration. (c) The dependence of PSDs on the soot-mode particle concentrations. (d) The effects of advanced emission control technology (Half sulfuric acid flow rate, half OC emission rate and half soot-mode emission factor) on PSDs. (e) The relative importance of each aerosol dynamics process on PSDs

Figure 4.6a mainly shows the dependence of PSDs on sulfuric acid concentration, which is strongly related to FSC, and lubricate oil and cr. The reduction in the sulfuric acid flow rate can be achieved by replacing a lower sulfur content fuel and lubricate oil. Compared with Case 1 (Base Case), the double sulfuric acid flow rate in Case 3 results in the nucleation mode about 16.9 times higher, while the half sulfuric acid flow rate in Case 4 leads to the nucleation mode about 36.5 times smaller, which suggests a highly nonlinear relationship between nucleation and sulfuric acid concentration.

Table 4.4 Base and sensitivity cases for simulating aerosol dynamics in a diluting diesel plume

Case ID	Sulfuric acid flow rate (mol s^{-1})	OC emission rate (mg km^{-1})	Soot-mode emission factor (particles km^{-1})	PNC predicted by CTAG model at 0.45 m (1-400 nm) (particles cm^{-3})	Notes
Case 1	10.6×10^{-7}	240.0	2.6×10^{14}	8.4×10^{7}	Base Case 1, 148 km h^{-1}, 4000 rpm
Case 2	3.5×10^{-7}	24.0	2.1×10^{14}	6.1×10^{6}	Base Case 2, 105 km h^{-1}, 2300 rpm
Case 3	21.2×10^{-7}	240.0	2.6×10^{14}	1.2×10^{9}	Double sulfuric acid flow rate of Case 1
Case 4	5.4×10^{-7}	240.0	2.6×10^{14}	1.3×10^{7}	Half sulfuric acid flow rate of Case 1
Case 5	10.6×10^{-7}	120.0	2.6×10^{14}	8.4×10^{7}	Half OC emission rate of Case 1
Case 6	10.6×10^{-7}	480.0	2.6×10^{14}	8.3×10^{7}	Double OC emission rate of Case 1
Case 7	10.6×10^{-7}	240.0	1.3×10^{14}	1.3×10^{8}	Half soot-mode emission rate of Case 1
Case 8	10.6×10^{-7}	240.0	5.2×10^{14}	4.7×10^{7}	Double soot-mode emission rate of Case 1
Case 9*	5.4×10^{-7}	120.0	1.3×10^{14}	7.3×10^{6}	Advanced technology of Case 1*
Case 10	10.6×10^{-7}	240.0	2.6×10^{14}	3.5×10^{8}	Nucleation only of Case 1
Case 11	10.6×10^{-7}	240.0	2.6×10^{14}	3.3×10^{8}	Nucleation + Coagulation of Case 1
Case 12	10.6×10^{-7}	240.0	2.6×10^{14}	8.8×10^{7}	Nucleation + Condensation of Case 1

* Half sulfuric acid flow rate, half OC emission rate and half soot-mode emission factor

Figure 4.6b shows the dependence of PSDs on the OC concentration, which is related to the fuel type, engine, and the effectiveness of oxidation catalyst. The decrease in the OC emission rate can be achieved by more complete combustion or a more effective oxidation catalyst, and vice versa. It can be seen that the PSD is very sensitive to the OC concentration, since OC dominates the growth of particles through the condensation process. Compared to Case 1, Case 5 with half OC emission rate sees separated nucleation mode and soot-mode, suggesting that the condensable OC in Case 5 is not in a sufficient quantity to grow particles to grow into a larger size. As a result, the nucleation mode is narrow, and the peak number concentration is large. While for Case 6, with abundant OC emission, the nucleation mode has grown rapidly and mixed with the soot-mode. Therefore, the nucleation mode is more spread out and has the lowest peak number concentration among the three cases.

Case 7 and 8 in Figure 4.6c illustrate the influence of soot-mode particle concentrations on the PSDs. Due to the larger size (compared with nucleation mode), soot-mode particles provide a strong condensational sink for sulfuric acid and OC concentrations. In Figure 4.6c, we can see that with half soot-mode emission rate, PNC increases to 1.3×10^8 particles cm^{-3}, which is much higher than Case 1 (8.4×10^7 particles cm^{-3}), showing that with decreased soot-mode particle concentration, the nucleation event is enhanced. On the other hand, with doubled soot-mode emission rate, PNC decreases to 4.7×10^7 particles cm^{-3}, which is about 56% of Case 1.

Based on the sensitivity analysis in sulfuric acid, OC and soot-mode particle concentrations, Case 9 is designed to be indicative of the effects of advanced emission control technology on PSDs (Figure 4.6d). Half sulfuric acid flow rate is selected considering two competing effects on sulfuric acid concentration in the exhaust of advanced diesel vehicles: low FSC, which will reduce sulfuric acid concentration, and high cr due to the aftertreatment devices, which will increase sulfuric acid concentration. Half OC emission rate and half soot-mode emission factor are assumed if the effectiveness of oxidation catalyst converter is enhanced or the diesel particulate filter (DPF) is installed. Compared with Case 1, the simulation result of Case 9 shows a large decrease in PNC, which is 7.3×10^6 particles cm^{-3} and about 8.7% of Case 1 (Figure 4.6d). This is attributed to both the decrease in nucleation mode, which is the dominant reason, and the soot-mode.

Cases 10 to 12 compare the relative importance of each aerosol dynamics process (Figure 4.6e). In Case 10, only the nucleation process is incorporated into the simulation, and since there is no condensable sink for sulfuric acid in the exhaust, the

nucleation has been strengthened tremendously, causing PNC, 3.5×10^8 particles cm^{-3} to be the largest among all the cases. Since there is no condensation and coagulation process, there is no growth for the nucleated particles, and the nucleation mode is limited to about 3 nm. In Case 11, nucleation and coagulation processes are considered. As with Case 10, the nucleation mode is large, and PNC is 3.3×10^8 particles cm^{-3}, which is a 6% of decrease when compared to Case 10. Meanwhile, the shape of PSD also shows little change. Both of above suggests that coagulation process plays a small role in determining PNC and PSD due to its large timescale (Zhang and Wexler, 2004). It also shows the importance of condensation process in aerosol dynamics, which has been validated in Case 12, in which nucleation and condensation process have been considered. PNC is 8.8×10^7 particles cm^{-3}, which is close to the result of Case 1, where the coagulation process is accountable for the 4% difference in PNC between the two cases.

4.4 Conclusion

This chapter describes the overall framework of the CTAG model, its individual components, and coupling of transport and transformation. Then it presents the validations of CTAG in simulating vehicle-induced turbulence and aerosol dynamics in diluting diesel plumes. For the diesel plume simulations, we also investigate the sensitivities of sulfuric acid concentrations, concentrations of organic compounds and soot-mode particles, and individual aerosol processes. We show that the dynamics of exhaust plumes are highly sensitive to vehicle-induced turbulence, sulfuric acid induced nucleation, and condensation of organic compounds. Therefore, ignoring any

of these processes will lead to misrepresentations in the environmental impacts of particulate emissions. Furthermore, constraining the uncertainties in exhaust sulfuric acid concentrations and the volatility of emitted organic compounds by measurements will help improve the capability of predicting particle size distributions in diluting exhaust plumes.

CHAPTER 5

MODELING MULTI-SCALE AEROSOL DYNAMICS AND MICRO-ENVIRONMENTAL AIR QUALITY NEAR A LARGE HIGHWAY INTERSECTION USING THE CTAG MODEL*

Abstract

This paper presents a new methodology, referred to as the multi-scale structure, to integrate the "tailpipe-to-road" (i.e., on-road domain) and "road-to-ambient" (i.e., near-road domain) simulations for elucidating the environmental impacts of exhaust particles from traffic sources. The multi-scale structure is implemented in the CTAG model to generate process-based on-road emissions of ultrafine particles (UFPs) and to characterize the impacts of traffic-related emissions on micro-environmental air quality near a highway intersection in Rochester, NY. The performance of CTAG, evaluated against with the field measurements, shows adequate agreement in capturing the dispersion of carbon monoxide (CO) and number concentrations of UFPs in the micro-environment. As a proof-of-concept case study, we also apply CTAG to separate the relative impacts of the shutdown of a large coal-fired power plant (CFPP) and the adoption of the ultra-low-sulfur diesel (ULSD) on UFP concentrations in the intersection micro-environment. Although CTAG is still computationally expensive compared to the widely-used parametric dispersion models for operationally purpose,

*Wang, Y., Nguyen, M. T., Steffens, J. T., Tong, Z., Wang, Y., Hopke, P. K., Zhang, K. M. Modeling multi-scale aerosol dynamics and micro-environmental air quality near a large highway intersection using the CTAG model. Science of the Total Environment. In revision.

it has the potential to improve the parametric dispersion models to resolve complex environments, e.g., by incorporating road-induced turbulence.

5.1 Introduction

There is a growing number of people living or spending substantial time within 500 m from the highways and major roads, being exposed to the traffic-related pollutants, e.g., ultrafine particles (UFPs), CO and NOx (HEI, 2010). Health studies show elevated risk for development of asthma and reduced lung function in children who live near major highways (Kunzli et al., 2003; Brugge et al., 2007). In a cohort of 5000 adults followed up for 8 years, cardiopulmonary mortality was found to be associated with living near a major road (Hoek et al., 2002). Therefore, it is important to estimate the spatial and temporal impacts of traffic-related emissions on near-road air quality, which are critical to assessing human exposure. However, there are still significant challenges in modeling near-road air quality.

One of the challenges is associated with the uncertainties in the on-road emission factors of air pollutants, especially for UFPs (Keogh et al., 2009). Besides the soot-mode particles emitted directly from tailpipes, nucleation mode particles are formed during the dilution process of the hot exhaust (Shi and Harrison, 1999; Maricq et al., 1999; Khalek et al., 1999) and are strongly affected by the traffic conditions (e.g., fuel, engine load, etc.) and meteorological conditions (e.g., temperature, relative humidity) (Ronkko et al., 2006; Frank et al., 2007; Kumar et al., 2011; Wang and Zhang, 2012). Measurements have been conducted to capture the on-road emissions of UFPs on the project-level (Ronkko et al., 2006; Fruin et al., 2007; Wehner et al., 2009; Westerdahl

et al., 2009). However, due to the complexity and variety in on-road traffic-related activities and effects of aerosol dynamics on the evolution of UFPs, it is difficult to provide accurate emission factors of UFPs based on a small set of measurements.

Another challenge arises from the effects of urban environments on the dispersion of air pollutants. Typical in urban or suburban areas, roadways are often surrounded by structures such as roadside barriers, buildings, and vegetation. Moreover, roadways may have various configurations. For example, highways may be elevated or depressed, and multiple roadways may form an intersection. The turbulence caused by the roadside structures affect the dispersion of pollutants considerably (Wang and Zhang, 2009; Steffens et al., 2012; Tong et al., 2012). As a result, the presence of roadways and roadside structures leads to the formation of "micro-environments", where significant spatial variations in pollutant concentrations exist. Charactering micro-environmental air quality poses challenges for both monitoring and modeling efforts (Brugge et al., 2007; Isakov et al., 2009).

In this paper, a novel multi-scale structure is created to advance our capability of simulating the evolution of UFPs from vehicular tailpipes to near-road environments. This multi-scale structure is implemented in the Comprehensive Turbulent Aerosol Dynamics and Gas Chemistry (CTAG) model, introduce in Wang and Zhang (2012), to characterize the micro-environmental air quality near a large highway intersection. This paper is organized as follows. First, we briefly describe the studied intersection micro-environment. Then we discuss the implementation of the multi-scale structure in CTAG for the linking between on-road and near-road UFPs simulations in detail. The simulation results of CTAG are evaluated by field measurements. Finally, we use

CTAG to estimate the impacts of emission reductions in improving the near-road air quality due to the shutdown of a coal-fired power plant (CFPP) and the adoption of the ultra-low-sulfur diesel (ULSD).

5.2 Method

5.2.1 The highway intersection micro-environment

Figure 5.1. Location of the highway intersection in the suburban Rochester, NY. The coal-fired power plant is to be introduced in Section 5.3.3.

Our study focuses on a micro-environment surrounding a large highway intersection located in Rochester, NY, shown in Figure 5.1. The highway intersection

consists of two major interstate highways (I-490 and I-590) as well as the NY Route 96 (NY-96). I-490 is a 6-lane highway that runs in the northwest-southeast direction, while the 4-lane I-590 traverses the area in the northeast-southwest direction. Both highways are elevated using embankments and bridges when intersecting with NY-96. We choose this site for several reasons: (1) Residential communities and schools are located surrounding the highway intersection, making near-road air pollution an important issue; (2) the New York State Department of Environmental Conservation (NYSDEC) maintains an air quality monitoring site, shown in Figure 5.1, which is located north of the intersection and ~200 m to the highway. This site provides continuous meteorological and air quality measurement data; (3) there are no other major roadways near the sampling site.

5.2.2 Field measurement

Continuous measurements of CO and UFPs were conducted at the NYSDEC site (Wang et al., 2011a). CO was measured using Non-dispersive Infrared (NDIR) method (TECO Model 48C). A Scanning Mobility Particle Sizer^{TM} (SMPS) was deployed to measure UFPs from 10 to 500 nm. The instruments were mounted at 4 m above the ground. There were also intensive mobile measurements at multiple locations surrounding the highway intersection with a Fast Mobility Particle Sizer^{TM} (FMPS) (Wang et al, 2011a), shown in Figure 5.1. The side-by-side comparison of UFP number concentrations measured using the SMPS and the FMPS was conducted before the intensive measurements. Meteorological data including wind velocity and direction (by Climatronics Sonic Anemometer), temperature and relative humidity (by

Teledyne RH200) was measured at the height of 10 m at NYSDEC site and roadway traffic activity was recorded and analyzed by New York State Department of Transportation (NYSDOT).

5.2.3 Numerical model

5.2.3.1 The CTAG model with the implementation of the multi-scale structure

CTAG is suitable for the study because of its capabilities in resolving the turbulent flow field in complex environments through CFD simulations and capturing transformation of air pollutants through aerosol dynamics (i.e., nucleation, condensation and evaporation, coagulation and deposition). Large-eddy Simulation (LES) model is used to solve the three-dimensional turbulent flow field and dispersion of pollutants affected by VIT, RIT and atmospheric boundary layer turbulence (ABLT). LES model resolves the large-scale energy containing eddies numerically while the small, unresolved eddies are modeled. The filtered Navier-Stokes equations are:

$$\frac{\partial \rho}{\partial t} + \frac{\partial}{\partial x_i}\left(\rho \bar{u}_i\right) = 0 \tag{5.1}$$

$$\frac{\partial}{\partial t}\left(\rho \bar{u}_i\right) + \frac{\partial}{\partial x_j}\left(\rho \bar{u}_i \bar{u}_j\right) = \frac{\partial}{\partial x_j}\left(\mu \frac{\partial \sigma_{ij}}{\partial x_j}\right) - \frac{\partial \bar{p}}{\partial x_i} - \frac{\partial \tau_{ij}}{\partial x_j} \tag{5.2}$$

where σ_{ij} is the stress tensor due to molecular viscosity defined by

$$\sigma_{ij} = \left[\mu\left(\frac{\partial \bar{u}_i}{\partial x_j} + \frac{\partial \bar{u}_j}{\partial x_i}\right)\right] - \frac{2}{3}\mu \frac{\partial \bar{u}_l}{\partial x_l}\delta_{ij} \tag{5.3}$$

and τ_{ij} is the subgrid-scale (SGS) stress defined by

$$\tau_{ij} = \rho\overline{u_i u_j} - \rho\bar{u}_i\bar{u}_j \tag{5.4}$$

The subgrid-scale stress resulting from the filtering operation is unknown and therefore requires modeling. The Smagorinsky eddy viscosity model (Smagorinsky, 1963) is used here to model the SGS stress:

$$\tau_{ij} - \frac{1}{3}\tau_{kk}\delta_{ij} = -2\mu_t\bar{S}_{ij} \tag{5.5}$$

where the eddy diffusivity is modeled by

$$\mu_t = \rho\bar{\Delta}^2\left|\bar{S}\right| \tag{5.6}$$

where $\bar{\Delta}$ is the filter width and $\left|\bar{S}\right|$ is defined by

$$\left|\bar{S}\right| = \sqrt{2\bar{S}_{ij}\bar{S}_{ij}} \tag{5.7}$$

The domain of the studied intersection micro-environment (as illustrated in Figure 5.1) is complex, with moving traffic on elevated highways and roadside structures such as vegetation, and buildings. The capabilities of CTAG in simulating aerosol dynamics at individual tailpipe level and resolving the effects of roadway and roadside structures on turbulent mixing and pollutant dispersion have been evaluated in our previous studies. The effect of VIT and RIT (e.g., highway embankment) on the turbulent mixing was studied in Wang and Zhang (2009). Then Steffens et al. (2012) explored the effects of a vegetation barrier on the particle size distributions in a near-road environment. Tong et al. (2012) modeled the spatial variation of black carbon particles in an urban highway-building environment. Wang and Zhang (2012) captured the turbulence and aerosol dynamics in the diluting exhaust plume of an individual vehicle. These earlier studies have provided a solid foundation for the study of

modeling multi-scale aerosol dynamics and micro-environmental air quality near a large highway intersection in the current study.

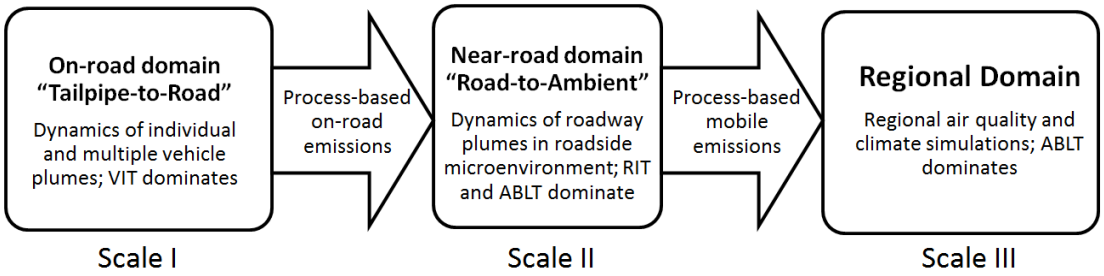

Figure 5.2. The multi-scale structure for the roadway air quality study, implemented in CTAG.

In this paper, a novel multi-scale structure is implemented in CTAG (Figure 5.2) based upon the mechanistic roadway air quality modeling framework proposed by Zhang and Wexler (2004). CTAG resolves the plume dynamics behind individual vehicles and the interactions of multiple plumes in the on-road domain (Scale I), as an emission model. The processed on-road emissions will serve as inputs to the near-road domain simulations (Scale II), where CTAG resolves the dynamics of roadway plumes in the roadside micro-environment, as a dispersion model. The processed roadway plume profiles on the near-road domain can be used as inputs to regional-scale air quality simulations (Scale III). The application of the multi-scale structure in this intersection micro-environment is discussed as follows.

On-road domain for "tailpipe-to-road" scale

On-road domain is created based on the traffic condition (e.g., traffic volume, speed and vehicle types). Using I-490 as an example, the on-road domain in Figure 5.3 has a size of 350 m (x axis) by 60 m (z axis) in the horizontal and 50 m in the vertical

direction (y axis). It contains two zones: the on-road background zone and emission profile zone, with the same traffic density and percentage, shown in Figure 5.3. Each zone has a size of 160 m by 28 m in the horizontal and 3 m in vertical, according to the percentage of heavy-duty truck, as discussed in Wang et al. (2011b). Within the two zones, different types of vehicles, i.e. gasoline passenger cars and heavy-duty diesel trucks, are represented by approximate vehicle geometries. The gaseous and primary particulate pollutants are emitted directly from the exhaust pipes. Vehicles are considered to be stationary. The inlet wind velocity is taken as the vector sum of the ambient wind velocity and the opposite of the vehicle speed. A fully developed vertical profile of the inlet wind flow is imposed on the faces of the on-road domain to simulate the atmospheric boundary layer under different stability classes. The background zone is used to provide the on-road background UFP concentration to take into account the effects of aged exhaust from on-road vehicles. Using on-road background concentrations is important for simulating on-road aerosol dynamics because it is the on-road background air, rather than the ambient air, that dilutes the exhaust during the "tailpipe-to-road" stage. The on-road domain needs to be long enough in order to account for the on-road background UFP concentration. The face on the downwind side of emission profile zone (the side with oblique crossed lines in on-road domain in Figure 5.3) is used to acquire the curbside concentrations of the UFPs, referred to as process-based UFP concentration because exhaust particles have undergone dilution and aerosol dynamical processes. The on-road turbulence data, i.e., the volume-averaged VIT and turbulent dissipation rate can also be acquired from the emission profile zone, which are used in the emission zones above highways in near-

road domain. The on-road domain is divided into 3 million unstructured cells and the finest mesh resolution is created for the near-vehicle region, increasing exponentially in x-, y-, z-directions towards the outer boundaries of the on-road domain. Mesh independence study (the domain meshed with 1.5 million and 4.5 million cells) has been conducted to make sure that the grid resolution to be fine enough for the accuracy of the simulation result. The faces of the four sides of the on-road domain are defined as velocity inlets or outflows, depending on the wind direction. A symmetric boundary is set up at the top plane of the domain to represent no shear stress condition.

In summary, the primary advantages of multi-scale structure in deriving processed, on-road emission profiles are 1) that we generate, instead of assuming, on-road background size-resolved UFP concentrations based on properties of individual plumes, and 2) that aerosol dynamics (or chemical reactions) are simulated to account for plume transformation.

Near-road domain for "road-to-ambient" scale

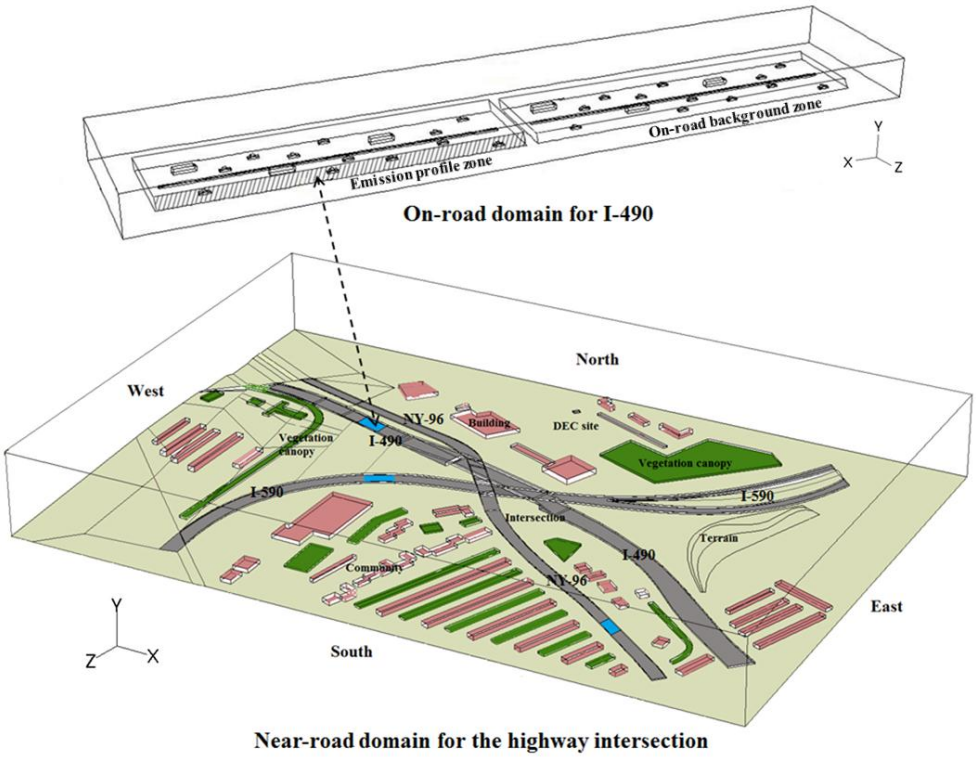

Figure 5.3. The sketch of the coupling between the on-road and near-road domains for micro-environmental air quality study, i.e., the multi-scale structure in CTAG

The schematic diagram of the near-road domain, i.e., the micro-environment near the highway intersection, is also shown in Figure 5.3. With the geographic information systems (GIS) software (e.g., Google Earth), the complex modeling domain can be readily constructed, and key features, including the highway intersection (in grey), buildings (in light red), vegetation canopy (in green), and terrain (in light yellow) can be incorporated in great details. The emission profile zones are highlighted as the straight sections in blue color. The domain has a size of 1364-160-943 m (x-y-z) and is divided into 6 million unstructured cells. Mesh independence study (the domain meshed with 3 million and 9 million cells) has been conducted to make sure that the

grid resolution to be fine enough for the accuracy of the simulation result (difference within 7% for the simulation results of the dispersion of CO). While the individual vehicular exhaust emissions are resolved in the on-road simulations, it is computationally expensive to do so for the near-road simulations. Therefore, volume-averaged emission rates for the highways are employed in the near-road domain. Emission zones are built right above the highway surfaces, with the same height and width as the emission profile zone in on-road domain for each highway, respectively. The size-resolved, process-based, volume emission rates of UFPs are acquired by equating the UFP concentrations between the on-road and near-road domains for each roadway under the same wind speed and direction. Specifically, the volume emission rates are set in the way that the UFP concentrations at the downwind surfaces of those blue sections in near-road domain are the same as the UFP concentrations at the downwind surfaces of emission profile zone in on-road domain. Then the volume emission rates are applied in the whole emission zone for each roadway in near-road domain. In addition, the on-road turbulence data are taken directly from on-road simulations to represent the effects of VIT for the near-road simulations. The faces of the four sides of the near-road domain are defined as velocity inlets or outflows, depending on the wind direction. For the velocity inlet boundary, a fully developed vertical profile of the inlet wind flow is imposed to simulate the atmospheric boundary layer under different stability classes. A symmetric boundary condition is set at the top plane of the domain. A no-slip condition is imposed to the surfaces of buildings and ground, while appropriate roughness is selected for the ground for different seasons.

In summary, the proposed method allows us to link individual plume properties with near-road air quality, and its application will be discussed in Section 5.3. A unique capability of the multi-scale structure is to capture how fuel properties, traffic and meteorological conditions affect particle size and composition distributions in the diluting plumes. Taken as inputs to the near-road simulations, the processed on-road emissions greatly enhance the modeling capability in elucidating how near-road air quality is impacted by on-road conditions. Combining on-road and near-road simulations, CTAG becomes a "plume-in-grid" model for mobile emissions. The processed emission profiles can improve regional air quality and climate predictions accordingly. Currently the practical connection between near-road domain and regional domain is under development, but the multi-scale structure enables CTAG to serve as an advanced analytical tool for a variety of applications.

5.2.4 Model implementation

We select 17 scenarios from 2005 to 2010, as summarized in Table 5.1. Each scenario, 1 to 3 hours in duration, is chosen due to its relatively constant wind velocity, wind direction and traffic volume based on hourly data, provided by NYSDEC and NYSDOT. Therefore, these scenarios can provide the time-constant boundary conditions for the unsteady-state simulation of the evolution of UFPs, as discussed in Wang and Zhang (2012). Meanwhile, they represent a wide range of meteorological and traffic conditions: 1) Seasons, reflecting by the varying temperatures (ranges from 2.7 to 33.9 ℃); 2) Wind velocity (from 1.3 to 5.2 m s^{-1}); 3) Wind direction, ranging from northeast (30.2°) to northwest (340.2°); 4) Traffic

volume (from morning peak to evening peak). The average percentage of heavy-duty vehicles on I-490 (~21%) is greater than I-590 (~14%). There is no vehicle class count data available for NY-96. The average fraction of heavy-duty vehicles of I-490 and I-590 is used to represent NY-96. Mean vehicle speed varies from 25 to 28 m s^{-1} for I-490 and I-590, depending on the traffic conditions. The averaged vehicle speed is estimated as 15 m s^{-1} for NY-96.

Table 5.1 Meteorological parameters and road conditions for selected scenarios from 2005 to 2010

Scenarios		Wind Velocity	Wind Direction[b]	Temperature	Relative humidity	Stability Class	Traffic Volume (vehicle h^{-1})		
		(m s^{-1})	(°)	(℃)	(%)		I-490	I-590	NY-96
06/09/2005	10:00-12:00	2.5	207.1	32.8	39.5	Slightly Unstable	5151	6315	505
07/23/2005	12:00-15:00	1.9	118.2	33.9	27.1	Unstable	4213	6216	484
03/21/2007	12:00-14:00	2.7	141.0	7.7	27.5	Slightly Unstable	4737	5270	591
07/14/2007	11:00-14:00	3.0	205.3	24.7	36.2	Slightly Unstable	4805	5661	538
10/08/2008	10:00-12:00	1.6	171.6	19.6	53.5	Slightly Unstable	4661	5403	542
12/03/2008	11:00-14:00	3.5	207.1	6.1	43.5	Neutral	4534	5012	578
01/13/2009	12:00-14:00	4.8	219.4	2.7	65.3	Neutral	4834	5317	610
08/12/2009[a]	07:00-09:00	1.3	340.2	23.9	61.0	Slightly Unstable	4250	5924	633
08/14/2009[a]	17:00-19:00	1.4	30.2	31.5	45.3	Unstable	2077	2445	254
06/09/2010	10:00-13:00	2.8	155.5	13.4	73.1	Neutral	5082	5498	601
09/07/2010	12:00-15:00	2.7	221.2	31.7	37.8	Slightly Unstable	5120	6225	632

[a] Include NYSDEC site measurement and intensive measurements.
[b] Wind direction: 0 °corresponding to wind from north, 90 °corresponding to wind from east, 180 °corresponding to wind from south, 270 °corresponding to wind from west.

The emission rates of CO shown in Table 5.1 are generated from MOBILE6.2 by NYSDOT for project-level micro-scale analysis in Rochester area: the vehicle activities (e.g., vehicle speed) were acquired through on-site measurements near the highway intersection and the vehicle technological parameters (e.g., model and year, engine type, control emission systems) are within the vehicle database for New York State (NYSDOT, 2008).

UFPs are represented by 11 size bins with fixed-boundary, moving-center sectional structure ranging from 1 to 500 nm. The level of sulfuric acid at the exit of

the tailpipe plays an important role in determining the formation of UFPs and it depends on the fuel sulfur content (FSC) and the SO_2-to-SO_3 conversion rate (cr). For diesel fuel, there was a nationwide transition starting in late 2006 from low-sulfur diesel (FSC ~ 350 ppm or above) to ultra-low-sulfur diesel (ULSD with FSC ~ 15 ppm or less) due to the highway diesel fuel sulfur program (USEPA, 2000). FSC in gasoline also decreased in 2006 from 60 ppm to 30 ppm (USEPA, 1999). cr is assumed to be 3% for diesel engines and 1% for gasoline engines (Shi and Harrison, 1999; Johnson et al, 2009). Organic carbon (OC) in the exhaust is responsible for the growth of nuclei and pre-existing particles. They are emitted directly from the tailpipe mainly as gas-phase and can be separated into volatile, semi-volatile and low-volatile groups. Among these groups, volatile OC (VOC) is considered to have little impact on particle growth due to their large volatilities. The semi-volatile and low-volatile groups account for 20-40% of the total mass emissions (Schauer et al. 1999). Then the emission factors for semi-volatile and low-volatile OC are estimated based on those of VOC generated from MOBILE6.2 and shown in Table 5.2. The emission factors of primary soot-mode particles for gasoline and diesel engines are shown in Table 5.2 (Maricq et al. 2002; Frank et al. 2007). The ambient CO and UFPs concentrations are estimated from multiple intensive mobile measurements at upwind locations, i.e., not affected by the highway intersection.

Table 5.2 Emission factors for OC, FSC and soot-mode particles by year

	Gasoline semi-volatile and low-volatile OC (mg/km)[a]	Diesel semi-volatile and low-volatile OC (mg/km)[a]	Gasoline FSC (ppm)	Diesel FSC (ppm)	Gasoline soot-mode particle (particles km^{-1})[a]	Diesel soot-mode particle (particles km^{-1})[a]
2005	60.0	64.4	60	350	3.5×10^{11}	9.0×10^{13}
2007	48.0	51.5	30	15	3.0×10^{11}	7.7×10^{13}
2008	43.3	46.5	30	15	2.8×10^{11}	7.4×10^{13}

2009	37.0	40.5	30	15	2.7×10^{11}	7.1×10^{13}
2010	34.6	37.2	30	15	2.6×10^{11}	6.8×10^{13}

[a] Annual change is estimated based on the yearly change of VOC and PM (Particulate Matter) predicted from MOBILE6.2.

5.3 Results and discussion

5.3.1 Evaluation of CTAG for CO in the micro-environment

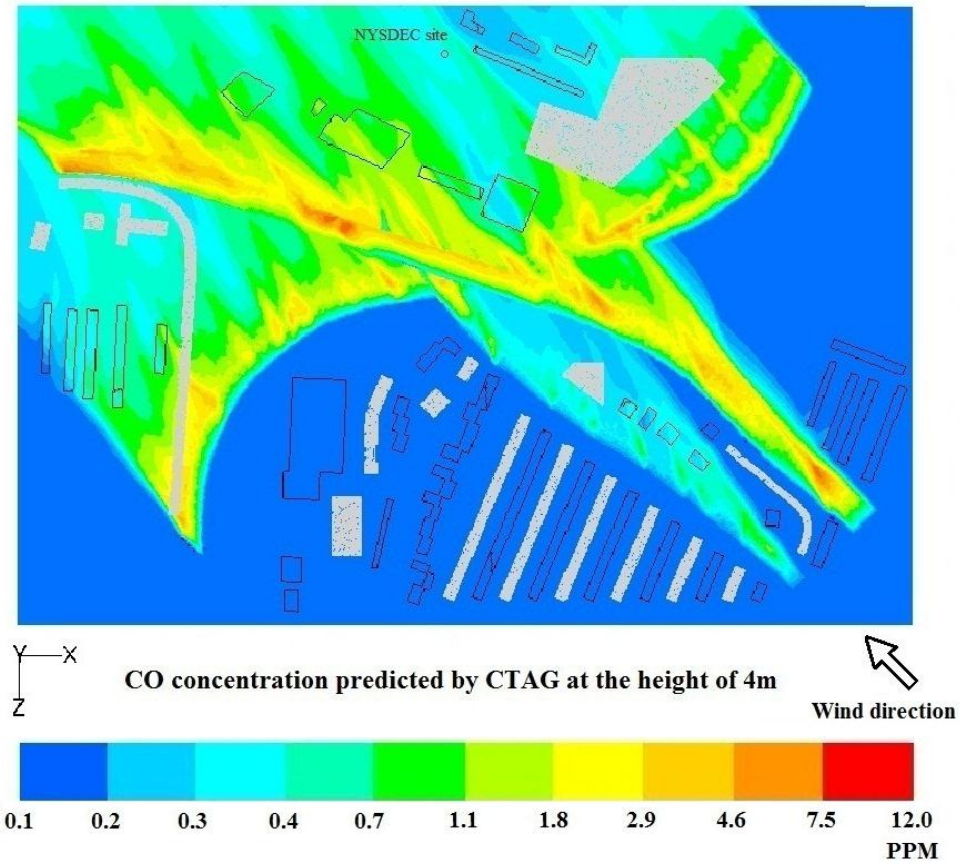

Figure 5.4. Dispersion of CO in the near-road domain at height of 4 m (the height of CO measurement equipment in the NYSDEC site) for 03/21/2007 (12:00-14:00) scenario. The wind direction is ~141 °. The light grey blocks in the figure of CTAG represent the vegetation canopy without leaves in winter

In the near-road environment, CO behaves as a non-reactive gas tracer and its dispersion is dominated by turbulence. Therefore, it can provide us the basic judgment for the pollutant dispersion model, and serves as an indicator for the turbulent flow

field. The contour of CO concentration in the near-road domain for 03/21/2007 (12:00-14:00) scenario is shown in Figure 5.4 as an example. It shows a wide range of variations, which are due to the strong wake effects caused by the roadway configurations and near-road buildings. Both VIT and RIT play important roles in mixing the tailpipe exhaust with the ambient air. VIT originates from the interaction between moving vehicles and ambient air. As shown in Figure 5.5(a), the movement of on-road vehicles results in a significant increase in VIT, which remains at a high level surrounding the vehicles and in the near wake of the vehicles. But due to dissipation of turbulence (Rao et al. 2002), VIT decays rapidly with the increasing distance away from the vehicles. VIT is strongly related to vehicle types and speed. The heavy-duty diesel trucks induce more turbulence than passenger cars due to its size and structure. RIT considered in CTAG includes the roadway configuration and near-road buildings. As shown in Figure 5.5(b), the embankment of I-490 acts as a topographic obstacle which causes a form drag and produces turbulence to compensate for the deformation of the flow field when wind flows over it. A recirculation cavity is created downwind of the embankment and turbulence increases due to the wake effect. The increased turbulence can prompt the dispersion of the pollutants, especially in the vertical direction (Wang and Zhang, 2009).

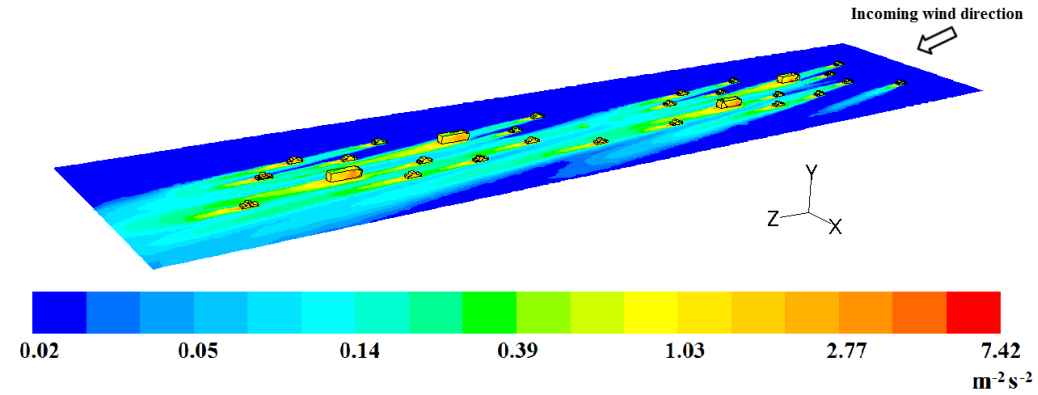

(a)

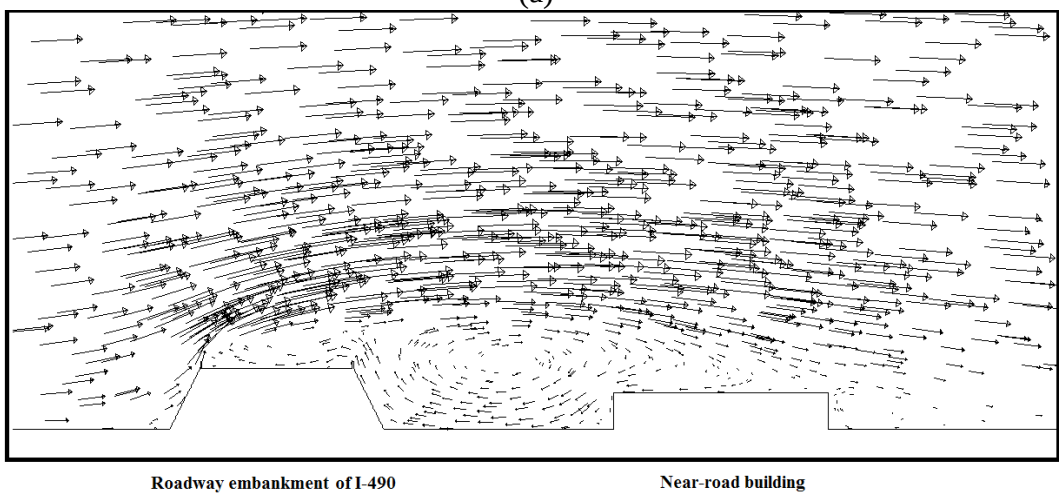

(b)

Figure 5.5. (a) Vehicle-induced turbulence (VIT) in the on-road domain (b) Wind velocity vector showing the effect of roadway structure and surrounding building on the flow field in near-road domain

The comparisons between predicted and measured CO concentrations and the evaluation statistics for CTAG are illustrated in Table 5.3. With small MNE (<19%) and MFE (12%), it has been demonstrated to have a good capability of capturing the dispersion of CO and the turbulent flow field. This is in accordance with the simulation results in Wang and Zhang (2009), where CTAG captured the horizontal and vertical gradients of CO and wind velocity near a major interstate (I-405) located

on the embankment. A good prediction of the near-road turbulent flow field can greatly diminish the potential uncertainties in the simulations of aerosol dynamics.

Table 5.3 Comparisons of pollutant concentrations between models and measurement data

Scenarios	Measured CO (ppm)	CO by CTAG (ppm)	Bias[b]	CO by the standard CFD (ppm)	Bias[b]	UFPs by measurement (particles cm^{-3}) (10 - 500 nm)[c]	UFPs predicted by CTAG (particles cm^{-3}) (10 - 500 nm)	Bias[b]
06/09/2005	0.53	0.76	43.4%	1.17	120.8%	2.69×10^4	4.21×10^4	56.5%
07/23/2005	0.41	0.53	29.3%	0.83	102.4%	1.33×10^4	1.74×10^4	30.8%
03/21/2007	0.35	0.41	17.1%	0.62	77.1%	1.03×10^4	1.60×10^4	55.3%
07/14/2007	0.42	0.53	26.2%	0.81	92.9%	6.86×10^3	9.77×10^3	42.4%
10/08/2008	0.49	0.56	14.3%	0.88	79.6%	5.12×10^3	7.55×10^3	47.5%
12/03/2008	0.56	0.62	10.7%	0.76	35.7%	5.37×10^3	8.42×10^3	56.8%
01/13/2009	0.43	0.38	-11.6%	0.52	20.9%	8.13×10^3	7.13×10^3	-12.3%
06/09/2010	0.35	0.32	-8.6%	0.46	31.4%	6.01×10^3	7.75×10^3	29.0%
09/07/2010	0.36	0.41	13.9%	0.49	36.1%	4.12×10^3	5.18×10^3	25.7%
MNE[a]	-	-	19.5%	-	66.3%	-	-	39.6%
MNB[a]	-	-	15.0%	-	66.3%	-	-	36.9%
MFE[a]	-	-	12.1%	-	34.8%	-	-	23.0%
MFB[a]	-	-	9.0%	-	34.8%	-	-	21.1%

[a] MNE: mean normalized error; MNB: mean normalized error; MFE: mean fractional error; MFB: mean fractional error. Error is a measure of the extent that the model deviates from the measurements and is always positive. Bias is a measure of the tendency of the model to over or under predict the measurements and can be positive or negative. MNB, MNE, MFB and MFE are described in the Supporting Information.
[b] Normalized by measurement.
[c] Measurement range of SMPS for UFPs.

5.3.2 Evaluation of multi-scale aerosol dynamics simulations in the micro-environment

Evolution of UFPs in the on-road domain and near-road domain for 09/07/2010 (12:00-15:00) scenario is shown in Figure 5.6 as an example to capture the 'tailpipe-

to-road' and 'road-to-ambient' stages of the multi-scale structure for roadway air quality.

- ***On-road domain for "tailpipe-to-road" scale***

It can be seen in Figure 5.6 that the exhaust plume in the wake of each vehicle (i.e., behind the rear of the passenger car or above the top of the heavy-duty diesel truck) is resolved in the on-road domain. Strongly affected by VIT, the exhaust plume spreads out quickly and the dilution ratio can reach upwards of 1000 in the few seconds before it reaches to the curbside of the roadway, which is in agreement with previous field studies and laboratory experiments (Kittelson et al., 1988; Shi et al., 2002).

Nucleation takes place in the near-wake region, where the fresh exhaust is diluted by the ambient air. The formation of new particles significantly increases the total UFP concentrations generated by traffic. The exhaust plumes from multiple vehicles are mixed together and aerosol dynamics process continues during the mixing process. UFP concentrations are sensitive to the dilution condition and the level of sulfuric acid, OC and primary soot-mode particles, and small changes might result in orders of magnitude difference (Ronkko et al., 2006; Wang and Zhang, 2012). Meanwhile, it should be noted that meteorological conditions (e.g., ambient temperature, relative humidity and wind velocity) might also affect the formation of new particles and the on-road UFP concentrations (Vehkamaki et al., 2003; Ronkko et al., 2006). Therefore, sensitivity studies are conducted using the CTAG model and scenarios of 07/23/2005 (12:00-15:00) and 02/18/2009 (11:00-12:00) are used as examples. As illustrated in Table 5.4, the on-road UFP concentrations are sensitive to the ambient temperature

and small variations in temperature (a 5 ℃ difference) can result in up to 59% change in UFP concentrations. Relative humidity also plays a crucial role in determining the on-road UPF concentrations. With a higher relative humidity (a 5% increase), the UFP concentrations can increase in a range from 12.8% to 25.5%. The wind velocity also affects on-road UFP concentrations. With doubled wind velocity, UFP concentrations decrease 3.6~4.2%, while with half wind velocity, UFP concentrations increase 2.5~3.7%. Wind velocity shows a relatively small impact on UFPs concentrations than ambient temperature and relative humidity, since instead of altering the nucleation rate of UFPs as ambient temperature and relative humidity, wind velocity changes the rate that transports the pollutants from vehicular tailpipes to roadway curbside. Higher wind velocity dilutes the pollutants faster. Therefore, lower temperature, higher relative humidity and lower wind velocity can lead to a higher on-road UFP concentration and vice versa.

Table 5.4 Sensitivity studies investigating the effect of meteorology conditions on the on-road *UFPs* concentrations (I-490 is taken as an example)

Scenario	Ambient temperature (℃)	UFPs predicted by CTAG (particles cm^{-3}) (1 - 500 nm)	Bias[b]	Scenario	Ambient temperature (℃)	UFPs predicted by CTAG (particles cm^{-3}) (1 - 500 nm)	Bias[b]
07/23/2005 (12:00-15:00)	28.9	3.08×10^5	59.0%	02/18/2009 (11:00-12:00)	-2.2	1.55×10^5	38.4%
	33.9[a]	1.94×10^5	--		2.8[a]	1.12×10^5	--
	38.9	8.74×10^4	-54.9%		7.8	6.43×10^4	-42.8%
	Relative humidity (%)				Relative humidity (%)		
07/23/2005 (12:00-15:00)	22.1	1.48×10^5	-23.6%	02/18/2009 (11:00-12:00)	42.0	1.05×10^5	-10.9%
	27.1[a]	1.94×10^5	--		47.0[a]	1.12×10^5	--
	32.1	2.43×10^5	25.5%		52.0	1.20×10^5	12.8%
	Wind velocity ($m\ s^{-1}$)				Wind velocity ($m\ s^{-1}$)		
07/23/2005 (12:00-	1.0	1.99×10^5	2.5%	02/18/2009 (11:00-	1.6	1.16×10^5	3.7%
	1.9[a]	1.94×10^5	--		3.1[a]	1.12×10^5	--

15:00)	3.8	1.87×10^5	-3.6%	12:00)	6.2	1.07×10^5	-4.2%

[a] Base case of each scenario, as shown in Table 5.1.
[b] Deviation from Base case.

In summary, simulating the vehicular UFPs emissions within the on-road domain of the multi-scale structure can be a crucial methodology, since UFPs emissions cannot be obtained directly from the widely-used emission models (e.g., MOBILE6.2, etc) and field measurements are not always applicable (due to the cost and safety issues, etc). When reliable data of sulfuric acid, OC and soot-mode particles are provided, the generation of UFPs can be obtained under various meteorological conditions. This methodology is more reliable, since sulfuric acid, OC and soot-mode particles mainly rely on the traffic activities instead of the meteorological conditions, e.g., the emission of soot-mode particle remains constant under fixed engine operation conditions (Ronkko et al., 2006). With the multi-scale structure, CTAG becomes an emission model and can produce process-based on-road emission factors of UFPs, which consider the effect of turbulence, tailpipe emission and weather conditions for the aerosol dynamics process.

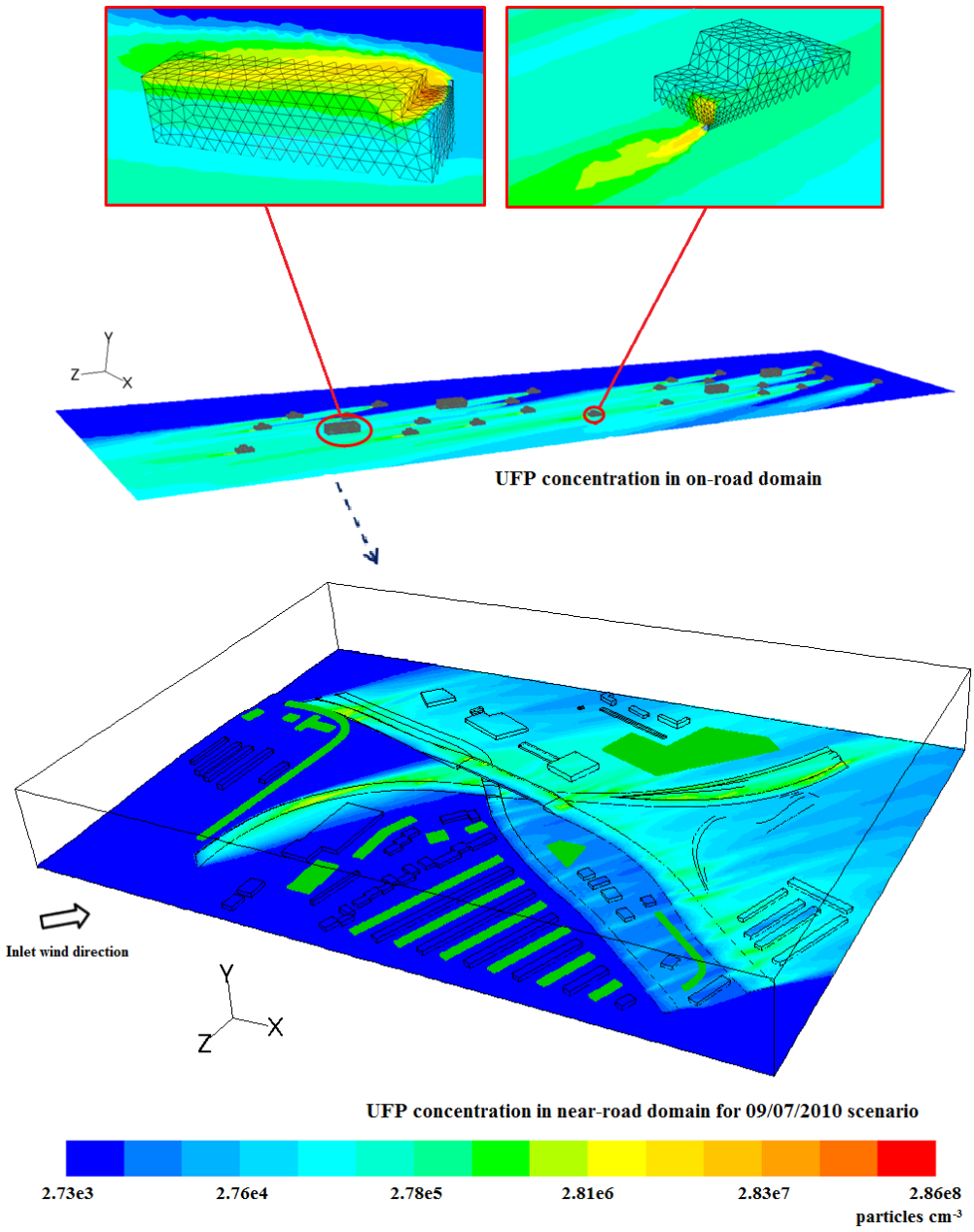

Figure 5.6. Time-averaged distributions of UFPs (1-500 nm) simulated by CTAG with the implementation of multi-scale structure: in the wake of individual vehicles, in on-road domain and in near-road domain for 09/07/2010 (12:00-15:00) scenario. The wind direction is ~221.2 °

- ***Near-road domain for "road-to-ambient" scale***

The evolution of UFPs in the near-road domain is modeled with the emission rates of UFPs provided by the on-road domain. The contour of UFP concentrations in the near-road domain for 09/07/2010 (12:00-15:00) scenario is shown in Figure 5.6. It can be seen that due to the emissions from the highway intersection, UFP concentrations in the downwind side are higher than the upwind side. Compared with the strong dilution in the on-road domain due to VIT, the dilution of UFPs in the near-road domain is much smaller (~ 10 or less). The impact of the highway intersection on the air quality varies considerably with the downwind distances (e.g., on the curbside of the highway or a few hundred downwind).

As illustrated in Table 5.3, there is a yearly trend indicating that the concentrations of both CO and UFPs have decreased from 2005 to 2010, due to the emission control technologies, e.g., decreasing the fuel sulfur content and installing after-treatment devices. The better air quality is beneficial to the people living or working near this highway intersection. In addition, scenarios with the wind blows from north are specially studied due to the presence of a residential community south of the intersection. As shown in Figure 5.7, it can be seen that the air quality in the residential community is strongly affected by the highway intersection, especially for those houses next to the intersection, of which the level of UFP concentration can be up to 3.66×10^4 (particles cm^{-3}), much higher than the ambient background UFP concentration, which is 3.2×10^3 (particles cm^{-3}). Areas of high UFP concentrations can be found on I-590, part of which is parallel to the ambient wind. The parallel wind can lead to the accumulation of tailpipe emissions on the highway. Another area of

high UFP concentrations can be found at the place where the three highways intersect, due to the large traffic volume. Intensive measurements were conducted in multiple locations surrounding the intersections (e.g., parking lot near schools and residential areas), and the 08/14/2009 (17:00-19:00) scenario is shown as an example in Figure 5.7. The comparisons between the predicted and measured UFP concentrations are summarized in Table 5.5. Meanwhile, the comparisons between predicted and measured UFP concentrations at the NYSDEC site for other 15 scenarios and the evaluation statistics for CTAG are shown in Table 5.3. The MNE (34.9%) and MFE (20.8%) of the predictions of UFP concentrations are higher than those of CO prediction. However, when considering the uncertainties in the input parameters (e.g., the level of sulfuric acid exited from the tailpipe, discussed in Section 5.3.4), the performance of CTAG is adequate in capturing the evolution of UFPs in the micro-environment.

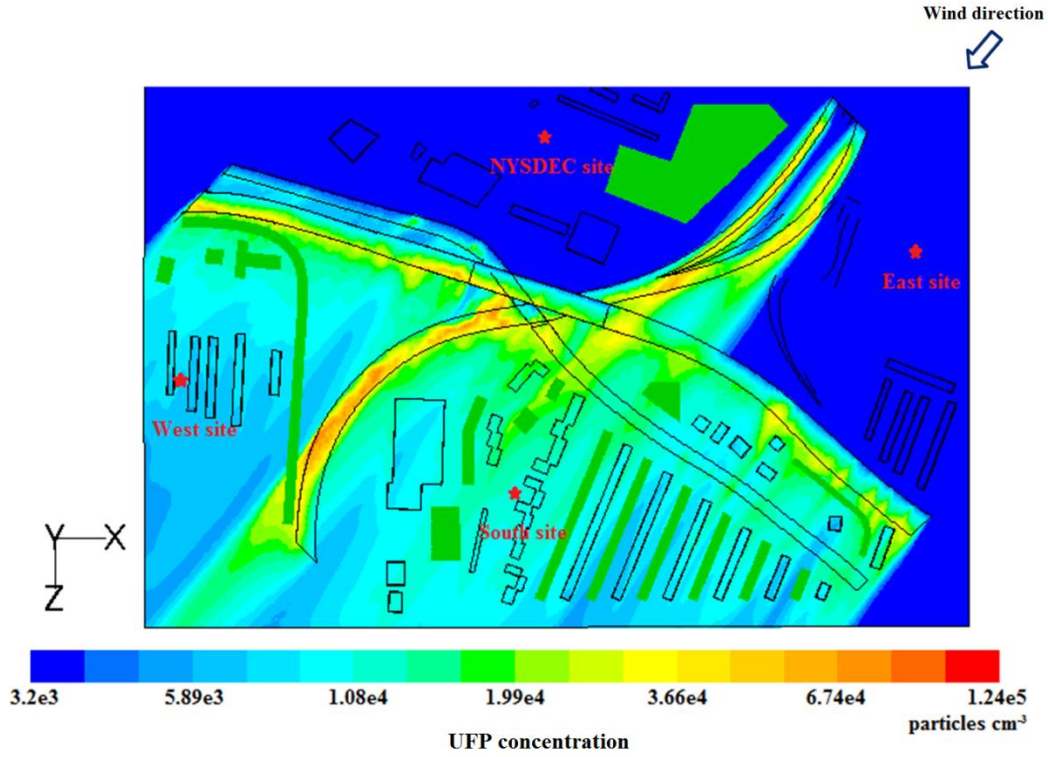

Figure 5.7. Time-averaged distribution of UFPs (1-500 nm) for 08/14/2009 (17:00-19:00) scenario. The residential community is located in the south of the intersection. Red stars denote the intensive measurement sites near the highway intersection. The wind direction is ~30.2 °

Table 5.5 Comparison of UFP concentrations between CTAG and measurements at multiple locations surrounding the highway intersection

Location	8/12/2009 scenario			8/14/2009 scenario		
	UFPs by measurement[b] (10 - 500 nm)	UFPs by CTAG[b] (10 - 500 nm)	Bias[c]	UFPs by measurement[b] (10 - 500 nm)	UFPs by CTAG[b] (10 - 500 nm)	Bias[c]
East site	1.1×10^4	8.6×10^3	-22.8%	3.2×10^{3a}	3.2×10^3	--
South site	1.2×10^4	1.7×10^4	38.7%	9.3×10^3	1.2×10^4	29.0%
West site	1.0×10^4	9.3×10^3	-7.1%	8.0×10^3	7.0×10^3	-10.9%
NYSDEC site	2.3×10^{3a}	2.3×10^3	--	4.2×10^3	3.2×10^3	-23.5%

[a] Ambient UFP concentration.
[b] Unit: particles cm^{-3}.
[c] Normalized by measurement data.

The comparisons between predicted and measured particle size distributions (PSDs) are also conducted, and 06/09/2005 (10:00-12:00) and 01/13/2009 (12:00-

14:00) scenarios are used as examples. As illustrated in Figure 5.8, CTAG captures the relative shapes of PSDs for both scenarios, but there are still discrepancies between the predictions and measurements. The condensation or evaporation of OC as well as coagulation plays an important role in the near-road evolution of the PSDs, and reliable and complete datasets for the emissions and compositions of OC can improve the precision of the PSDs' prediction.

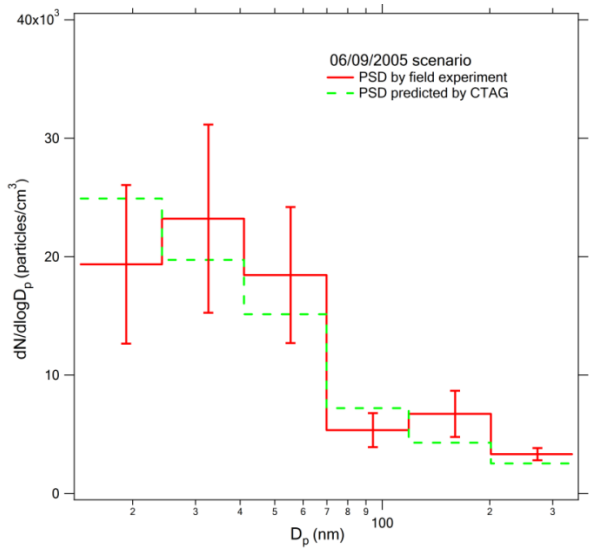

(a)

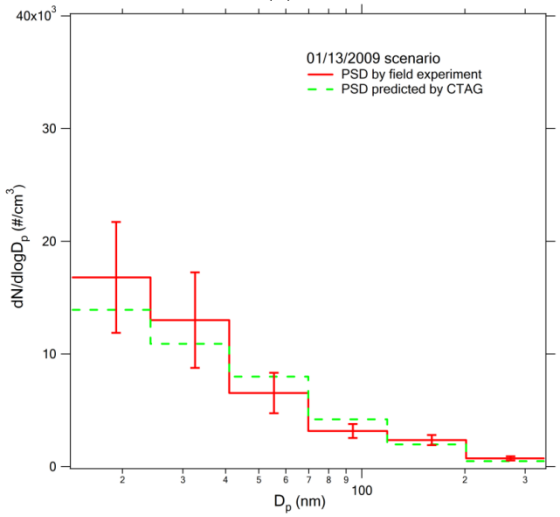

(b)

Figure 5.8. Comparisons of PSDs between predictions by CTAG and measurements for (a) 06/09/2005 (10:00-12:00) scenario and (b) 01/13/2009 (12:00-14:00) scenario

The evaluations in this paper as well as our previous papers (Wang and Zhang, 2009; Wang et al., 2011b; Steffens et al., 2012; Tong et al., 2012) have shown the capability of CTAG in predicting the near-road dispersion of multi-pollutants, while more tests are necessary before we are confident that CTAG is suitable for most air quality problems. However, the novel multi-scale structure proposed in this paper can potentially be a useful methodology for the study of vehicular UFPs emissions.

5.3.3. Application of CTAG to evaluate the impacts of emission reductions in a proof-of-concept case study

In this section, CTAG is employed in a proof-of-concept case study in evaluating the impacts of emission reduction measures. A large coal-fired power plant (CFPP, ~260 MWe), located northwest to the downtown Rochester and the intersection micro-environment, was shut down for conversion to natural gas in early 2008, as illustrated in Figure 1. Another major change in emission sources around that period was the adoption of ULSD for heavy-duty diesel trucks. It has been observed in field measurements that air quality in Rochester area was affected by the CFPP shutdown and the ULSD adoption from late 2006 to early 2008 (Wang et al., 2011a).

More specifically, in order to elucidate their impacts on residential communities and schools near the highway intersection, simulations are conducted on the following scenarios, illustrated in Table 6. The influence of CFPP shutdown is reflected by the variations in ambient UFP concentrations (collected at the NYSDEC site) in near-road

domain, since CFPP is located upwind of the highway intersection for the following scenarios (wind blows from northwest).

- 2005 Base: 01/20/2005 (11:00-12:00) scenario is chosen as a baseline case to characterize the conditions prior to CFPP shutdown and ULSD adoption.
- 2009 Base: 01/17/2009 (10:00–11:00) scenario is selected as a baseline case to characterize the conditions after CFPP shutdown and ULSD adoption. This scenario was selected because its meteorology (wind velocity, wind direction, temperature and relative humidity, etc) and traffic conditions (vehicle speed and traffic volume, etc) were similar to those in the 2005 Base.
- Two other scenarios, 2005 LB and 2009 HB (i.e., controlled numerical experiments), are constructed to further separate the impacts of power plant and transportation sources, listed in Table 5.6.

Table 5.6 Comparisons between four cases to characterize the impacts of CFPP shutdown and ULSD adoption

Scenario	CFPP shutdown	Ambient UFP concentration (particles cm^{-3})	ULSD adoption	Fuel sulfur content (ppm)	Reduction in UFP concentration[b]
2005 Base	No	1.56×10^4	No	350	N/A
2005 LB[a]	Yes	3.16×10^3	No	350	-5.2% (-1.0% to -3.0%)
2009 HB[a]	No	1.56×10^4	Yes	15	-74.9% (-60.1% to -87.7%)
2009 Base	Yes	3.16×10^3	Yes	15	-80.6% (-69.3% to -90.3%)

[a] Controlled numerical experiment.
[b] Reduction in UFP concentration relative to 2005 Base.

Figure 5.9 illustrates the distributions of UFPs in the micro-environment for four cases, while the average and the ranges of UFPs reductions are listed in Table 5.6. Those statistics are based on around 2000 data points sampled in the residential community. Our simulation results suggest the following findings regarding the air

quality impact of CFPP shutdown and ULSD adoption: 1) Both CFPP shutdown and ULSD adoption improved the micro-environmental air quality near the intersection. 2) For the near-road communities, the ULSD adoption resulted in greater reductions in UFP concentrations than the CFPP shutdown. The magnitude of the reduction varies with the fraction of heavy-duty diesel trucks on the highways. 3) There are large variations in terms of the magnitudes of UFPs reductions within the community, shown in Table 5.6. In addition, the measurements from Wang et al. (2012) suggest a significant impact of ULSD on the drop of $PM_{2.5}$ and BC concentrations near the NYSDEC site. It is also observed from field measurements that the CFPP shutdown had a larger regional impact on air quality than ULSD adoption, due to the SO_2-related particle nucleation event (Wang et al., 2011a). These results from field measurements and CTAG simulations reveal the environmental benefits of CFPP shutdown and ULSD adoption. It should be noted that a comprehensive analysis of the long-term micro-environmental impact of the CFPP shutdown and ULSD adoption should be conducted by including a large set of meteorological and traffic conditions, which is beyond the scope of the current study.

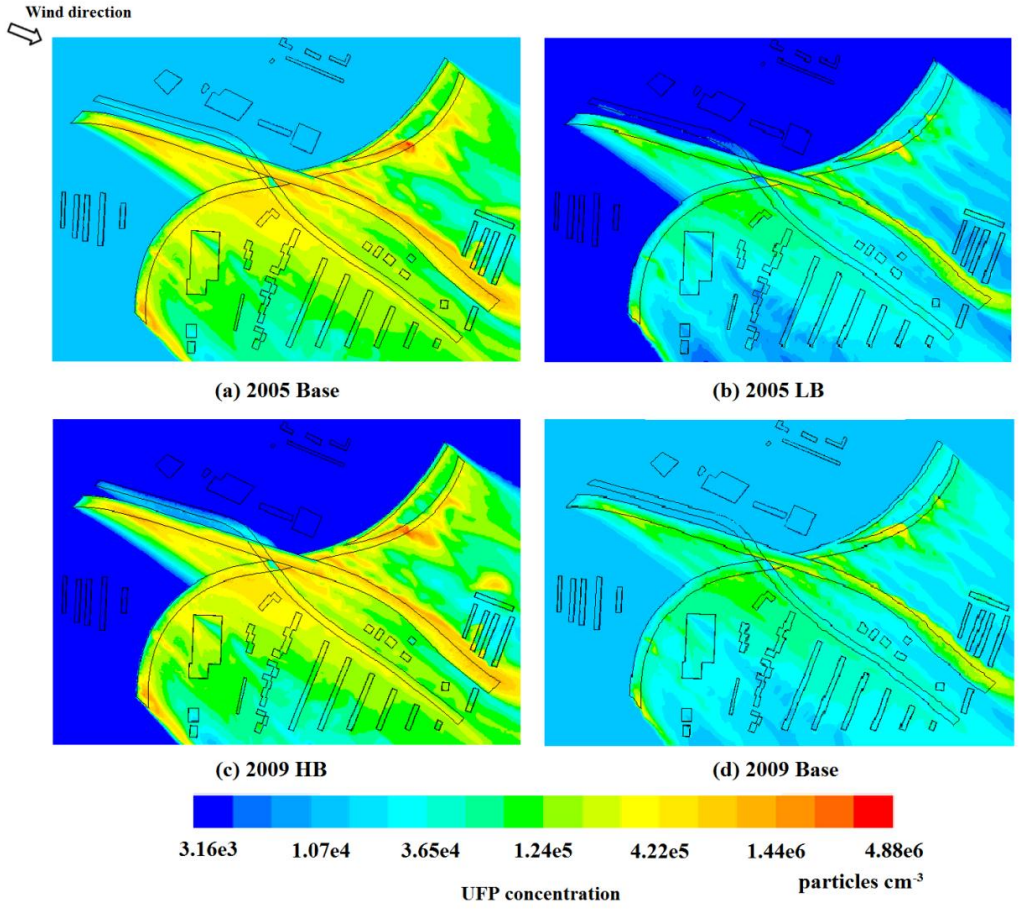

Figure 5.9. Time-averaged distributions of UFPs (1-500 nm) for the four cases described in Table 6, regarding the shutdown of CFPP and the adoption of ULSD. The wind direction is ~297 °

5.3.4 Uncertainties and limitations

Even though the CTAG model with the multi-scale structure has the capability in linking tailpipe emissions with near-road air quality mechanistically, its performance in the current and future applications will rely on the quality of the input data. As the emission characteristics vary among individual vehicles, an accurate representation of the vehicle population will improve the modeling results. Wang and Zhang (2012) evaluated the aerosol dynamics simulations of diluting diesel plumes by CTAG. The results show that predictions of UFP concentrations are sensitive to the exhaust-level

sulfuric acid concentrations. The installation of aftertreatment devices such as diesel particulate filter (DPF) affects the exhaust-level sulfuric acid concentrations significantly. For example, it has been shown that under certain operating conditions, the SO_2-to-SO_3 conversion rate can increase from 1-5% if without aftertreatment devices to more than 60% if equipped with aftertreatment devices in heavy-duty vehicles (NREL, 1999; Herner et al., 2011). This presents considerable challenges for predicting on-road particle emissions with more and more vehicles equipped with those aftertreatment devices join the on-road fleets.

Our current study focuses on the unsteady-state simulation with time-constant boundary conditions. Even though CTAG is capable of simulating the unsteady-state dispersion with time-varying boundary conditions, we did not have high-time resolution meteorological and traffic data (e.g., in minutes) for the intersection micro-environment to construct the transient scenarios. Future work will involve evaluating the performance of the CTAG model in resolving the transient spatial variations of air pollutants in the micro-environment with proper datasets.

CTAG is still computationally expensive compared to those widely-used parametric dispersion models for operationally purpose, e.g., AERMOD (Cimorelli et al., 2005) and OSPM (Berkowicz, 2000). However, CTAG has the potential to improve the parametric dispersion models to resolve complex environments, e.g., by incorporating RIT.

5.4. Conclusion

In this paper, a novel multi-scale structure has been introduced and implemented in CATG for simulating air quality in a micro-environment near a highway intersection. The processed on-road particle emissions can be generated in the on-road domain. This is an important process since it captures the formation of nucleation mode particles during the dilution process of the engine exhaust, which is strongly affected by traffic-related activity and meteorological conditions. The interactions between multiple exhaust plumes are also simulated in the on-road domain. These processed on-road particle emissions are then applied as the volume emission sources for the near-road simulations to characterize the spatial and temporal impacts of traffic-related emissions on micro-environmental air quality.

CTAG shows adequate agreement when compared with experimental measurements. The simulation results illustrate that the air quality in the intersection micro-environment is dominated by the traffic-related activity and the level of pollutant concentrations varies spatially and temporally. Additionally, as a proof-of-concept case study, CTAG has revealed relative impacts of the CFPP shutdown and the ULSD adoption on the air quality in the intersection micro-environment.

CHAPTER 6

ANALYSES OF TURBULENT FLOW FIELDS AND AEROSOL DYNAMICS OF DIESEL ENGINE EXHAUST INSIDE TWO DILUTION SAMPLING TUNNELS USING THE CTAG MODEL[*]

Abstract

The experimental results from laboratory emission testing have indicated that particulate emission measurements are sensitive to the dilution process of exhaust when using fabricated dilution systems. In this chapter, we first categorize the dilution parameters into two groups: 1) gas dynamics (e.g., mixing types, mixing enhancers, dilution ratios, residence time); 2) gas properties (e.g., temperature, relative humidity, particle size distributions of both raw exhaust and dilution gas). Then we employ the Comprehensive Turbulent Aerosol Dynamics and Gas Chemistry (CTAG) model to investigate the effects of those parameters on a set of particulate emission measurements comparing two dilution tunnels, i.e., a T-mixing lab dilution tunnel and a portable field dilution tunnel with a type of coaxial mixing. The turbulent flow fields and aerosol dynamics of particles are simulated inside two dilution tunnels. Particle size distributions under various dilution conditions predicted by CTAG are evaluated against the experimental data. It is found that in the area adjacent to the injection of exhaust, turbulence plays a crucial role in mixing the exhaust with the

[*]Wang, Y., Yang, B., Lipsky, E. M., Robinson, A. L., Zhang, K. M. Analyses of turbulent flow fields and aerosol dynamics of diesel engine exhaust inside two dilution sampling tunnels using the CTAG model. Environmental Science & Technology. In revision.

dilution air, and the strength of nucleation dominates the level of particle number concentrations. Further downstream, nucleation terminates and the growth of particles by condensation and coagulation continues. Sensitivity studies reveal that a potential unifying parameter for gas dynamics, i.e., the dilution rate of exhaust, plays an important role in new particle formation. The T-mixing lab tunnel tends to favor the nucleation due to a larger dilution rate of the exhaust than the coaxial mixing field tunnel. Our study indicates that numerical simulation tools can be potentially utilized to develop strategies to reduce the uncertainties associated with dilution samplings of emission sources.

6.1 Introduction

The development of emission inventories and regulations relies on the results from emission testing (Burtscher, 2005; Lipsky and Robinson, 2005). Because of its high temperature and high concentrations, the raw exhaust from combustion sources needs to be diluted for speciation and quantification, especially for its particulate components (Burtscher, 2005; Brockmann et al., 1984; Hildemann et al., 1989). Therefore, the fabricated dilution system is essential to almost all emission testing procedures and major combustion sources (Lipsky and Robinson, 2005; Brockmann et al., 1984; Hildemann et al., 1989).

Dilution systems have been utilized for various purposes: 1) to capture the atmospheric dilution, especially for establishing a link between the atmospheric dilution and the undiluted exhaust (Lyyranen et al., 2004; Ronkko et al., 2006); and 2) to preserve the exhaust properties as unbiased as possible from the measurement and

dilution setup artifacts to produce a so called “tailpipe-level” emissions as observed inside the exhaust pipe (Strand et al., 2004). For either purpose, the current dilution samplings have many known limitations and those limitations are pronounced for measuring the semi-volatile composition and the ultrafine range (<100 nm) of the particulate emissions. Dilution air properties have been shown to have a strong influence on particle size distributions. One can obtain up to two orders of magnitude change in nanoparticle concentrations from an engine operating at a stable steady state condition by changing dilution air properties (Abdul-Khalek et al., 1999). Nucleation-mode particles are found to be sensitive to sampling conditions and thus the laboratory measurements may differ considerably from on-road emissions depending on chosen dilution parameters (Ronkko et al., 2006).

In recent years, numerical methods have been utilized to improve our understanding of the flow field and aerosol dynamics inside the dilution system (Casati et al., 2007; Shi and Harrison, 1999; Vouitsis et al., 2005). Vouitsis et al. (2005) applied a box model of nucleation, condensation, coagulation and diffusional losses to the walls in a porous dilutor, assuming that the mixing of exhaust within the dilutor occurs adiabatically and instantaneously. One challenge regarding the dilution process of exhaust is that the majority of dilution tunnels are operated under a turbulent condition. Therefore, it is important to understand the turbulence and its effect on aerosol dynamics inside the dilution tunnels, especially those with complex geometries. Under this circumstance, Computational Fluid Dynamics (CFD) has been employed to simulate the nucleation of dibutylphthalate in a perforated tube diluter (Pyykonen et al., 2007).

In Chapter 4, we have evaluated the CTAG (that stands for the Comprehensive Turbulent Aerosol Dynamics and Gas Chemistry) model, a CFD-based turbulent reacting model, in resolving vehicle-induced turbulence and aerosol dynamics of individual plumes in the atmosphere (Wang and Zhang, 2012). In this chapter, we employ CTAG to investigate the dilution processes of the same diesel exhaust inside two dilution tunnels. We aim to answer the following questions: 1) How do the turbulent mixing processes in the two dilutors differ from each other? 2) How does the turbulent mixing process interact with aerosol dynamics that affects particulate emission measurements? Future studies will compare the turbulent mixing processes inside the dilution systems with those in the atmosphere.

6.2 Dilution parameters controlling the sampling measurement

Studies have shown that various design and operation parameters can affect the functionality of dilution tunnels (Burtscher, 2005; Lipsky and Robinson, 2005; Kittelson et al., 1998; Lipsky et al., 2002; Mathis et al., 2004). We separate them into two groups based on their characteristics, as described in Table 1, which provides the background for the follow-up discussions and potentially the guideline for future designs.

Table 6.1 Dilution parameters controlling the sampling measurement of engine emissions

Group I. Gas dynamics	Fixed parameter: Tunnel configuration	Mixing type of the dilution tunnel: T-mixing dilution tunnel, coaxial mixing dilution tunnel (Lipsky and Robinson, 2005), perforated tube diluter (Dekati Ltd.), ejector diluter (Dekati Ltd.), rotating disk diluter (Matter Engineering Inc.), etc.
		The mixing enhancer: fan shape plate (Lipsky and Robinson, 2005), orifice plate, baffle, etc.
	Variable parameter: Operating condition	Dilution ratio (DR) at the end of the dilution tunnel
		Residence time inside the dilution tunnel
Group II: Gas property	Property of engine exhaust: temperature, water content, sulfuric acid concentration, OC concentration and composition, size distribution of the primary soot-mode particles, etc.	
	Property of dilution gas: temperature of dilution gas, relative humidity (RH), particle size distribution, OC concentration and composition, type of dilution gas (e.g., pure nitrogen or air), etc.	

The tunnel configuration in Group I ("gas dynamics") is usually designed ahead of the measurements and remains fixed during the measurements, while the operating conditions can be varied during the experiment depending on the purpose of the study. Sometimes there is no clear boundary for the fixed part and the variable part, e.g., even though the mixing type is fixed in the rotating disk diluter, the dilution ratio (DR) can still be changed by varying the rotating speed (Matter Engineering Inc.).

For Group II ("gas properties"), the property of exhaust depends on the types of fuel, engines, and their operating conditions during the experiment (Khalek et al., 2003). The property of dilution gas can be varied during the experiment depending on the purpose of the study (Mathis et al., 2004; Maricq et al., 1999).

In summary, these dilution parameters contribute to the complexity of the design and operation of dilution tunnels. Therefore, a thorough understanding of their individual effects as well as coupled effects is necessary. In this study, we focus on selected parameters in the two groups inside a single stage dilution tunnel, while in

some experiments, two or more stages of the dilution systems have been combined to achieve the desired DRs (Ronkko et al., 2006; Casati et al., 2007).

6.3 Experimental data

Experiments were conducted to compare the performance of a portable field dilution tunnel, noted as "field tunnel", with a larger dilution tunnel primarily used in laboratories, noted as "lab tunnel" (Lipsky and Robinson, 2005). The emission source was provided by a single-cylinder Yanmar L70AE air-cooled diesel engine and tests were conducted at a low load (25% of full capacity). The inter-comparison experiments involved simultaneous sampling with the two dilution tunnels from the same location of an enclosed exhaust duct. Therefore this experiment setup eliminates the difference in exhaust properties, and focuses on the effect of the dilution process on particle number concentration measurements. Particle size distributions (PSDs) were measured from 10 – 460 nm using a TSI Scanning Mobility Particle Sizer (TSI 3081 DMA with the model 3010 CPC).

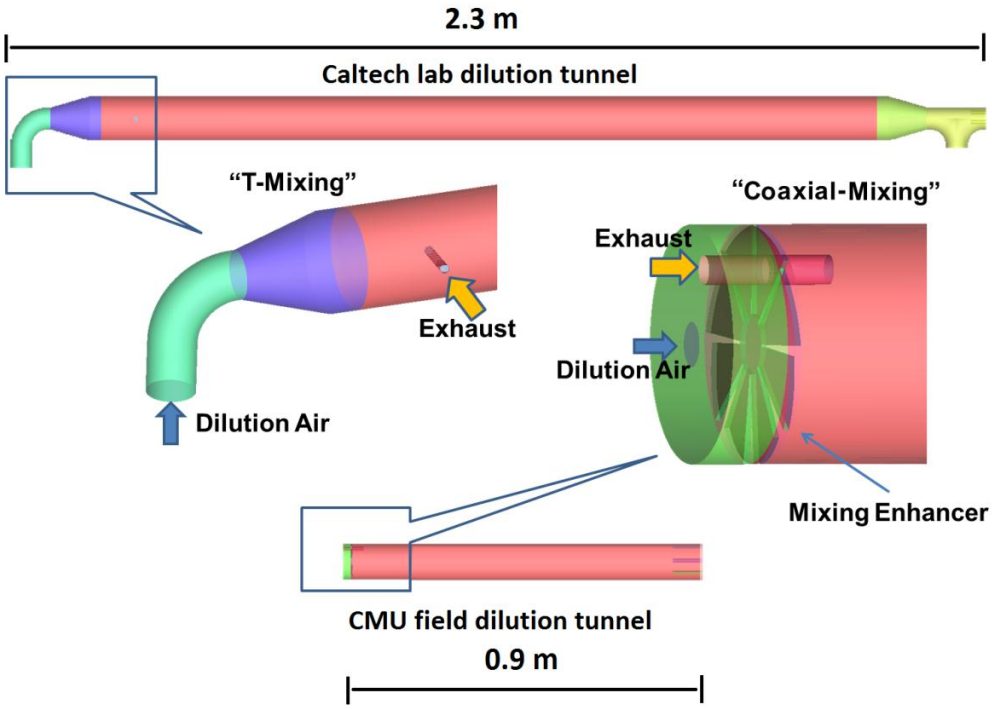

Figure 6.1. Configurations and three dimensional computational domains of two dilution tunnels

Figure 6.1 illustrates the difference in the configurations of lab tunnel and field tunnel, i.e., their Group I parameters: 1) In terms of mixing types, the lab tunnel employs a T-mixing configuration, while the field tunnel utilizes coaxial mixing; 2) in terms of mixing enhancers, a fan-shaped mixing enhancer is installed in the field tunnel, but not in the lab tunnel. The two dilution tunnels also vary in size with the lab tunnel (2.3 m) longer than the field tunnel (0.9 m). The flow rate through the lab tunnel is ~1000 lpm, while the field tunnel is operated at ~174 lpm. Therefore both tunnels are maintained at a residence time (RT) of ~2.5 s (Lipsky and Robinson, 2005). DR is determined by simultaneously measuring CO_2 levels of exhaust and diluted exhaust at the end of the tunnels and defined as:

$$DR = \frac{(CO_2)_{ex} - (CO_2)_{amb}}{(CO_2)_{tun} - (CO_2)_{amb}} \quad (6.1)$$

where $(CO_2)_{ex}$ is the exhaust CO_2 level, $(CO_2)_{amb}$ is the CO_2 level of the dilution air, and $(CO_2)_{tun}$ is the CO_2 level of the diluted exhaust. The variation of DR is achieved by adjusting the exhaust flow rate, while keeping the flow rate of the dilution air as a constant (Vouitsis et al., 2005). Experiments under two DRs, 20 (noted as DR20) and 120 (noted as DR120) were conducted for both tunnels.

6.4 Modeling method

6.4.1 The CTAG model

The CTAG model is employed to simulate the turbulent flow field and aerosol dynamics within the dilution tunnels. The turbulent flow field inside the dilution tunnel is solved by the Large-eddy Simulation (LES) model (described in Chapter 5), which has demonstrated the good ability to capture the flow and mixing features in internal flows when compared to experimental data (Guleren and Turan, 2007; Wegner et al., 2004). Aerosol dynamics, including nucleation, condensation, evaporation, coagulation, and deposition, is used to capture the evolution of number concentration, size distribution, and chemical composition of multi-component aerosol particles (Wang and Zhang, 2012) and is described in Chapter 4. One extension of the CTAG model is the deposition of particles on the surfaces of dilution tunnel. For the ultrafine particles considered in this study, Brownian deposition is important and equations from Papavergos and Hedely (1984) are used. The deposition velocity in Talbot et al. (1980) is used to account for the thermophoretic deposition.

A presumed finite-mode probability-distribution function (PDF) method, also known as a multi-environment CFD micro-mixing model (Fox, 2003), is used to couple the turbulent mixing process with the aerosol dynamics and also capture the micro-mixing effects on aerosol dynamics. In this approach, each computational cell in the CFD grid is divided into N_e modes or environments, which correspond to a discretization of the presumed composition PDF into a finite set of delta (δ) functions:

$$f_\Phi\left(\Psi;x,t\right)=\sum_{n=1}^{N_e}p_n\left(x,t\right)\prod_{\alpha=1}^{N_s}\delta\left[\Psi_\alpha-\left\langle\phi_\alpha\right\rangle_n\left(x,t\right)\right] \tag{6.2}$$

where f_Φ is the joint PDF of all scalars, N_e is the number of environments, N_s is the total number of scalars (species), p_n is the probability of environment n or volume fraction of environment n, and $\left\langle\phi_\alpha\right\rangle_n$ is the mean composition vector in environment n.

The weighted concentration is defined as:

$$\left\langle s\right\rangle_n=p_n\left\langle\phi\right\rangle_n \tag{6.3}$$

The transport of probability:

$$\frac{\partial p}{\partial t}+\nabla\cdot\left(\vec{v}p-D_t\nabla\cdot p\right)=G\left(p\right)+G_s\left(p\right) \tag{6.4}$$

$$\frac{\partial\left\langle s\right\rangle_n}{\partial t}+\nabla\cdot\left(\vec{v}\left\langle s\right\rangle_n-D_t\nabla\cdot\left\langle s\right\rangle_n\right)=M^n\left(p,\left\langle s\right\rangle_1,...,\left\langle s\right\rangle_{N_e}\right)+M_s^n\left(p,\left\langle s\right\rangle_1,...,\left\langle s\right\rangle_{N_e}\right)+p_nS\left(\left\langle\phi\right\rangle_n\right) \tag{6.5}$$

where G and M^n are the rates of change of $p=[p_1, p_2, ..., p_N]$ and $\langle s \rangle_n$ due to micro-mixing, respectively, G_s and M_s^n are additional micro-mixing terms to eliminate the spurious dissipation rate in the mixture-fraction-variance transport equation, and S is the chemical source term. The mean compositions of the scalars are given by:

$$\langle \phi \rangle = \sum_{n=1}^{N_e} p_n \langle \phi \rangle_n = \sum_{n=1}^{N_e} \langle s \rangle_n \tag{6.6}$$

A three-environment presumed-PDF model is used for the coupling of the turbulent mixing process and the aerosol dynamics inside the dilution tunnel, which approximates the fluctuations of the species concentrations on the sub-grid scale. One inlet stream is environment 1 (exhaust), the other inlet stream is in environment 2 (dilution air), and environment 3 is a mixture of the two fluids.

The aerosol dynamics module and the presumed finite-mode PDF method are written in C-language and incorporated into ANSYS FLUENT through User-Defined Function (UDF).

6.4.2 Model implementation

As shown in Figure 6.1, the three-dimensional computational domains of the two dilution tunnels are built and discretized into approximately 1 million hexahedral cells. Mesh independence studies (with 0.5 million and 2 million cells) have been conducted to assure that the grid resolution is fine enough for the accuracy of the simulation (difference within 7% for the simulation results of the dispersion of CO_2). A no-slip

condition is set to the wall of the dilution tunnels. Boundary conditions for the velocity inlets of diesel exhaust and dilution air under different cases are shown in Table 6.2. For the outflow condition, a zero normal first derivative of all quantities is fulfilled.

Table 6.2 Boundary conditions for CTAG simulations under different cases, obtained from the experiment.

Case	Diesel exhaust					Dilution air				Dilution-corrected UFP concentration at the end of tunnels (particle cm^{-3})
	Exhaust temperature (K)	Sulfuric acid mass concentration	Exhaust OC mass concentration	Exhaust CO_2 mass concentration	UFP concentration (particle cm^{-3})	Dilution air temperature (K)	RH of dilution air (@ 297 K)	Dilution air CO_2 mass concentration	UFP concentration (particle cm^{-3})	
1. Lab20	514	2.32×10^{-6}	5.52×10^{-5}	0.086	8.52×10^{7}	297	10 %	5.80×10^{-4}	7.20×10^{4}	1.54×10^{9}
2. Lab120	514	2.32×10^{-6}	5.52×10^{-5}	0.086	8.52×10^{7}	297	<1 %	5.80×10^{-4}	7.20×10^{4}	7.93×10^{8}
3. Field20	514	2.32×10^{-6}	5.52×10^{-5}	0.086	8.52×10^{7}	297	<1 %	5.80×10^{-4}	7.20×10^{4}	7.47×10^{8}
4. Field120	514	2.32×10^{-6}	5.52×10^{-5}	0.086	8.52×10^{7}	297	<1 %	5.80×10^{-4}	7.20×10^{4}	7.69×10^{8}

As shown in Table 6.2, most of the gas properties, i.e., the Group II parameters, are the same under the four cases, except the RH of the dilution air. For the lab tunnel, the dilution air used at DR120 (Case 2) is drier than that of DR20 (Case 1), while the RH of the dilution air used in the field tunnel (Case 3 and 4) is also low. The exhaust sulfuric acid mass concentration depends on the fuel sulfur content (FSC), the SO_2-to-SO_3 conversion rate (cr), and the air-fuel ratio. FSC is estimated at ~500 ppm for the diesel fuel used in the measurement. A/F is ~32 for the low load. cr is approximated as 5%, when no oxidation catalyst is used (Vouitsis et al., 2005). The level of organic carbon (OC) is measured and its volatility distribution is described in Table 6.3 and 6.4. The Clausius-Clapeyron relation is used to estimate the vapor pressure of OC at different temperatures:

$$\ln \frac{P_{vap,T_1}}{P_{vap,T_2}} = \frac{\Delta H_{vap}}{R} \cdot \left(\frac{1}{T_2} - \frac{1}{T_1} \right) \tag{6.6}$$

The size distribution of particles in the dilution air and soot-mode particles in the exhaust are obtained from the experimental measurements. PSD modeled by CTAG is represented by 22 size bins ranging from 1 to 400 nm.

Table 6.3 Enthalpies of vaporization (Pyykonen et al., 2007)

C^* ($\mu g\ m^{-3}$)	ΔH_{vap} (kJ mol^{-1})	Molecular weight (g mol^{-1})
0.01	77	524
0.1	73	479
1	69	434
10	65	389
100	61	344
1000	57	299
10000	54	254

Table 6.4 Volatility distribution of OC emissions obtained from measurement

C* ($\mu g\ m^{-3}$)	0.01	0.1	1	10	100	1000	10000
f_{SVOC}	0.03	0.06	0.09	0.14	0.18	0.3	0.2

f_{SVOC} is the mass fraction of the emissions that is in that volatility bin.

6.5 Results and discussion

6.5.1 Analysis of turbulent flow fields inside two dilution tunnels

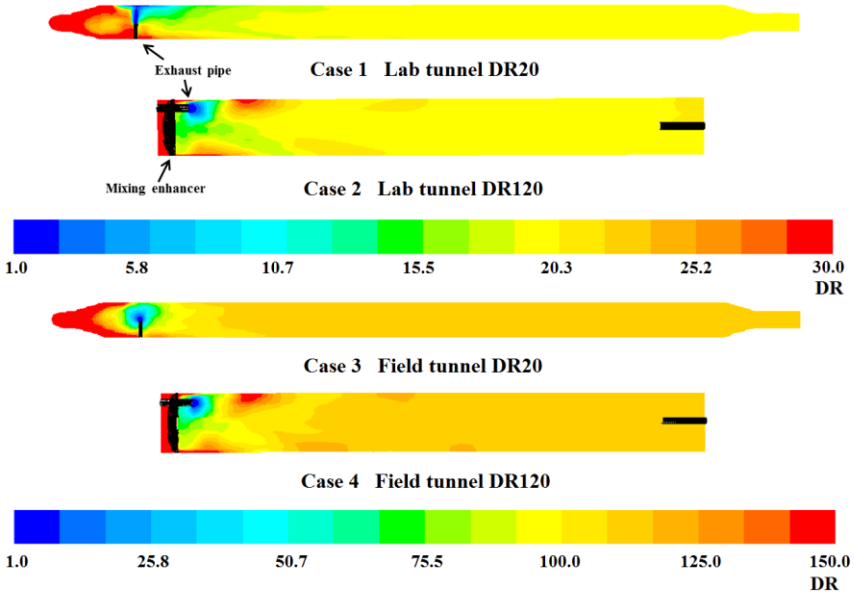

Figure 6.2. Time-averaged distributions of DR in the cross-section through the exhaust pipe within the two dilution tunnels. Blue represents the exhaust and red represents the dilution air, colors between blue and red represents the degree of dilution

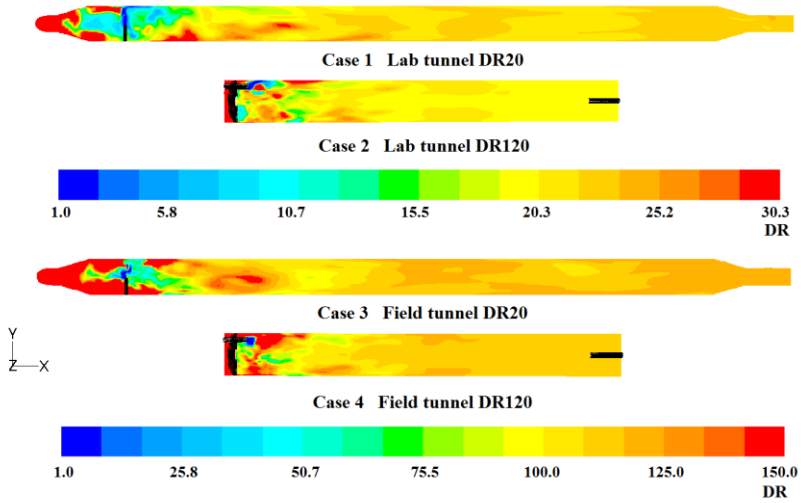

Figure 6.3. Instantaneous distribution of DRs for the two dilution tunnels under DR20 and DR120

The dilution process of diesel exhaust inside the dilution tunnel is indicated by the DR, shown in Figure 6.2. It can be seen that due to the effect of strong turbulence near the exhaust pipe, exhaust is mixing rapidly with the dilution air, illustrated by the fast transition in colors. The spatial inhomogeneity disappears under turbulent and molecular mixing. For both tunnels, the well-mixed status is achieved before the diluted exhaust reaches the end of the dilution tunnels.

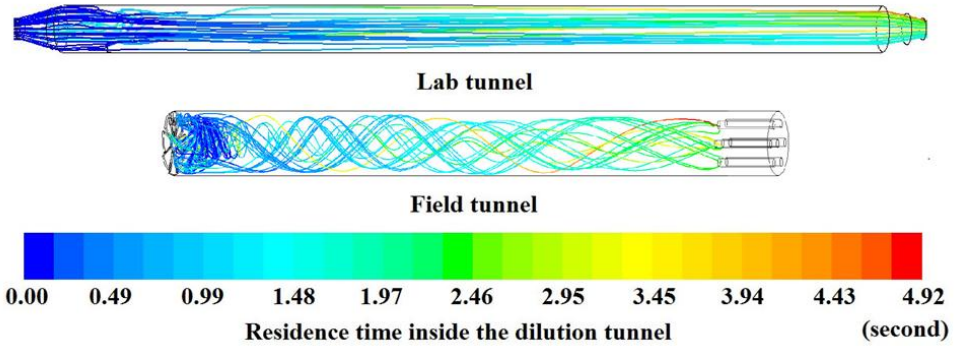

Figure 6.4. Pathlines noted by the residence time inside the dilution tunnels

The flow patterns inside two dilution tunnels are examined. As illustrated in Figure 6.4, the pathline shows that for lab tunnel, the diluted exhaust moves relatively parallel toward the downstream, while for field tunnel, the diluted exhaust rotates forward due to the effect of the mixing enhancer. The residence time inside the dilution tunnel (RT) used in the experiment is defined as the approximate travel time of the mixture. RT simulated by CTAG is ~ 2.5 s, similar to that estimated in the experiment. The residence time of certain amount of diluted exhaust is longer due to the recirculation in the rear of the mixing enhancer.

Of particular note is that in general, the DR characterized in the dilution sampling measurements is the value at the end of the dilution tunnels. However, inside the dilution tunnel (especially near the exhaust pipe), there is a wide range of DRs, due to the spatial inhomogeneity. With LES model, CTAG captures the instantaneously and time-averaged profile of DRs inside the tunnels, which can be a challenge for those models based on empirical equations or assumptions, especially in complicated domains.

In summary, the complexity in the turbulent flow field makes it necessary to employ a suitable unsteady turbulence model for the prediction of evolution of exhaust particles, as described in Section 6.5.2.

6.5.2 Evaluation of aerosol dynamics inside two dilution tunnels

6.5.2.1 New particle formation and the evolution of particle number concentrations inside the tunnels

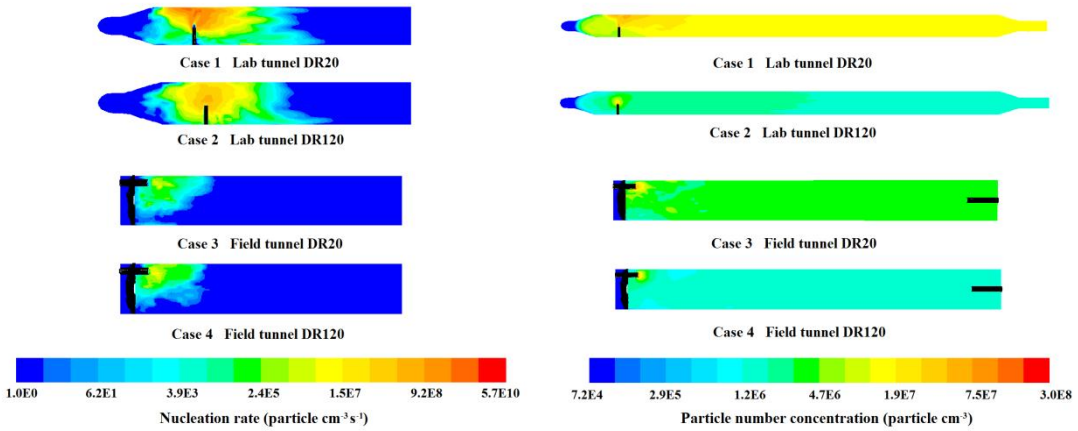

(a) (b)

Figure 6.5. Time-averaged distributions of (a) nucleation rate (near the injection area of exhaust) (b) the level of UFP concentration inside the two dilution tunnels

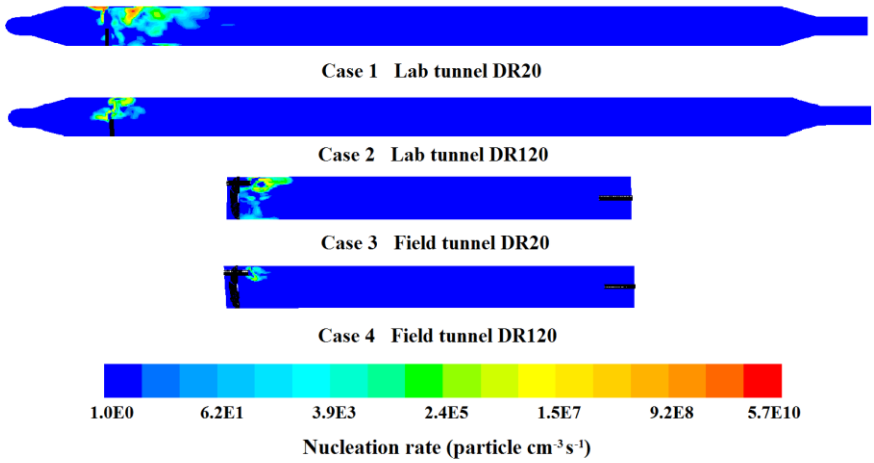

Figure 6.6. Instantaneous distributions of nucleation rate inside the two dilution tunnels

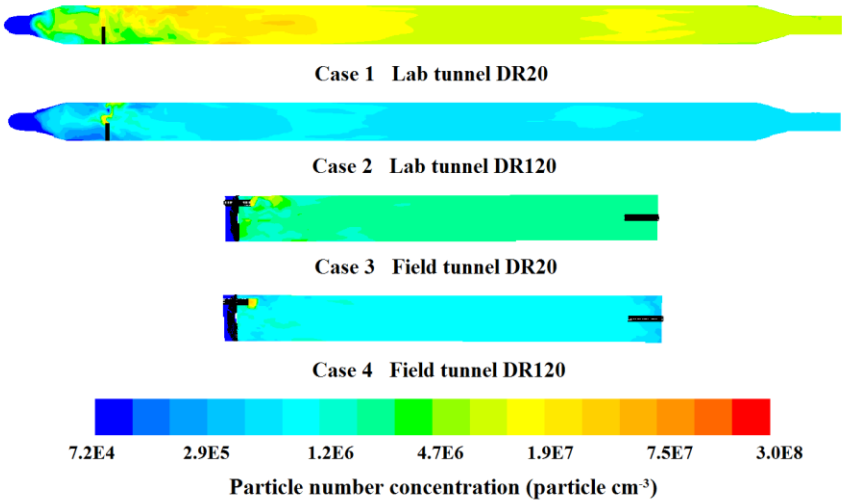

Figure 6.7. Instantaneous distributions of UFP concentration inside the two dilution tunnels

Figure 6.6(a) illustrates the nucleation process in the two dilution tunnels and only the areas near the injection of the exhaust are shown since the nucleation process ceases quickly after the exhaust is diluted. Turbulent mixing affects the local gaseous species concentration, temperature, and RH, which play important roles in determining the formation of UFPs. The maximum nucleation rate in the lab tunnel DR20 (Case 1) is approximately 2 ~ 3 orders higher than the other three cases (Case 2, 3 and 4). The

dilution air in Case 2, 3 and 4 is drier than Case 1, which partially contributes to the differences. Further analysis is conducted in Section 6.5.3.1.

The contours of UFP concentration inside the dilution tunnels are shown in Figure 6.6(b). The level of UFP concentration varies among cases due to their different nucleation rates. With a stronger nucleation process, the UFP concentration at the end of the lab tunnel DR20 (Case 1) is higher than those in the other three cases (shown in Table 6.2 as well). The UFP concentration at the end of the lab tunnel under DR120 is similar to that of the field tunnel under DR120 since nucleation is suppressed for both cases. In the area adjacent to the injection of exhaust, turbulence plays a crucial role in mixing the exhaust with the dilution air, and the strength of nucleation dominates the level of UFP concentration. Further downstream, nucleation terminates and the growth of UFPs by condensation and coagulation continues.

6.5.2.2 Evaluation of PSDs between CTAG and measurement

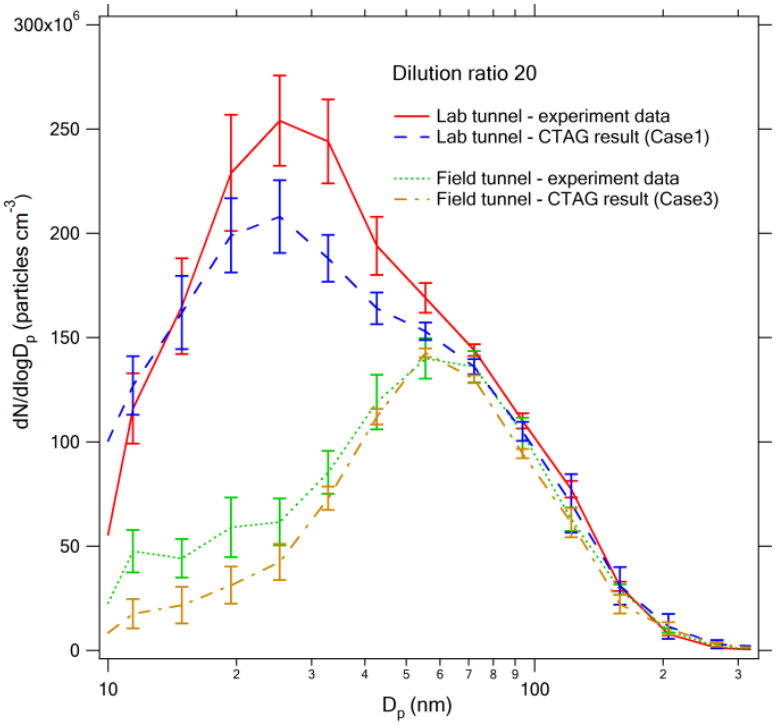

(a)

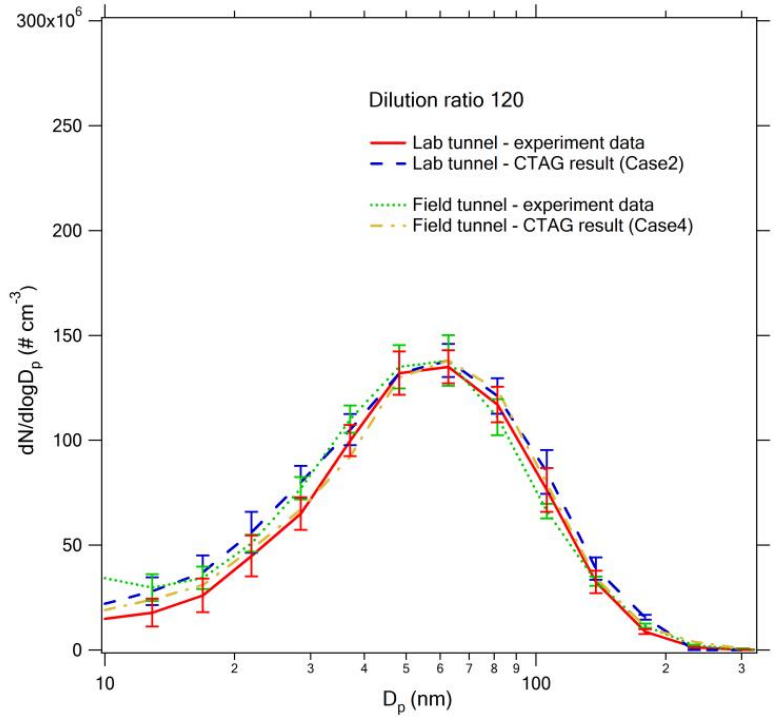

(b)

Figure 6.8. Dilution-corrected PSDs at the end of two dilution tunnels under (a) DR20 (b) DR120

The comparisons between the measured and simulated PSDs are shown in Figure 6.8 for both dilution tunnels under DR20 and DR120 conditions. A large nucleation mode is observed for the lab tunnel under DR20 due to the strong nucleation, while it is rarely observed for the other three cases. Therefore, both measurements and simulations in the study show that nucleation is sensitive to the dilution conditions (e.g., RH of the dilution air and the mixing type). Due to the growth by the condensation of OC and sulfuric acid, as well as the coagulation between the particles, the nucleation mode at the end of the lab tunnel at DR20 peaks at around 25 nm. It is also observed that the accumulation mode is relatively stable, which is consistent with the hypothesis that the majority of particles in the accumulation mode are carbonaceous agglomerates that are unaffected by the changes in dilution conditions (Lipsky and Robinson, 2005). Meanwhile, the volume size distributions from both measurement and CTAG predictions show excellent agreements for the two dilution tunnels, indicating that the observed new particle formation does not affect overall mass or the accumulation mode. The volume size distributions are shown in Figure 6.9.

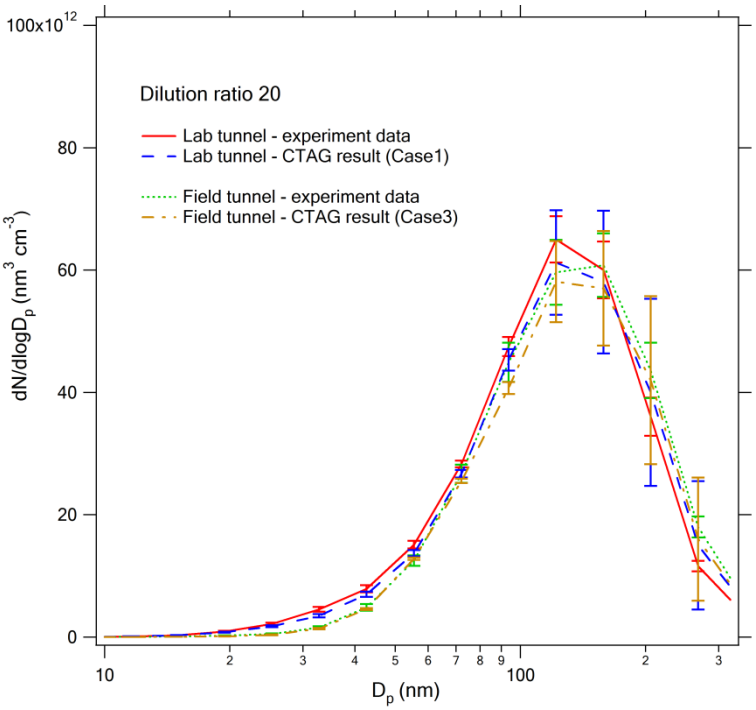

Figure 6.9. Comparison of volume size distributions between CTAG and measurement inside the two dilution tunnels

PSDs simulated by CTAG capture the general shapes of measured PSDs, although the model under-predicts the concentrations near the peak of the nucleation mode for the lab tunnel under DR20 (Case 1) in Figure 6.8(a). This may be caused by the difference between estimated and actual levels of sulfuric acid, and further analysis is in Section 6.5.5. The weighted deviation of PSD for the lab tunnel under DR20 between simulation and measurement is 12.6%, while the weighted deviation for the field tunnel under DR20 is 8.5%. The differences between simulation and experiment for both tunnels under DR120 are less than 3% since only the accumulation mode exists.

6.5.3 Sensitivity analysis of dilution parameters

As discussed earlier, there are three differences in dilution parameters during the measurements: RH (Group II), the mixing type (Group I), and the mixing enhancer (Group I). Therefore, the method of exclusion is utilized to investigate their individual effect on the formation of UFPs. The effect of RH (Group II) is studied firstly, since the consistency in Group II can provide the unbiased conditions for later investigations in Group I in Section 6.5.3.2 and 6.5.3.3. DR is fixed as 20 for all cases, while other parameters are shown in Table 6.5.

Table 6.5 Sensitivity study of dilution parameters (variations from the validated cases are highlighted)

		DR	RH of dilution air (@ 297 K)	Mixing enhancer	RT	Dilution-corrected UFP concentration at the end of tunnels (particle cm^{-3})	Relative change based on Base case	Maximum dilution rate of exhaust (s^{-1})
Case1[a]	Lab tunnel	20	10%	No	~2.5 s	1.54×10^9	N/A (Base Case)	83.2
Case3	Field tunnel	20	<1%	Yes	~2.5 s	7.47×10^8	-5.3% (to Case 6)	31.9
Case5	Lab tunnel	20	**<1%**	No	~2.5 s	8.42×10^8	-45.5% (to Case 1)	83.2
Case6[a]	Field tunnel	20	**10%**	Yes	~2.5 s	7.89×10^8	N/A (Base Case)	31.9
Case7	Lab tunnel	20	10%	**Yes**	~2.5 s	1.82×10^9	18.0% (to Case 1)	124.8
Case8	Field tunnel	20	10%	**No**	~2.5 s	7.76×10^8	-1.6% (to Case 6)	11.9
Case9	Lab tunnel	20	10%	Yes	**~1.3 s**	2.22×10^9	43.3% (to Case 1)	160.1
Case10	Lab tunnel	20	10%	No	**~5.0 s**	8.50×10^8	-45.0% (to Case 1)	36.5
Case11	Field tunnel	20	10%	Yes	**~1.3 s**	8.22×10^8	4.2% (to Case 6)	49.7
Case12	Field tunnel	20	10%	Yes	**~5.0 s**	7.49×10^8	-5.1% (to Case 6)	18.1

[a] Base cases of lab tunnel (Case 1) and field tunnel (Case 6).

6.5.3.1 Effect of RH of the dilution air (Group II)

RH of dilution air is found to have a considerable effect on the formation of UFPs during the dilution process, and higher RH can increase the amount of nucleation mode particles (Particulate, 2005). Sensitivity studies (Case 5 and Case 6) are

conducted, since RH of the dilution air used in the experiment is different for the two tunnels, which could cause the difference in PSDs.

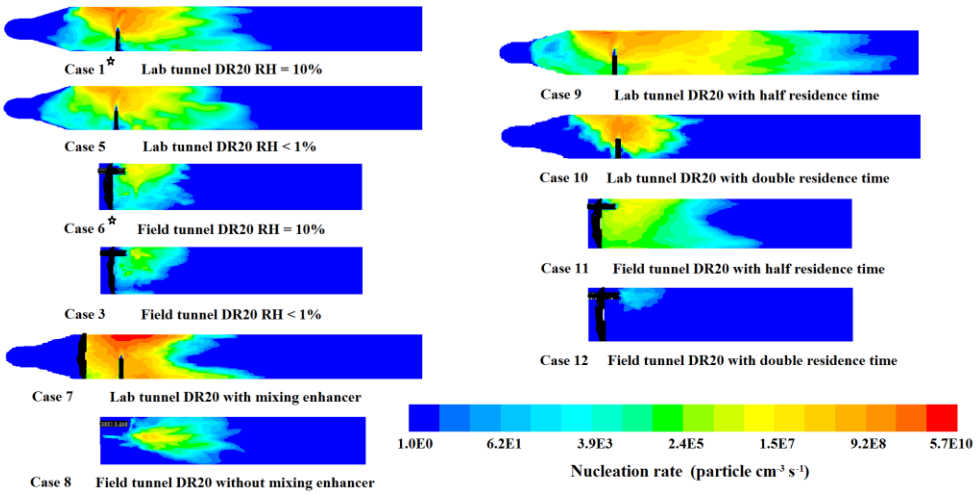

Figure 6.10. Time-averaged nucleation rate inside two dilution tunnels for sensitivity studies

As shown in Figure 6.10, for both tunnels, stronger nucleation can be observed under the higher RH, i.e., 10% (Case 1 vs. Case 5; Case 3 vs. Case 6). Meanwhile, for Case 3 and Case 5, even if the dilution air is dry (<1%), nucleation still occurs in both tunnels. This is because the water vapor in the exhaust can increase the RH of the mixture to more than 5% near the exhaust pipe when the hot exhaust is cooled by the cold dilution air. PSDs in Figure 6.11(a) show that a large nucleation mode exists under the high RH for lab tunnel (Case 1), while under the low RH (Case 5), nucleation is considerably suppressed. The UFP concentration at the end of the lab tunnel under low RH is 45.5% lower than that under high RH (Table 6.5). For the field tunnel, RH has shown a smaller impact on nucleation and there is no nucleation mode observed under both high and low RH (Case 3 and Case 6). The deference in UFP concentration is only 5.3%.

The inter-comparison shows that under the same RH of 10%, the UFP concentration in the lab tunnel is about 95.2% higher than that in the field tunnel. Therefore, RH cannot explain the difference between the two dilution tunnels for the nucleation event, and in the following studies, Case 1 and Case 6 (RH of 10%) serve as the base cases for the lab tunnel and field tunnel, respectively.

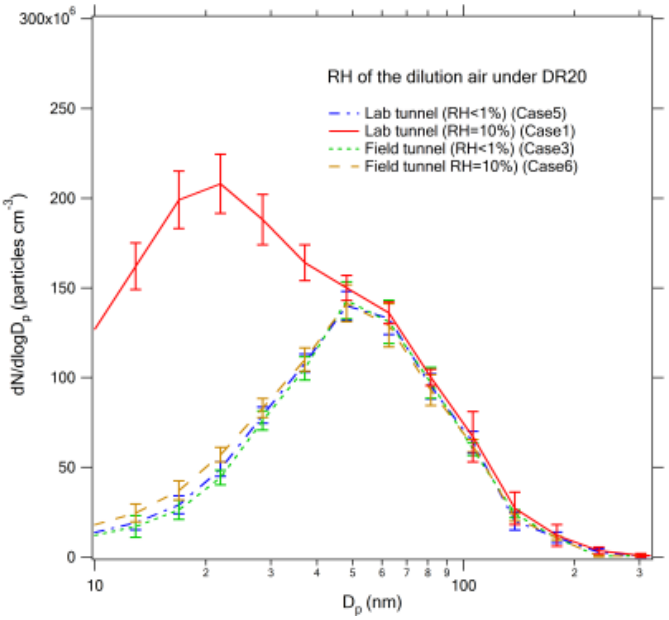

(a)

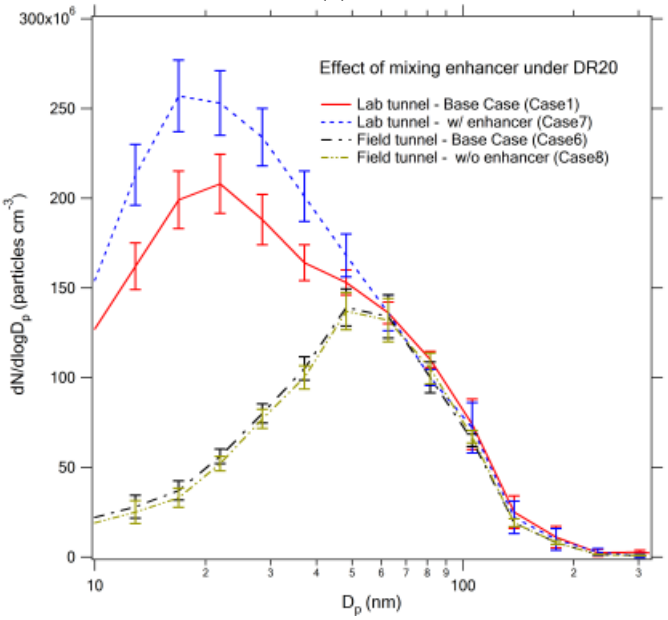

(b)

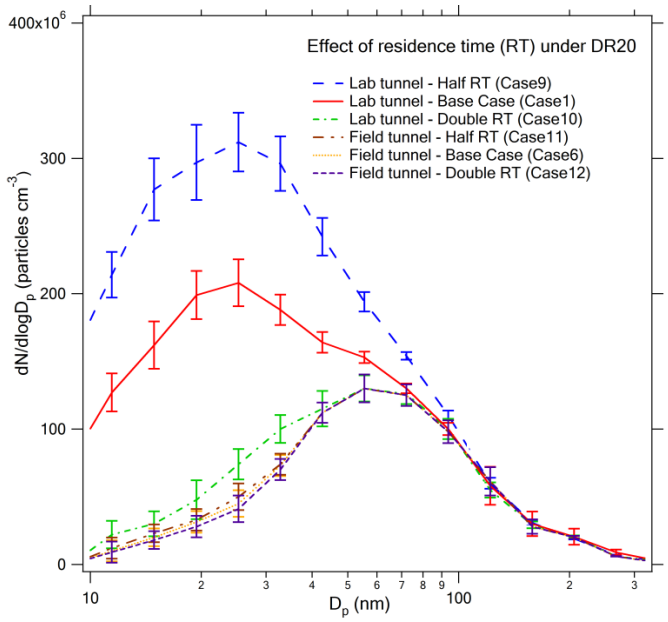

(c)

Figure 6.11. Dilution-corrected PSDs at the end of the two dilution tunnels for sensitivity studies

6.5.3.2 Effect of the mixing types and mixing enhancer (Fixed parameter in Group I)

As discussed earlier, there are two differences in the configuration of the dilution tunnel, one is the mixing type, and the other is the mixing enhancer. Since the mixing type is the basic design of the dilution tunnel and remains unchanged, sensitivity study regarding the installation or not of the mixing enhancer is then conducted (Case 7 and Case 8), while other parameters in Group I and II are the same for both tunnels.

- Lab tunnel installed with the mixing enhancer

For comparison, the same fan-shaped mixing enhancer is installed in lab tunnel upstream where the dilution air and exhaust meet, as shown in Figure 6.10 (Case 7). The mixing enhancer disturbs the dilution air before it mixes with exhaust, and increases the turbulence level of the incoming dilution air. As shown in Figure 6.10,

the mixing enhancer becomes a distinct boundary for the nucleation process since the mixing of exhaust and dilution air occurs instantaneously behind the mixing enhancer. As illustrated in Figure 6.10, the maximum nucleation rate is enlarged with the mixing enhancer (Case 7 vs. Case 1), while a larger nucleation mode exists in the PSD of lab tunnel with the mixing enhancer (Figure 6.11(b)). The UFP concentration at the end of lab tunnel increases 18.0% when compared to the case without the mixing enhancer (Case 1).

- Field tunnel without mixing enhancer

The field tunnel without the mixing enhancer is also created to investigate the effect of the mixing enhancer inside field tunnel (Case 8). As shown in Figure 6.10, since there is no disturbance from the mixing enhancer, nucleation occurs at the shear layer where the exhaust encounters the dilution air. The maximum nucleation rate is similar to that of field tunnel with mixing enhancer. PSDs in Figure 6.11(b) have shown little difference for the cases with or without the mixing enhancer in field tunnel. The UFP concentration at the end of the field tunnel for the case without the enhancer is only 1.6% lower than that with the enhancer (Table 6.5), suggesting that under the coaxial mixing, the mixing enhancer plays a less important role in altering the nucleation process.

For both tunnels without the mixing enhancer (Case 1 and Case 8), the UPF concentration at the end of the lab tunnel is 98.5% higher than that of the field tunnel, suggesting that instead of the mixing enhancer, the mixing type causes the main difference in the formation of UFPs between the two dilution tunnels.

6.5.3.3 Effect of residence time (RT) inside the dilution tunnel (Variable parameter in Group I)

Besides the investigations on the differences between the two dilution tunnels, the effect of RT is also studied. RT can be altered when the flow rates of exhaust and dilution air vary at the same ratio simultaneously. Two RTs (~1.3 s and ~5.0 s) are generated for the comparisons (Case 9 to 12).

As shown in Figure 6.10, the levels of nucleation have shown large differences under various RTs, even within the same tunnel. For both tunnel, stronger nucleation can be observed under the shorter RT. A similar trend can be found for the PSDs at the end of the dilution tunnels under various RTs, as illustrated in Figure 6.11(c). It is shown that for the lab tunnel, the nucleation mode varies more significantly than that for the field tunnel. The differences in the UFP concentrations can vary by up to 45% with various RT for the lab tunnel and ~5% for the field tunnel (Table 6.5), suggesting the importance of RT in the operation of different types of dilution tunnels.

6.5.4 The dilution rate of the exhaust, a potential unifying parameter

In the sensitivity study, it has been shown that even under the same gas properties (Group II), there are still large differences in the formation of UFPs. Therefore, gas dynamics (Group I) is responsible for the differences in nucleation. So far, there are not a defined set of parameters to characterize the gas dynamics. In our study, the dilution rate of the exhaust is introduced to characterize the effect of gas dynamics on the dilution process and is represented by the scalar dissipation rate of exhaust (Pope, 1985):

$$\varepsilon_{\xi} = C_{\phi} \left\langle \xi'^2 \right\rangle \frac{\varepsilon}{k} \tag{6.7}$$

where k and ε are the turbulent kinetic energy and turbulent dissipation rate, respectively. $\left\langle \xi'^2 \right\rangle$ is the mixture variance and C_{ϕ} is a constant.

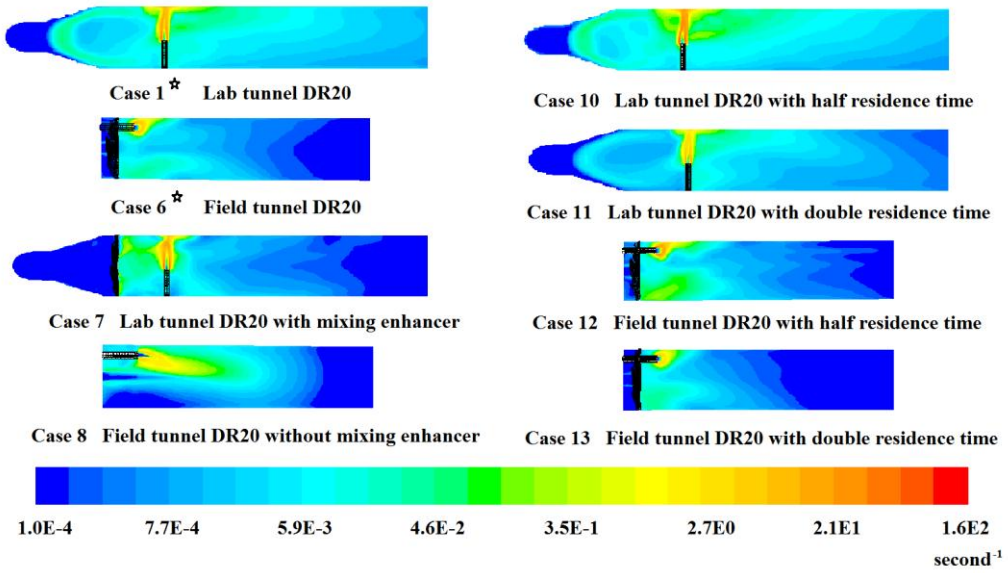

Figure 6.12. Time-averaged dilution rate of exhaust inside the dilution tunnels

The contour of dilution rate and the maximum values for various cases are shown in Figure 12 and Table 6.5. It can be seen that the level of dilution rate varies significantly with the mixing type, the mixing enhancer, and RT. T-mixing in lab tunnel has the advantage of allowing a higher degree of penetration into the cross-stream than the coaxial mixing in the field tunnel (Case 1 vs. Case 6). The corresponding maximum dilution rate in the lab tunnel (83.2 s^{-1}) is higher than that in the field tunnel (31.9 s^{-1}). The mixing enhancer also tends to increase the dilution rate, especially in areas directly behind the mixing enhancer (Case 1 vs. Case 7), which prompts the formation of UFPs. Furthermore, RT can affect the level of dilution rate

significantly. For the lab tunnel, the maximum dilution rate increases 92.4% under the half RT and decrease 56.1% with the double RT. A similar trend can also be found for the field tunnel. It is also shown in Table 6.5 that the variation in RH (Group II) doesn't affect the dilution rate, suggesting that the dilution rate of exhaust is mainly related to the gas dynamics (Group I).

A previous study finds that the possibility of nucleation could become higher with a shorter dilution time duration, which demonstrates that extremely rapid dilution is crucial for obtaining super-saturation where nucleation is possible (Zhang and Wexler, 2004). This effectively interprets our experimental and simulation results, and illustrates that the dilution rate of exhaust can affect the local saturation ratio and alter the formation of UFPs. A similar trend can also be found in other types of nucleation, e.g., Moody and Collins (2003) show that increasing the rate of mixing also increases the rate of formation of TiO_2 particles. Since the dilution process is conducted under a highly turbulent environment, the dilution rate of exhaust is positively related to the level of turbulence, as discussed below.

Turbulence intensity (I) represents the level of turbulence and is defined by:

$$I = \frac{u}{U} \tag{6.8}$$

where U is the mean velocity magnitude, and u is the root-mean-square of the turbulent velocity fluctuations and can be computed from:

$$u = \left(\frac{2k}{3}\right)^{\frac{1}{2}} \tag{6.9}$$

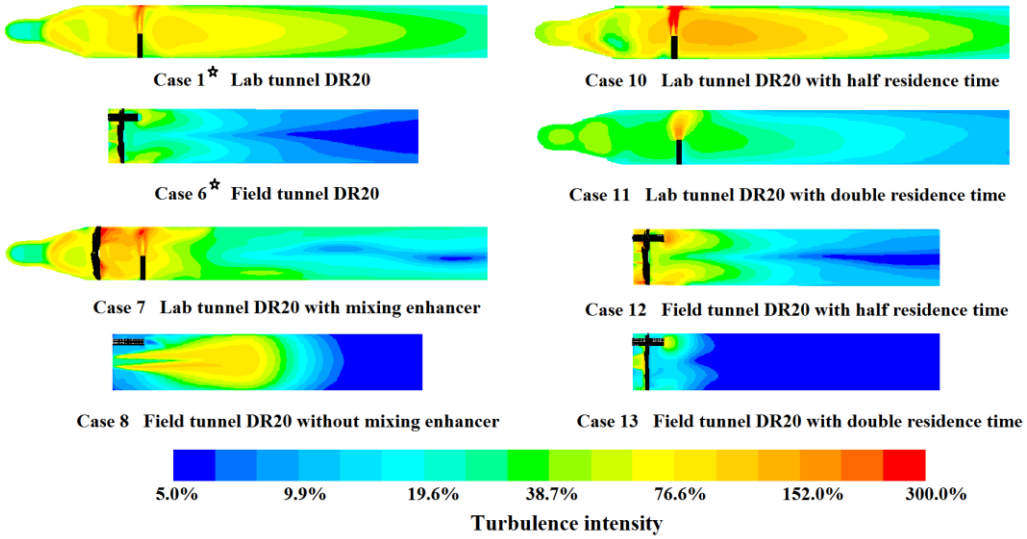

Figure 6.13. Time-averaged turbulence intensity (I) inside dilution tunnels

The dilution process is conducted under a highly turbulent environment, therefore the dilution rate of exhaust is strongly related to the level of turbulence. The turbulence intensity, I, represents the level of turbulence inside the dilution tunnels. As illustrated in Figure 6.13, T-mixing tends to generate more turbulence than coaxial mixing due to the direct intersection between the exhaust and dilution air (Case 1 vs. Case 6). Turbulence intensity also increases in the rear of the mixing enhancer when it is installed in the lab tunnel (Case 1 vs. Case 7). For the field tunnel without the mixing enhancer (Case 8), the level of turbulence in the shear layer between the exhaust and dilution air is also large, however, due to the parallel mixing, few exhaust can be penetrated into the dilution air. Therefore, nucleation is suppressed. Furthermore, RT affects the level of turbulence due to the variation in the flow rate. Turbulence intensity increases under a shorter RT for both lab and field tunnels due to a stronger interaction between the exhaust and dilution air (Case 10 vs. Case 11; Case

12 vs. Case 13). In general, strong turbulence inside the dilution tunnels causes rapid mixing and increases dilution rate of exhaust.

6.5.5 Uncertainty and limitation

There are still uncertainties in some input parameters that were not measured directly, e.g., the sulfuric acid concentration in the exhaust, which is a critical parameter for nucleation. The level of sulfuric acid is dependent on what fraction of the SO_2 formed in the engine is oxidized to SO_3, i.e., cr, and is difficult to measure. In the simulation of aerosol dynamics, uncertainty rises during the selection of cr, e.g., cr as 4-8% is used in the study of Vouitsis et al. (2005), while cr can be much larger if aftertreatment devices are installed (e.g., diesel oxidation catalyst (DOC), diesel particulate filter (DPF)). There is also a potential contribution from the sulfur in the lubricant oil, especially when ultra-low sulfur fuels are used (Vouitsis et al., 2005; Herner et al., 2011). Sensitivity studies of the selection of cr are conducted and discussed in the Supporting Information.

Figure 6.14 shows the dependence of PSDs on cr. For the lab tunnel, compared with the Base Case (cr=5%), the case with cr equals to 8% results in the UFP concentration about 92.2% higher, while the cr of 2% leads to the UFP concentration about 48.7% smaller, which suggests a strong relationship between nucleation and cr. For the field tunnel, cr has little effect on the nucleation mode due to the coaxial mixing.

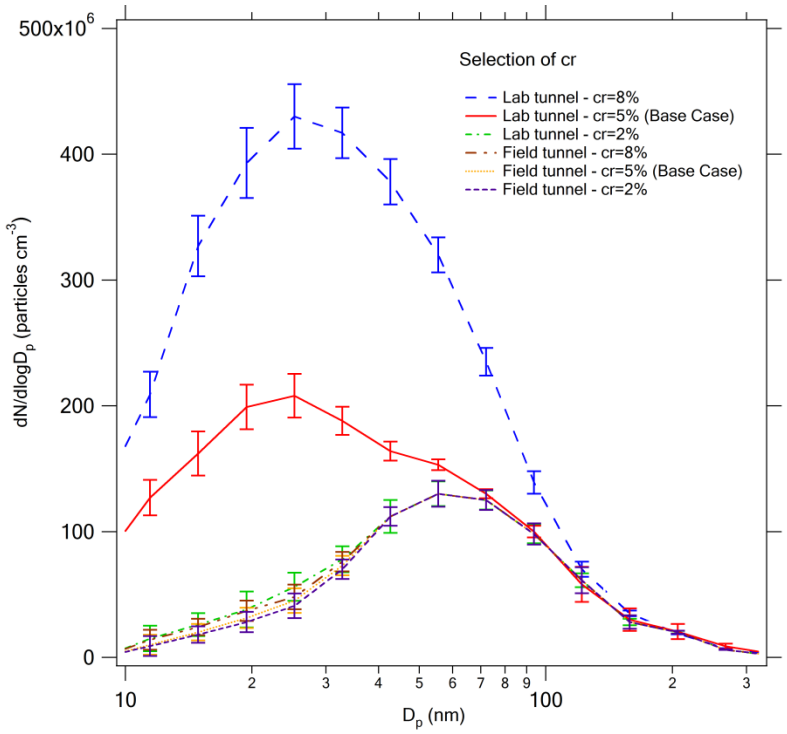

Figure 6.14. The dependence of PSDs on cr for both tunnels

The CTAG model can also be improved, e.g., the binary homogeneous nucleation model of water-sulfuric acid vapor is used to capture the formation of UFPs (Vehkamaki and Lehtinen, 2003). However, there might be other types of nucleation (e.g., nucleation of organics) occurring during the dilution process (Ronkko et al., 2006).

6.6 Conclusion

We have investigated the effects of gas dynamics-related parameters and gas properties-related parameters on the evolution of exhaust particles during the dilution process inside two dilution tunnels. The dilution rate of exhaust was identified as a potentially unifying parameter describing gas dynamics. In general, the formation of

new particles increases with the increasing dilution rate of exhaust. Our study suggests the benefits of simulation tools such as CTAG on improving the design and operation of the dilution tunnels. Simulation-aided designs may become effective in reducing the costs of conducting emission measurements. Many parameters can be varied during dilution tunnel operations to alter the turbulent flow field and affect the aerosol dynamics. With mechanistic understandings of the coupled turbulence and aerosol dynamic processes, we can design and operate the dilution systems to achieve the different goals, e.g., retaining tailpipe-level emissions or capturing the effects of plume processing on exhaust particles. This is important for the ongoing effort to define a standardized dilution sampling methodology for characterizing emissions from stationary combustion sources (Lipsky and Robinson, 2005).

CHAPTER 7

CONTRIBUTIONS AND FUTURE DIRECTIONS

This dissertation presents a four-year development, evaluation and application of the comprehensive CTAG model in the field of air quality. CTAG has demonstrated the capability of resolving the plume dynamics behind individual vehicles and in fabricated dilution systems, which is important for characterizing the emissions from various combustion sources. CTAG can also capture the dynamics of roadway plumes in the roadside micro-environment, which is useful for evaluating the spatial and temporal impacts of traffic-related emissions on near-road air quality. CTAG has also proven its capability in serving as a regulated model that can mitigate near-road air pollution through roadway and surrounding infrastructure designs and define a standardized dilution sampling methodology for characterizing emissions from multiple combustion sources.

7.1 Contributions

1) This dissertation illustrates the major roadway-related turbulence characteristics and incorporates them into near-road air quality for the first time in this research field. It demonstrates that the significant improvement in predicting the spatial gradients of air pollutants near roadways can be achieved by detailed treatment of turbulence characteristics in dispersion modeling. It also indicates that roadway designs affect

near-road air quality and that future roadway designs could serve as an effective strategy to mitigating near-road air pollution.

2) This dissertation reveals that the initial NO_2/NOx ratios have to be carefully selected based on traffic conditions in order to assess NO_2 concentrations near roadways. It is the first to argue that the commonly assumed NO_2/NOx ratio by volume of 5% may not be suitable for most roadways, especially those with a high fraction of heavy-duty truck traffic. It also finds that high O_3 concentrations and high traffic volumes are of particular concern for near-road NO_2 exposure. Under such conditions, peak NO_2 concentration will likely occur near roadways (rather than on roadways), and elevated NO_2 concentration will persistent over a long distance downwind. These findings are crucial for USEPA to revising the health-based National Ambient Air Quality Standards (NAAQS) for NO_2 establishing new monitoring requirements to include monitors at locations where maximum NO_2 concentrations are expected to occur, such as within 50 m of major roadways.

3) This dissertation illustrates that the dynamics of exhaust plumes are highly sensitive to vehicle-induced turbulence, sulfuric acid induced nucleation, and condensation of organic compounds. Moreover, constraining the uncertainties in exhaust sulfuric acid concentrations and the volatility of emitted organic compounds by measurements will help improve the capability of predicting particle size distributions in diluting exhaust plumes.

4) This dissertation is the first to simulate the near-road micro-environmental air quality with coupled turbulence and aerosol dynamics. It introduces a novel multi-scale structure to generate the processed on-road particle emissions. This is an

important process since it captures the formation of nucleation mode particles during the dilution process of the engine exhaust, which is strongly affected by traffic-related activity and meteorology conditions. Additionally, as a proof-of-concept case study, CTAG reveals relative impacts of the CFPP shutdown and the ULSD adoption on the air quality in the intersection micro-environment, illustrating that CTAG can be used to improve the regulatory model in assessing the air quality in multi-scale environments.

5) This dissertation is the first to conduct the simulation of the aerosol dynamics coupled with turbulence inside different dilution systems for diesel engines. It investigates the effects of gas dynamics-related parameters and gas properties-related parameters on the evolution of exhaust particles during the dilution process inside the dilution tunnels. It identifies the dilution rate of exhaust as a potentially unifying parameter describing gas dynamics. The CTAG model has the potential to develop strategies to reduce the uncertainties associated with dilution samplings and define a standardized dilution sampling methodology for characterizing emissions from multiple combustion sources.

7.2 Experience in the development of the CTAG model

I have gained some experience in developing the CTAG model since I came to Cornell University in fall 2008:

The transport part of the CTAG model is based on the commercial CFD software, ANSYS FLUENT, which has been widely used in both academia and industry. ANSYS FLUENT provides various types of turbulence models, e.g., $k-\varepsilon$ model,

Reynolds stress model or Large-eddy simulation model. Meanwhile, it is a good option to develop the transport part of the CTAG model by myself, e.g., coding in Fortran or Matlab. However, the potential problem for me is finding an effective way to generate the computational domain for those complicated geometries (e.g., terrains, buildings) in near-road air quality study.

For the transformation part of the CTAG model, as the key part of simulating the evolution of aerosol particles, the aerosol dynamics (i.e., nucleation, condensation and evaporation, coagulation and deposition) is not incorporated in ANSYS FLUENT. Therefore, it is necessary for me to code the aerosol dynamics module in C-language and incorporated into ANSYS FLUENT through its User-Defined Function (UDF). Within the code, macros are important symbols to communicate with ANSYS FLUENT, since certain parameters (e.g., the temperature, the level of pollutants in each cell within the computational domain) are needed in the calculation for the aerosol dynamics.

7.3 Future directions

This dissertation suggests several future directions to further investigate the emission and dispersion of pollutants from combustion sources by utilizing the CTAG model.

First, based on the current study of the near-road atmospheric dilution and the dilution of vehicle exhaust inside the fabricated dilution system, it is necessary to compare the differences in the transformation of pollutants in the fabricated dilution tunnel, from free jet and in the on-road condition (i.e., in the wake of vehicles), as

illustrated in Figure 7.1, which is important for the ongoing effort to define a standardized dilution sampling methodology.

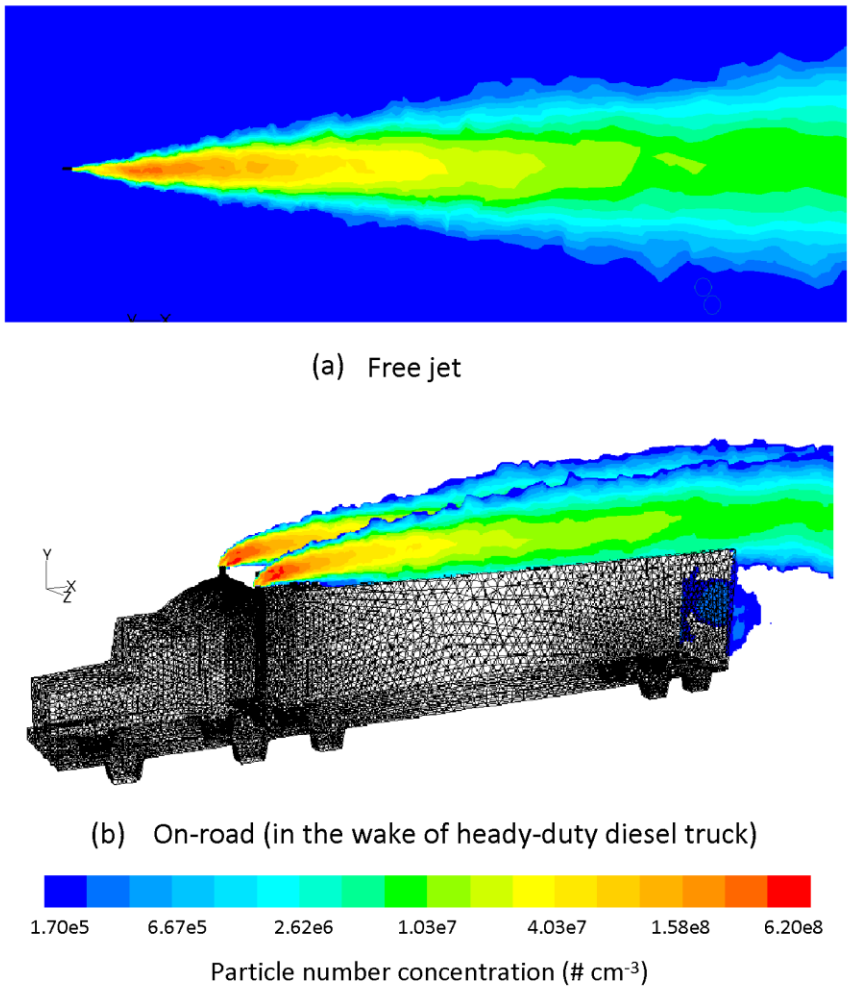

Figure 7.1. The evolution of UFPs in the exhaust plume (a) from a free jet, (b) in the wake of a heavy-duty diesel truck

Second, we will continue our investigation in the turbulent reacting flows inside other types of dilution tunnels that have been widely-used, e.g., the ejector diluter as shown in Figure 7.2 and the rotating disk diluter in Figure 7.3.

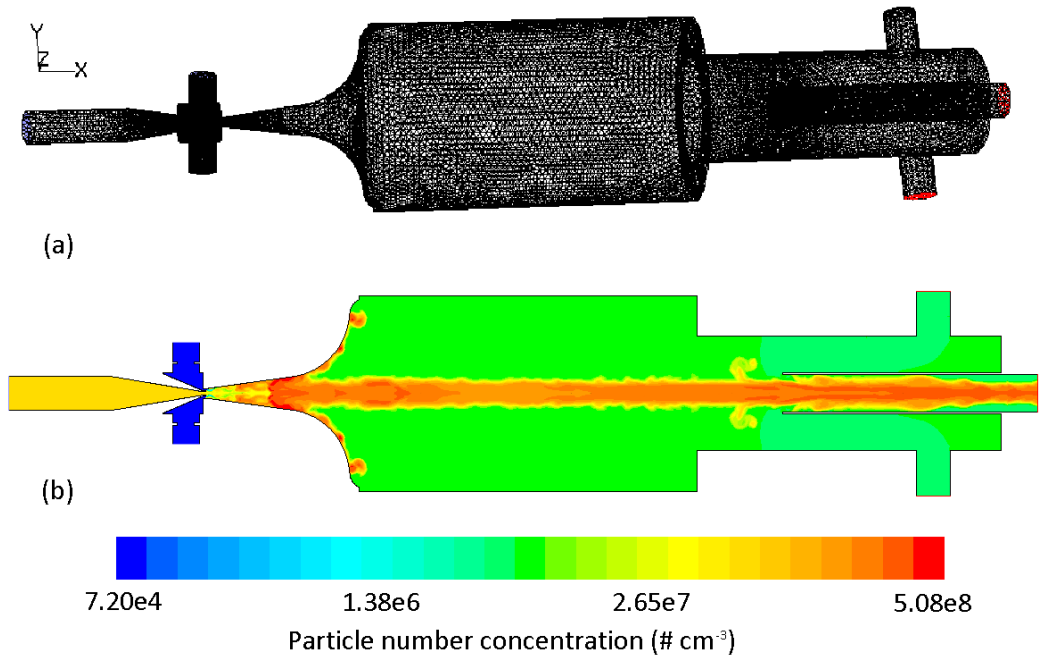

Figure 7.2. Contours of a) the three-dimensional computational domain of the ejector diluter, b) the formation of UPFs inside the ejector diluter

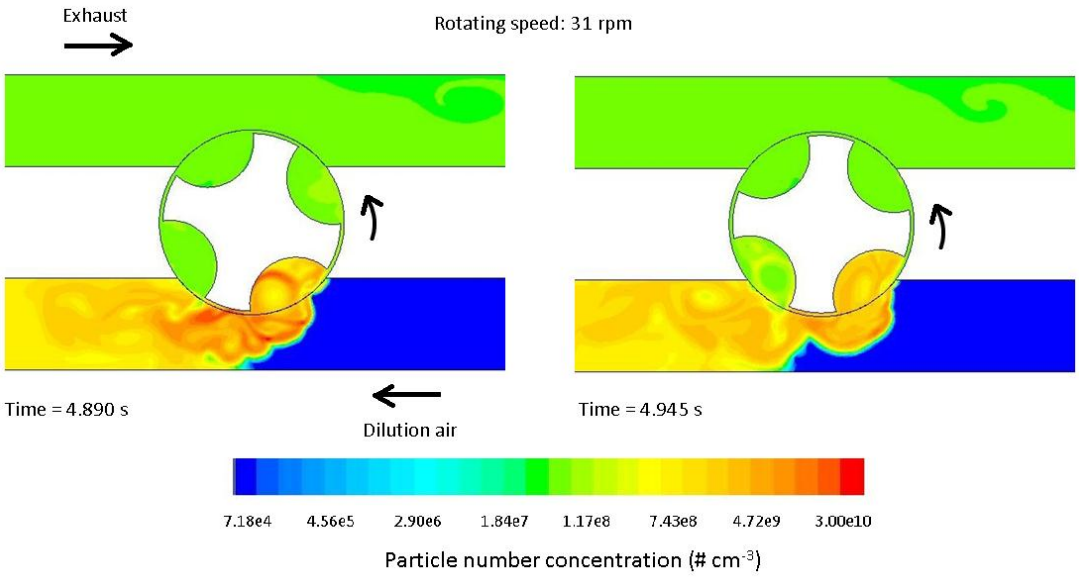

Figure 7.3. Contours of the particle number concentrations at different time within a rotating disk diluter

Meanwhile, the capabilities and applications of the CTAG model are also being expanded by other researchers from the Energy and Environment Research Laboratory (EERL) in Cornell University. For example, the study on the thermoradiative effect of vegetation canopy on the microclimate of urban areas is conducted. The effect of roadside solid barriers or solid barriers with green infrastructures (e.g., green roof) on the near-road air quality is also being studied.

Finally, besides these near-road air quality applications, the CTAG model can also be utilized in analyzing the environmental impacts of other types of emission sources under various circumstances:

- **The cruising aircraft in the stratosphere, idling aircraft near the airport terminal or the aircraft taxing aircraft on the runway**

Aircraft engines emit carbon dioxide, carbon monoxide, oxides of nitrogen, oxides of sulfur, hydrocarbons and aerosol particles. These emissions alter the chemical composition of the atmosphere in a variety of ways, both directly and indirectly. For example, during flight, emissions can cause stratospheric ozone reduction, which leads to increased surface UV radiation. On the ground, air quality can also be decreased by emissions from aircraft and also the associated ground transportation (RCEP, 2004). It is a concern that the techniques for assessment of the impact of aircraft emissions on both local and regional air quality are poorly developed and that the available modeling tools are in general inadequate (Rogers et al., 2002).

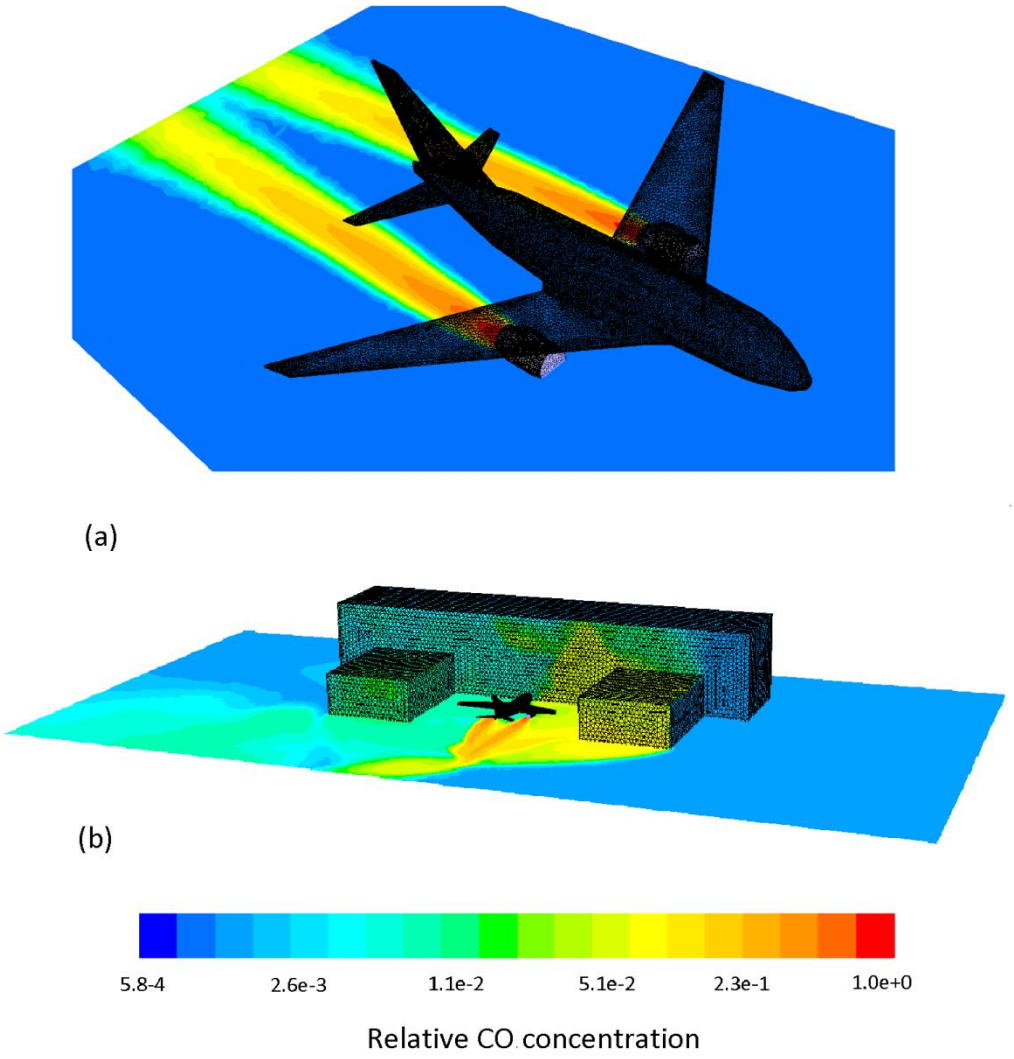

Figure 7.4. (a) The exhaust plume in the wake of a cruising aircraft in the stratosphere, (b) dispersion of pollutants emitted from a idling aircraft near an airport terminal

- **The cargo ship sailing on the sea or berthed cargo ships in the harbor**

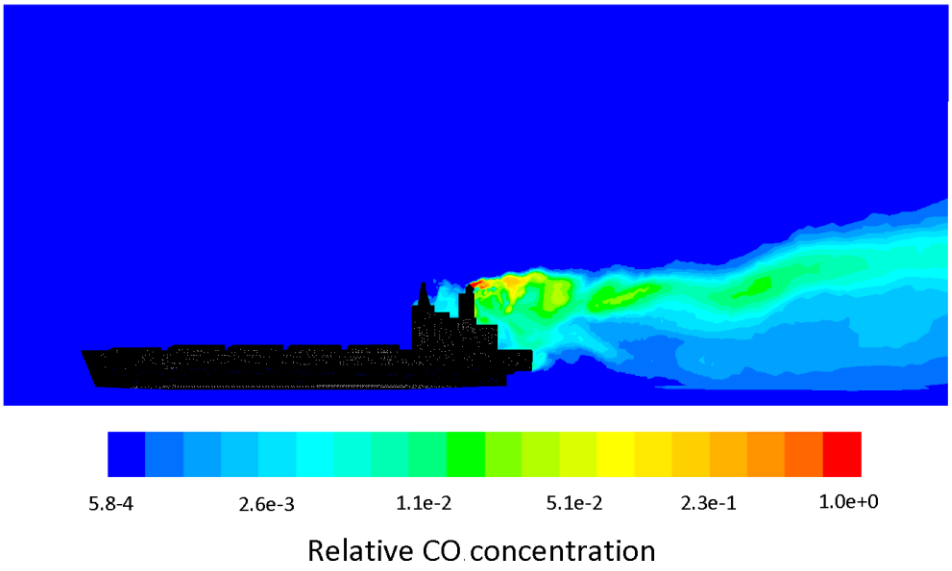

Figure 7.5. The exhaust plume of a cargo ship sailing on the sea

Air emissions from ships account for a non-negligible portion of the emissions inventories and contribute to air quality, human health, and climate change problems at local, regional, and international levels (Eyring et al., 2005; Wang and Corbett, 2007). For example, it is estimated that world cargo ships account for 6-12% of the 55.2-68 million tons of sulfur emissions emanating from global, anthropogenic sources (Stern, 2005).

- **The moving locomotive or idling locomotives in the station.**

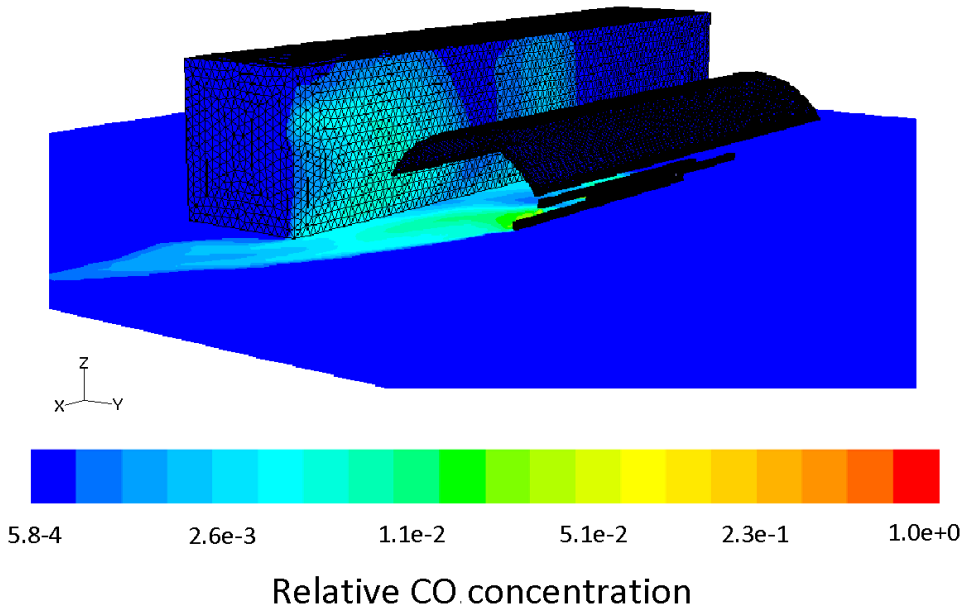

Figure 7.6. Dispersion of pollutants emitted from locomotives in a busy train station

Railway transportation is one of the non-road emission sources and the exhaust can negatively affect communities and ecosystems (Elbir and Dincer, 2007). Besides the primary railway transportation-delivered air pollutants, such as particulate matter (PM), nitrogen oxides (NOx), locomotive diesel exhaust contains approximately 450 organic compounds, of which about 40 are listed as toxic air contaminants with negative effects on human health and the environment (Bailey and Solomon, 2004).

- **The coal-fired or gas-fired power plant**

Coal-fired power plants are the largest human-caused source of sulfur dioxide, a pollutant gas that contributes to the production of acid rain and causes significant health problems, particularly through its role in forming particulates (Miller, 2005).

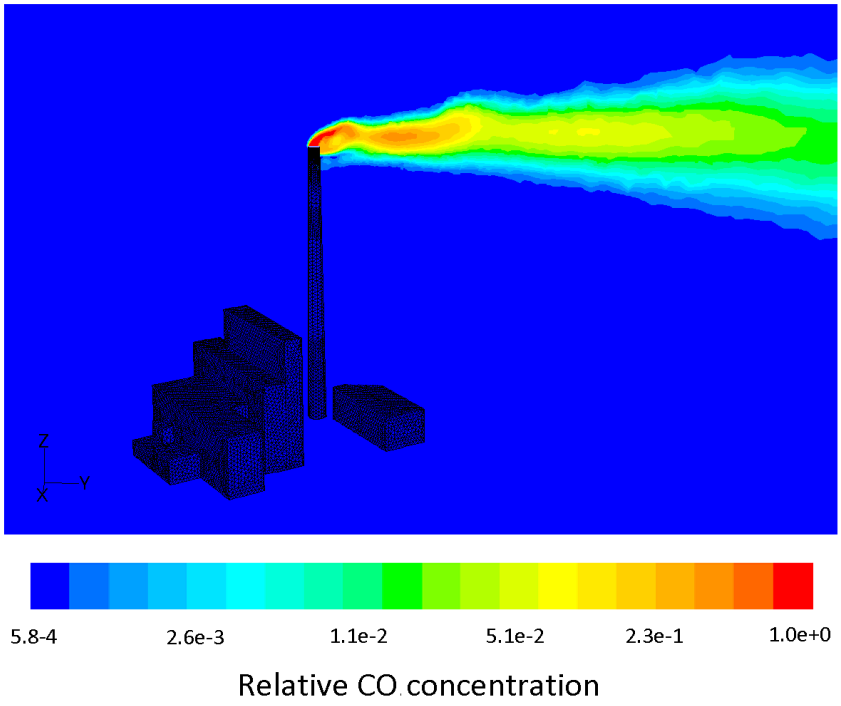

Figure 7.7. The exhaust plume from a coal-fired power plant

In summary, the CTAG model can be an effective tool in these studies, which is important for us to have a better understanding of the emission and dispersion of multiple pollutants from major combustion sources, which can benefit the health of people who work or live near theses sources.

REFERENCES

Abdul-Khalek, I., Kittelson, D., Brear, F. 1999. The influence of dilution conditions on diesel exhaust particle size distribution measurements. SAE Technical Paper 1999-01-1142.

Albriet, B., Sartelet, K. N., Lacour, S., Carissimo, B., Seigneur, C. 2010. Modelling aerosol number distributions from a vehicle exhaust with an aerosol CFD model. Atmospheric Environment 44(8): 1126-1137.

Alvarez, R., Weilenmann, M., Favez, J Y. 2008. Evidence of increased mass fraction of NO_2 within real-world NOx emissions of modern light vehicles - derived from a reliable online measuring method. Atmospheric Environment 42(19): 4699-4707.

ANSYS FLUENT 12.0. 2009. ANSYS FLUENT 12.0 - User's Guide. ANSYS.Inc.

Arnold, F., Pirjola, L., Aufmhoff, H., Schuck, T., Lahde, T., Hameri, K. 2006. First gaseous sulfuric acid measurements in automobile exhaust: Implications for volatile nanoparticle formation. Atmospheric Environment 40(37): 7097-7105.

Baik, J.-J., Kang, Y.-S., Kim J. -J. 2007. Modeling reactive pollutant dispersion in an urban street canyon. Atmospheric Environment 41(5): 934-949.

Bailey, D., Solomon, G. 2004. Pollution prevention at ports: clearing the air. Environment Impact Assessment Review, 24:749–774

Baker, J., Thompson, H. L., Cai, X. 2004. A study of the dispersion and transport of reactive pollutants in and above street canyons--a large eddy simulation. Atmospheric Environment. 38(39): 6883-6892.

Baldauf, R., Thoma, E., Khlystov, A., Isakov, V., Bowker, G., Long, T., Snow, R. 2008. Impacts of noise barriers on near-road air quality. Atmospheric Environment. 42 (32), 7502-7507.

Ban-Weiss, G. A., McLaughlin, J. P., Harley, R. A., Lunden, M. M., Kirchstetter, T. W., Kean, A. J., Strawa, A. W., Stevenson, E. D., Kendall, G. R. 2008. Long-term changes in emissions of nitrogen oxides and particulate matter from on-road gasoline and diesel vehicles. Atmospheric Environment. 42 (2), 220-232.

Baumer, D., Vogel, B., Fiedler, F. 2005. A new parameterisation of motorway-induced turbulence and its application in a numerical model. Atmospheric Environment. 39 (31), 5750-5759.

Benson, P. E. 1992. A review of the development and application of the CALINE3 and CALINE4 models. Atmospheric Environment Part B-Urban Atmosphere. 26 (3), 379-390.

Berkowicz, R. 2000. OSPM - A parameterised street pollution model. Environmental Monitoring and Assessment. 65 (1-2): 323-331.

Blocken, B., Carmeliet, J., Stathopoulos, T. 2007. CFD evaluation of wind speed conditions in passages between parallel buildings - effect of wall-function roughness modifications for the atmospheric boundary layer flow. Journal of Wind Engineering and Industrial Aerodynamics. 95, (9-11), 941-962.

Boylan, J. W., Russell, A. G. 2006. PM and light extinction model performance metrics, goals, and criteria for three-dimensional air quality models. Atmospheric Environment. 40(26): 4946-4959.

Brockmann, J. E., Liu, B. Y. H., McMurry, P. H. 1984. A sample extraction diluter for ultrafine aerosol sampling. Aerosol Science & Technology. 3 (4), 441-451.

Brugge, D., Durant, J. L., Rioux, C. 2007. Near-highway pollutants in motor vehicle exhaust: A review of epidemiologic evidence of cardiac and pulmonary health risks. Environmental Health. 6:23.0.

Builtjes, P. J. H., Talmon, A. M. 1987. Macroscale and microscale mixing in chemical reactive plumes. Boundary-Layer Meteorology 41(1-4): 417-426.

Burtscher, H. 2005. Physical characterization of particulate emissions from diesel engines: a review. Journal of Aerosol Science. 36 (7), 896-932.

Carpenter, L. J., Clemitshaw, K. C., Burgess, R. A., Penkett, S. A., Cape, J. N., McFadyen, G. C. 1998. Investigation and evaluation of the NOx/O_3 photochemical steady state. Atmospheric Environment. 32(19): 3353-3365.

Carslaw, D. C. 2005. Evidence of an increasing NO_2/NO_X emissions ratio from road traffic emissions. Atmospheric Environment. 39(26): 4793-4802.

Carslaw, D. C., Beevers, S. D. 2005. Development of an urban inventory for road transport emissions of NO_2 and comparison with estimates derived from ambient measurements. Atmospheric Environment. 39(11): 2049-2059.

Carter, W. P. L. 2000. Documentation of the SAPRC-99 chemical mechanism for VOC reactivity assessment, Report to the California Air Resources Board.

Casati, R., Scheer, V., Vogt, R., Benter, T. 2007. Measurement of nucleation and soot mode particle emission from a diesel passenger car in real world and laboratory in situ dilution. Atmospheric Environment. 41 (10), 2125-2135.

Chan, S. H., Sun, J. H., Low, S. C. 1998. A compact particulate dilution tunnel for the characterization of diesel exhaust. Proceedings of the Institution of Mechanical Engineerings, Part D: Journal of Automobile Engineering. 212- 299.

Chang, J. C., Hanna, S. R. 2004. Air quality model performance evaluation. Meteorology and Atmospheric Physics. 87, 167-196.

Chemical abstracts. American Chemical Society.

Chock, D. P. 1980. General-Motors sulfate dispersion experiment - An analysis of the wind-field near a road. Boundary-Layer Meteorology. 18 (4), 431-451.

Cimorelli, A. J., Perry, S. G., Venkatram, A., Weil, J. C., Paine, R., Wilson, R. B., Lee, R. F., Peters, W. D., Brode, R. W. 2005. AERMOD: A dispersion model for industrial source applications. Part I: General model formulation and boundary layer characterization. Journal of Applied Meteorology. 44 (5), 682-693.

Clements, A. L., Jia, Y., Denbleyker, A., McDonald-Buller, E., Fraser, M. P., Allen, D. T., Collins, D. R., Michel, E., Pudota, J., Sullivan, D., Zhu, Y. 2009. Air pollutant concentrations near three Texas roadways, part II: Chemical characterization and transformation of pollutants. Atmospheric Environment. 43(30): 4523-4534.

Coe, D. L., Eisinger, D. S., Prouty, J. D., Kear, T. 1998. User's Guide for CL4: A user friendly interface for the CALINE4 model for transportation project impact assessments. Caltrans-U.C. Davis Air Quality Project, Sacamento.

Cook, R., Isakov, V., Touma, J. S., Benjey, W., Thurman, J., Kinnee, E., Ensley, D. 2008. Resolving local-scale emissions for modeling air quality near roadways. Journal of the Air & Waste Management Association. 58 (3), 451-461.

Cook, R., Touma, J. S., Fernandez, A., Brzezinski, D., Bailey, C., Scarbro, C., Thurman, J., Strum, M., Ensley, D., Baldauf, R. 2007. Impact of underestimating the effects of cold temperature on motor vehicle start emissions of air toxics in the United States. Journal of the Air & Waste Management Association. 57 (12), 1469-1479.

DenBleyker, A., Allen, D., McDonald-Buller, E. 2008. Assessment of CO and NOx Emission Estimates from MOBILE6 with Ambient Concentrations from Texas Roadways-Final Report. The Texas Joint Center for Transportation and Air Quality Houston Advanced Research Center (20-23016-UT0707).

Dincer, F., Elbir, T. 2007. Estimating national exhaust emissions from railway vehicles in Turkey. Science of the Total Environment. 374: 127-134.

Donahue, N. M., Robinson, A. L., Stanier, C. O., Pandis, S. N. 2006. Coupled partitioning, dilution, and chemical aging of semivolatile organics. Environmental Science & Technology 40(8): 2635-2643.

Eyring, V., Kohler, H. W., Van Aardenne, J., Lauer, A. 2005. Emissions from international shipping: 1 the last 50 years. Journal of Geophysical Research – Atmospheres. 110, D17305.

Fox, R. O. 2003. Computational models for turbulent reacting flows. Cambridge university press: Cambridge, U. K.

Fraigneau, Y. C., Gonzalez, M., Coppalle, A. 1995. Dispersion and chemical-reaction of a pollutant near a motorway. Science of The Total Environment. 169 (1-3), 83-91.

Fraigneau, Y., Gonzalez, M., Coppalle, A. 1996. The influence of turbulence upon the chemical reaction of nitric oxide released from a ground source into ambient ozone. Atmospheric Environment 30(9): 1467-1480.

Frank, B. P., Tang, S., Lanni, T., Grygas, J., Rideout, G., Meyer, N., Beregszaszy, C. 2007. The effect of fuel type and aftertreatment method on ultrafine particle emissions from a heavy-duty diesel engine. Aerosol Science & Technology. 41:1029-1039.

Fruin, S., Westerdahl, D., Sax, T., Sioutas, C., Fine, P. M. 2008. Measurements and predictors of on-road ultrafine particle concentrations and associated pollutants in Los Angeles. Atmospheric Environment. 42(2):207-219.

Galmarini, S., Vila-Guerau de Arellano, J. Duynkerke, P. G. 1995. The effect of micro-scale turbulence on the reaction rate in a chemically reactive plume. Atmospheric Environment 29(1): 87-95.

Garbrecht, T., Lupkes, C., Augstein, E., Wamser, C. 1999. Influence of a sea ice ridge on low-level airflow. Journal of Geophysical Research-Atmospheres. 104 (D20), 24499-24507.

Georgopoulos, P. G., Seinfeld, J. H. 1986. Mathematical modeling of turbulent reacting plumes-I. General theory and model formulation. Atmospheric Environment 20(9): 1791-1807.

Gery, M. W., Whitten, G. Z., Killus, J. P., Dodge, M. C. 1989. A photochemical kinetics mechanism for urban and regional scale computer modeling. Journal of Geophysical Research-Atmospheres, 94, 12925–12956.

Gidhagen, L., Johansson, C., Omstedt, G., Langner, J., Olivares, G. 2004. Model simulations of NOx and ultrafine particles close to a Swedish highway. Environmental Science & Technology. 38 (24), 6730-6740.

Gonzalez, M. 1997. Analysis of the effect of microscale turbulence on atmospheric chemical reactions by means of the pdf approach. Atmospheric Environment 31(4): 575-586.

Green, S. R. 1992. Modelling turbulent air flow in a stand of widely-spaced trees. The Phoenics Journal of Computational Fluid Dynamics and its Application. 5. 294-312.

Grieshop, A., Miracolo, M. A., Donahue, N. M., Robinson, A. L. 2009. Constraining the volatility distribution and gas-particle partitioning of combustion aerosols using isothermal dilution and thermodenuder measurements. Environmental Science & Technology. 43 (13), 4750-4656.

Gromke, C., Buccolieri, R., Di Sabatino, S., Ruck, B. 2008. Dispersion study in a street canyon with tree planting by means of wind tunnel and numerical investigations - Evaluation of CFD data with experimental data. Atmospheric Environment. 42 (37), 8640-8650.

Guleren, K. M., Turan, A. 2007. Validation of large-eddy simulation of strongly curved stationary and rotating U-duct flows. International Journal of Heat and Fluid Flow. 28, 909-921.

Hagler, G. S. W., Baldauf, R. W., Thoma, E. D., Long, T. R., Snow, R. F., Kinsey, J. S., Oudejans, L., Gullett, B. K. 2009. Ultrafine particles near a major roadway in Raleigh, North Carolina: Downwind attenuation and correlation with traffic-related pollutants. Atmospheric Environment. 43 (6), 1229-1234.

Hauf, T., Neumannhauf, G. 1982. The turbulent wind flow over an embankment. Boundary-Layer Meteorology. 24 (3), 357-369.

Health Effects Institute. 2010. Traffic-Related Air Pollution: A Critical Review of the Literature on Emissions, Exposure, and Health Effects. HEI Special Report 17.

HEI. 2010. Traffic-Related Air Pollution: A critical review of the literature on emissions, exposure, and health effects. Boston, MA, Health Effects Institute.

Held, T., Chang, D. P. Y., Niemeier, D. A. 2003. UCD 2001: an improved model to simulate pollutant dispersion from roadways. Atmospheric Environment 37(38): 5325-5336.

Herner, J. D., Hu, S., Robertson, W. H., Huai, T., Collins, J. F., Dwyer, H., Ayala, A. 2009. Effect of advanced aftertreatment for PM and NOx control on heavy-duty diesel truck emissions. Environmental Science & Technology 43(15): 5928-5933.

Herner, J. D., Hu, S., Robertson, W. H., Huai, T., Chang, M. C. O., Rieger, P., Ayala, A. 2011. Effect of advanced aftertreatment for PM and NOx reduction on heavy-duty diesel engine ultrafine particle emissions. Environmental Science & Technology 45:2413-2419.

Hildemann, L. M., Cass, G. R., Markowski, G. R. 1989. A dilution stack sampler for collection of organic aerosol emissions: design, characterization and field tests. Aerosol Science & Technology. 10 (1), 193-204.

Hoek, G., Brunekreef, B., Goldbohm, S., Fischer, P., van den Brandt, P. A. 2002. Association between mortality and indicators of traffic-related air pollution in the Netherlands: a cohort study. Lancet 360(9341):1203-1209.

Horvath, S. M. 1980. Nitrogen dioxide, pulmonary function, and respiratory disease. Bulletin of the New York Academy of Medicine. 56(9): 835-846.

Hosker, Jr., R. P., Rao, K. S., Gunter, R. L., Nappo, C. J., Meyers, T. P., Birdwell, K. R., White, J. R. 2003. Issues affecting dispersion near highways: Light winds, intra-urban dispersion, vehicle wakes, and the roadway-2 dispersion model.

Isakov, V., Touma, J. S., Burke, J., Lobdell, D. T., Palma, T., Rosenbaum, A., Ozkaynak, H. 2009. Combining regional- and local-scale air quality models with exposure models for use in environmental health studies. Journal of the Air & Waste Management Association. 59:461-472.

Jacobson, M. Z. 1997. Development and application of a new air pollution modeling system - ii. aerosol module structure and design. Atmospheric Environment. 31, 131-144.

Johnson, J. P., Kittelson, D. B., Watts, W. F. 2009. The effect of federal fuel sulfur regulations on in-use fleets: On-road heavy-duty source apportionment. Environmental Science & Technology. 43(14):5358-5364.

Kalthoff, N., Baumer, D., Corsmeier, U., Kohler, M., Vogel, B. 2005. Vehicle-induced turbulence near a motorway. Atmospheric Environment. 39 (31), 5737-5749.

Karamchandani, P., Koo, A., Seigneur, C. 1998. Reduced gas phase kinetic mechanisms for atmospheric plume chemistry. Environmental Science & Technology 32(11): 1709-1720.

Katolicky, J., Jicha, M. 2005. Eulerian-Lagrangian model for traffic dynamics and its impact on operational ventilation of road tunnels. Journal of Wind Engineering and Industrial Aerodynamics. 93 (1), 61-77.

Kenty, K. L., Poor, N. D., Kronmiller, K. G., McClenny, W., King, C., Atkeson, T., Campbell, S. W. 2007. Application of CALINE4 to roadside NO/NO_2 transformations. Atmospheric Environment. 41(20): 4270-4280.

Keogh, D. U., Ferreira, L., Morawska, L. 2009. Development of a particle number and particle mass vehicle emissions inventory for an urban fleet. Environmental modeling & Software. 24(11):1323-1331.

Khalek, I. A., Spears, M., Charmley, W. 2003. Particle size distribution from a heavy-duty diesel engine: steady-state and transient emission measurement using two dilution systems and two fuels. SAE Paper 2003-01-0285.

Khare, M., Chaudhry, K. K., Gowda, R. M. M., Ahmad, K. 2005. Effects of the homogeneous traffic on vertical dispersion parameter in the near field of roadways - A wind tunnel study. Environmental Modeling & Assessment. 10 (1), 55-62.

Kim, J.-J., Baik, J.-J. 2001. Urban street-canyon flows with bottom heating. Atmospheric Environment. 35 (20), 3395-3404.

Kim, H. G., Patel, V. C. 2000. Test of turbulence models for wind flow over terrain with separation and recirculation. Boundary-Layer Meteorology. 94 (1), 5-21.

Kittelson, D. B., Arnold, M., Watts, W. F. 1998. Review of diesel particulate matter sampling methods Supplemental Report # 2, Aerosol dynamics, laboratory and on-road studies.

Kittelson, D. B., Watts, W. F., Johnson, J. P. 2006. On-road and laboratory evaluation of combustion aerosols-Part I: Summary of diesel engine results. Journal of Aerosol Science. 37(8): 913-930.

Kittelson, D. B., Watts, W. F., Johnson, J. P., Thorne, C., Higham, C., Payne, M., Goodier, S., Warrens, C., Preston, H., Zink, U., Pickles, D., Goersmann II, C., Twigg II, M. V., Walker, A. P., Boddy, R. 2008. Effect of fuel and lube oil sulfur on the performance of a diesel exhaust gas continuously regenerating trap. Environmental Science & Technology 42: 9276-9282.

Kittelson, D. B., Kadue, P. A., Scherrer, H. C., Loverien, R. E. 1988. Characterization of diesel particles in the atmosphere. CRC, AP-2 Project Group.

Kozaka, E. O., Ozkan, G., Ozdemir, I. B. 2004. Turbulent structure of three-dimensional flow behind a model car: 1. Exposed to uniform approach flow. Journal of Turbulence. 5, 22.

Kumar, P., Ketzel, M., Vardoulakis, S., Pirjola, L., Britter, R. 2011. Dynamics and dispersion modelling of nanoparticles from road traffic in the urban atmospheric environment - A review. Journal of Aerosol Science. 42(9):580-603.

Kunzli, N., McConnell, R., Bates, D., Bastain, T., Hricko, A., Lurmann, F., Avol, E., Gilliland, F., Peters. J. 2003. Breathless in Los Angeles: the exhausting search for clean air. American Journal of Public Health. 93(9):1494-1499.

Lidman, J. K. 1985. Effect of a noise wall on snow accumulation and air quality. Transportation Research Record. 1033, 79-88.

Lien, F. S., Yee, E., Cheng, Y. 2004. Simulation of mean flow and turbulence over a 2D building array using high-resolution CFD and a distributed drag force approach. Journal of Wind Engineering and Industrial Aerodynamics 92, (2), 117-158.

Lipsky, E. M., Robinson, A. L. 2005. Design and evaluation of a portable dilution sampling system for measuring fine particle emissions from combustion systems. Aerosol Science & Technology. 39 (6), 542-553.

Lipsky, E., Stanier, C. O., Pandis, S. N., Robinson, A. L. 2002. Effects of sampling conditions on the size distribution of fine particulate matter emitted from a pilot-scale pulverized-coal combustor. Energy & Fuels. 16 (2), 302-310.

Liu, C. S., Ahmadi, G. 2005. Computer simulation of pollutant transport and deposition near Peace Bridge. Particulate Science and Technology. 23 (2), 109-127.

Liu, J., Chen, J. M. Black, T. A., Novak, M. D. 1996. E-ε modeling of turbulent air flow downwind of a model forest edge. Boundary-Layer Meteorology. 77(1): 21-44.

Liu, Y. H., He, Z., Chan, T. L. 2011. Three-dimensional simulation of exhaust particle dispersion and concentration fields in the near-wake region of the studied ground vehicle. Aerosol Science and Technology 45(8): 1019-1030.

Lyyranen, J., Jokiniemi, J., Kauppinen, E. I., Backman, U., Vesala, H. 2004. Comparison of different dilution methods for measuring diesel particle emissions. Aerosol Science & Technology. 38, 12-23.

Mao, J., Ren, X., Chen, S., Brune, W. H., Chen, Z., Martinez, M., Harder, H., Lefer, B., Rappengluck, B., Flynn, J., Leuchner, M. 2009. Atmospheric oxidation capacity in the summer of Houston 2006: Comparison with summer measurements in other metropolitan studies. Atmospheric Environment. 44: 4107-4115.

Maricq, M. M., Chase, R. E., Xu, N., Podsiadlik, D. H. 2002. The effects of the catalytic converter and fuel sulfur level on motor vehicle particulate matter emissions: Gasoline vehicles. Environmental Science & Technology. 36:276-282.

Maricq, M. M., Chase, R. E., Podsiadlik, D. H., Vogt, R. 1999. Vehicle exhaust particle size distributions: a comparison of tailpipe and dilution tunnel measurements. SAE Paper 1999-01-1461.

Maricq, M. M., Podsiadlik, D. H., Chase, R. E. 1999. Gasoline vehicle particle size distributions: Comparison of steady state, FTP, and US06 measurements. Environmental Science & Technology. 33(12):2007-2015.

Mathis, U., Ristimaki, J., Mohr, M., Keskinen, J., Ntziachristo, L., Samaras, Z.; Mikkanen, P. 2004. Sampling conditions for the measurement of nucleation mode particles in the exhaust of a diesel vehicle. Aerosol Science & Technology. 38 (1149-1160).

McConnell, R., Berhane, K., Yao, L., Jerrett, M., Lurmann, F., Gilliland, F., Kunzli, N., Gauderman, J., Avol, E., Thomas, D., Peters, J. 2006. Traffic, susceptibility, and childhood asthma. Environmental Health Perspectives. 114 (5), 766-772.

Miller, B. G. 2005. Coal energy systems. Elsevier Academic Press.

Moody, E. G., Collins, L. R. Effect of mixing on the nucleation and growth of titania particles. 2003. Aerosol Science & Technology. 37, 403-424.

NREL. 1999. Diesel emission control – sulfur effects (DECSE) program. Phase I interim data report No. 3: Diesel fuel sulfur effects on particulate matter emissions.

Oran, E. S., Boris, J. P. 2005. Numerical simulation of reactive flow. Cambridge University Press. 2nd Edition.

OSHA. 2000. Chemical sampling information: nitrogen dioxide. Occupational Safety and Health Administration.

Ozdemir, E., Ozdemir, I. B. 2004. Turbulent structure of three-dimensional flow behind a model car: 2. Exposed to crosswind. Journal of Turbulence.

Pandis, S. N., Wexler, A. S., Seinfeld, J. H. 1995. Dynamics of Tropospheric Aerosols. Journal of Physical Chemistry. 99(24): 9646-9659.

Papavergos, P. G., Hedley, A. B. 1984. Particle deposition behavior from turbulent flow. Chemical Engineering Research and Design. 62, 275-295.

Particulate. 2005. Characterization of exhaust particulate emissions from road vehicles.

Peters, A., von Klot, S., Heier, M., Trentinaglia, I., Hormann, A., Wichmann, H. E., Lowel, H. 2004. Exposure to traffic and the onset of myocardial infarction. New England Journal of Medicine. 351 (17), 1721-1730.

Peters, N. 2000. Turbulent combustion. Cambridge University Press.

Pope, S. B. 2008. Turbulent flows. Cambridge University Press.

Pope, S. B. 1985 PDF methods for turbulent reacting flows. Progress in Energy and Combustion Science. 11, 119-192.

Pyykonen, J., Miettinen, M., Sippula, O., Leskinen, A., Raunemaa, T., Jokiniemi, J. 2007. Nucleation in a perforated tube diluter. Journal of Aerosol Science. 38, 172-191.

Rao, K. S., Gunter, R. L., White, J. R., Hosker, R. P. 2002. Turbulence and dispersion modeling near highways. Atmospheric Environment. 36 (27), 4337-4346.

RCEP. Royal commission on environmental pollution - The environmental effects of civil aircraft in flight. 2004.

Riddle, A., Carruthers, D., Sharpe, A., McHugh, C., Stocker, J. 2004. Comparisons between FLUENT and ADMS for atmospheric dispersion modelling. Atmospheric Environment. 38 (7), 1029-1038.

Rogers, H. L., Lee, D. S., Raper, D. W., de Forster, P. M., Wilson, C. W., Newton, P. J. 2002. The impacts of aviation on the atmosphere. QinetiQ report number QINETIO/FST/CT/TR021654.

Ronkko T, Virtanen A, Vaaraslahti K, Keskinen J, Pirjola L, Lappi M. 2006. Effect of dilution conditions and driving parameters on nucleation mode particles in diesel exhaust: Laboratory and on-road study. Atmospheric Environment. 40(16):2893-2901.

Sadanaga, Y., Matsumoto, J., Kajii, Y. 2003. Photochemical reactions in the urban air: Recent understandings of radical chemistry. Journal of Photochemistry and Photobiology C: Photochemistry Reviews 4(1): 85-104.

Sahlodin, A. M., Sotudeh-Gharebagh, R., Zhu, Y. F. 2007. Modeling of dispersion near roadways based on the vehicle-induced turbulence concept. Atmospheric Environment. 41 (1), 92-102.

Samet, J. M. 2007. Traffic, air pollution, and health. Inhalation Toxicology. 19 (12), 1021-1027.

Schauer, J. J., Kleeman, M. J., Cass, G. R., Simoneit, B. R.T. 1999. Measurement of emissions from air pollution sources. 2. C_1 through C_{30} organic compounds from medium duty diesel trucks. Environmental Science & Technology. 33(10): 1578-1587.

Schauer, J. J., Kleeman, M. J., Cass, G. R., Simoneit, B. R.T. 2002. Measurement of emissions from air pollution sources. 5. C_1-C_{32} organic compounds from gasoline-powered motor vehicles. Environmental Science & Technology. 36(6): 1169-1180.

Seinfield, J. H., Pandis, S. N. 2006. Atmospheric chemistry and physics: From air pollution to climate change. JOHN WILEY & SONS, INC.

Shi, J. P., Harrison, R. M. 1999. Investigation of ultrafine particle formation during diesel exhaust dilution. Environmental Science & Technology. 33(21):3730-3736.

Shi, J. P., Harrison, R. M., Evans, D. E., Alam, A., Barnes, C., Carter, G. 2002. A method for measuring particle number emissions from vehicles driving on the road. Environmental Technology. 23(1):1–14.

Singh, N., Joshi, R. R., Chun, H. Y., Pant, G. B., Damle, S. H., Vashishtha, R. D. 2008. Seasonal, annual and inter-annual features of turbulence parameters over the tropical station Pune (18 degrees 32 ' N, 73 degrees 51 ' E) observed with UHF wind profiler. Annales Geophysicae. 26 (12), 3677-3692.

Sini, J. F., Anquetin, S., Mestayer, P. G. 1996. Pollutant dispersion and thermal effects in urban street canyons. Atmospheric Environment. 30 (15), 2659-2677.

Smagorinsky J. 1963. General circulation experiments with the primitive equations. Monthly Weather Review. 91:99–164.

Steffens, J., Wang, Y. J., Zhang, M. 2012. Exploration of effects of a vegetation barrier on particle size distributions in a near-road environment. Atmospheric Environment. Atmospheric Environment. 50: 120-128.

Stern, D. I. 2005. Global sulfur emissions from 1850 to 2000. Chemosphere, 163-175.

Strand, M., Bohgard, M., Swietlicki, E., Gharibi, A., Sanati, M. 2004. Laboratory and field test of a sampling method for characterization of combustion aerosols at high temperatures. Aerosol Science & Technology. 38, 757-765.

Talbot, L., Cheng, R. K., Schefer, R. W., Willis, D. R. 1980. Thermophoresis of particles in a heated boundary layer. Journal of Fluid Mechanisms. 101 (4), 737-758.

Terjung, W. H., Orourke, P. A. 1982. The effects of changing solar angles, cloud regimes, and air temperatures on the temperatures of contrasting surfaces. Boundary-Layer Meteorology. 24 (3), 269-279.

Thompson, R. S., Eskridge, R. E. 1987. Turbulent diffusion behind vehicles: Experimentally determined influence of vortex pair in vehicle wake. Atmospheric Environment. 21 (10), 2091-2097.

Thom, A. S. 1975. Momentum, mass and heat exchange of plant communities. Vegetation and the Atmosphere 1: 1-278. Burlington, Mass: Academic.

Tong, Z., Wang, Y. J., Patel, M., Kinney, P., Chillrud, S. and Zhang, K. M. 2012. Modeling spatial variations of black carbon particles in an urban highway-buildings environment. Environmental Science & Technology. 46 (1): 312-319.

Trebs, I., Bohn, B., Ammann, C., Rummel, U., Blumthaler, M., Konigstedt, R., Meixner, F. X., Fan, S., Andreae, M. O. 2009. Relationship between the NO2 photolysis frequency and the solar global irradiance. Atmospheric Measurement Technology. 2(2): 725-739.

Uhrner, U., von Löwis, S., Vehkamäki, H., Wehner, B., Bräsel, S., Hermann, M., Stratmann, F., Kulmala, M., Wiedensohler, A. 2007. Dilution and aerosol dynamics within a diesel car exhaust plume-CFD simulations of on-road measurement conditions. Atmospheric Environment. 41(35): 7440-7461.

Uhrner, U., von Löwis, S., Zallinger, M., Vehkamäki, H., Wehner, B., Stratmann, F., Wiedensohler, A. 2011. Volatile nanoparticle formation and growth within a diluting diesel car exhaust, Journal of the Air & Waste Management Association. 61(4), 399-408.

USEPA. 1999. EPA's program for cleaner vehicles and cleaner gasoline. Office of Mobile Sources.

USEPA. 2000. Code of Federal Regulations. Regulation of fuels and fuel additives (40 CFR 80).

USEPA. 2010. Primary national ambient air quality standard for nitrogen dioxide; final rule. Federal Register 75(26): 6474-6537.

Venkatram, A., Isakov, V., Yuan, J., Pankratz, D. 2004. Modeling dispersion at distances of meters from urban sources. Atmospheric Environment. 38 (28), 4633-4641.

Vehkamaki, H., Kulmala M., Lehtinen, K. E. J. 2003. Modelling binary homogeneous nucleation of water-sulfuric acid vapours: Parameterisation for high temperature emissions. Environmental Science & Technology. 37(15): 3392-3398.

Vehkamaki, H., Kulmala M., Napari, I., Lehtinen, K. E. J., Timmreck, C., Noppel, M., Laaksonen, A. 2002. An improved parameterization for sulfuric acid-water nucleation rates for tropospheric and stratospheric conditions. Journal of geophysical research. 107(D22): 4622.

Vouitsis, E., Ntziachristos, L., Samaras, Z. 2005. Modelling of diesel exhaust aerosol during laboratory sampling. Atmospheric Environment. 39 (7), 1335-1345.

Walklate, P. J., Weiner, K. L., Parkin, C. S. 1996. Analysis of and experimental measurements made on a moving air-assisted sprayer with two dimensional air jets penetrating uniform crop canopy. Journal of Agricultural Engineering. (63) 365-378.

Wang, C., Corbett, J. J. 2007. The costs and benefits of reducing SO2 emissions from ships in the US West Coastal waters. Transportation Research Part D. 12 577-588.

Wang, H., Pope, S. B. 2011. Large eddy simulation/probability density function modeling of a turbulent $CH_4/H_2/N_2$ jet flame. Proceedings of the Combustion Institute. 33(1): 1319-1330.

Wang, X. Characterizing on-road vehicular emissions and their impacts on near-roadway air pollution. Dissertation. 2011.

Wang, Y., Hopke, P. K., Chalupa, D. C., Utell, M. J. 2011a. Long-term study of urban ultrafine particles and other pollutants. Atmospheric Environment. 45(40):7672-7680.

Wang, Y., Hopke, P. K., Rattigan, O., Chalupa, D. C., Utell, M. J. 2012. Multiple year black carbon measurements and source apportionment using Delta-C in Rochester, NY. Journal of the Air & Waste Management Association. 62(8): 880-887.

Wang, Y. J., Zhang, K. M. 2009. Modeling Near-Road Air Quality Using a Computational Fluid Dynamics Model, CFD-VIT-RIT. Environmental Science & Technology. 43(20): 7778-7783.

Wang, Y. J., DenBleyker, A., McDonald-Buller, E., Allen, D., Zhang, K. M. 2011b. Modeling the chemical evolution of nitrogen oxides near roadways. Atmospheric Environment. 45(1): 43-52.

Wang, Y. J., Zhang, K. M. 2012. Coupled turbulence and aerosol dynamics modeling of vehicle exhaust plumes using the CTAG model. Atmospheric Environment. 59: 284-293.

Wang, Y., Nguyen, M. T., Steffens, J. T., Tong, Z., Wang, Y., Hopke, P. K., Zhang, K. M. Modeling multi-scale aerosol dynamics and micro-environmental air quality near a large highway intersection using the CTAG model. Science of the Total Environment. In revision.

Wang, Y., Yang, B., Lipsky, E. M., Robinson, A. L., Zhang, K. M. Analyses of turbulent flow fields and aerosol dynamics of diesel engine exhaust inside two dilution sampling tunnels using the CTAG model. Environmental Science & Technology. Under review.

Wehner, B., Uhrner, U., Von Löwis, S., Zallinger, M., Wiedensohler, A. 2009. Aerosol number size distributions within the exhaust plume of a diesel and a gasoline passenger car under on-road conditions and determination of emission factors. Atmospheric Environment. 43(6): 1235-1245.

Wegner, B., Huai, Y., Sadiki, A. 2004. Comparative study of turbulent mixing in jet in cross-flow configurations using LES. International Journal of Heat and Fluid Flow. 25, 767-775.

Westerdahl, D., Wang, X., Pan, X. C., Zhang, K. M. 2009. Characterization of on-road vehicle emission factors and microenvironmental air quality in Beijing, China. Atmospheric Environment. 43 (3), 697-705.

White, F. M. 2002. Fluid Mechanics. McGraw-Hill Science Engineering.

Xie, X. M., Huang, Z., Wang, J. S., Xie, Z. 2005. The impact of solar radiation and street layout on pollutant dispersion in street canyon. Building and Environment. 40 (2), 201-212.

Xie, X., Liu, C.-H., Leung, D. Y. C. 2007. Impact of building facades and ground heating on wind flow and pollutant transport in street canyons. Atmospheric Environment. 41 (39), 9030-9049.

Xie, X. M., Liu, C. H., Leung, D. Y. C., Leung, M. K. H. 2006. Characteristics of air exchange in a street canyon with ground heating. Atmospheric Environment. 40 (33), 6396-6409.

Yarwood, G., Rao, S., Yocke, M., Whitten, G. Z. 2005. Updates to the carbon bond chemical mechanism: CB05. Final report to the U.S. EPA, RT-0400675.

Zhang, K. M., Wexler, A. S. 2004. Evolution of particle number distribution near roadways--Part I: analysis of aerosol dynamics and its implications for engine emission measurement. Atmospheric Environment. 38 (38), 6643-6653.

Zhang, K. M., Wexler, A. S., Zhu, Y. F., Hinds, W. C., Sioutas, C. 2004. Evolution of particle number distribution near roadways. Part II: the 'road-to-ambient' process. Atmospheric Environment. 38 (38), 6655-6665.

Zhang, K. M., Wexler, A. S., Niemeier, D. A., Zhu, Y. F., Hinds, W. C., Sioutas, C. 2005. Evolution of particle number distribution near roadways. Part III: Traffic analysis and on-road size resolved particulate emission factors. Atmospheric Environment. 39 (22), 4155-4166.

Zhang, K. M., Wexler, A. S. 2002. Modeling the number distributions of urban and regional aerosols: theoretical foundation. Atmospheric Environment. 36 (11): 1863-1874.

Zhang, K. M., Wexler, A. S. 2006. An asynchronous time-stepping (ATS) integrator for atmospheric applications: Aerosol dynamics. Atmospheric Environment. 40(24): 4574-4588.

Zhu, Y. F., Hinds, W. C., Kim, S., Sioutas, C. 2002a. Concentration and size distribution of ultrafine particles near a major highway. Journal of the Air & Waste Management Association. 52, (9), 1032-1042.

Zhu, Y. F., Hinds, W. C. 2005. Predicting particle number concentrations near a highway based on vertical concentration profile. Atmospheric Environment. 39 (8), 1557-1566.

Zhu, Y. F., Hinds, W. C., Shen, S., Sioutas, C. 2004. Seasonal trends of concentration and size distribution of ultrafine particles near major highways in Los Angeles. Aerosol Science and Technology. 38, 5-13.

Zhu, Y. F., Hinds, W. C., Kim, S., Shen, S., Sioutas, C. 2002b. Study of ultrafine particles near a major highway with heavy-duty diesel traffic. Atmospheric Environment. 36, (27), 4323-4335.

Zhu, Y., Pudota, J., Collins, D., Allen, D., Clements, A., DenBleyker, A., Fraser, M., Jia, Y., McDonald-Buller, E., Michel, E. 2009. Air pollutant concentrations near three Texas roadways, Part I: Ultrafine particles. Atmospheric Environment. 43(30): 4513-4522.